

On modelling and experimentation of planar grinding using abrasive pads with grits of defined geometries and distributions for enabling controlled surface texture

by Yuchen Zhou

Thesis submitted to the University of Nottingham for the Degree of Doctor of Philosophy

January 2018

Abstract

The surface of diamond grinding tool manufactured by current production method exhibits stochastic nature in terms of different grit size, irregular geometry, random crystallinegraphic orientation, non-uniform spacing, and varying protrusion heights. These topography characteristics has been found having various negative effects for the abrasive performance, especially in high-precision applications, causing less controllable surface topography, inefficient chip flow, high working temperature and cutting force.

The thesis covers the design and manufacture of laser generated novel abrasive pad with ordered abrasive grits from CVD polycrystalline diamond films, providing repeatable patterns and shapes for abrasive tool used in load controlled plane grinding process, which is regarded as engineered abrasive pad. Two major design parameters for engineered abrasive pad, including abrasive grit geometry and planar contact area between grits and workpiece surface, were investigated. An inverted test setup was developed to enable the evaluation for the performance of ordered abrasive pad under plane grinding operation. The analysis of material removal and surface topography was made and compared between conventional abrasive pad (randomly shaped grits) and two engineered abrasive pad (saw tooth and square frustum) to evaluate the influence of grit geometry on the grinding performance. Furthermore, a geometrical model was developed to simulate the surface roughness generated by engineered abrasive pad. Inverted tests were conducted allowing the validation of the model. Besides grit geometry, three abrasive pads (one conventional, two engineered) with different planar contact were also studied through inverted grinding test to evaluate the influence of planar contact area on grinding performance. An improvement of

design for better material removal (31.5% in Chapter 7) was achieved by adjusting the planar contact area of engineered abrasive pad.

It was found that laser generated abrasive pad can provide not the only superior surface finish, but also introduce less damage to the workpiece surface. More efficient chip flow and very little tool wear leading to a longer tool life was also observed. In particular, the engineered grits with symmetric shape (square frustum) exhibits superior performance over conventional grits (randomly shaped) and asymmetric grits (saw tooth). A good agreement between simulation and experimental results was found for surface roughness prediction, therefore provide good initial results for numerically studying engineered abrasives under planetary abrasive machining processes. Moreover, the evaluation of planar contact area also shows laser generated abrasives can provide significant advantages in material removal when designed with comparable planar contact area as conventional abrasive pad under specific applications, particularly when the abrasive contact geometry is designed to provide clearance in the cutting directions. Combining the findings above, a preliminary benchmark methodology was proposed for design of engineered abrasive pad, which enables the future optimization of engineered abrasive tool.

Publications

Y. Zhou, D. Axinte, P. Butler-Smith, E. Jessen, T. Norbygaard, Effects of novel rotary-abrasive finishing pad textures on the controlled 2-body abrasive wear of Type 304 stainless steel, Wear, 348–349 (2015) 89-97.

Acknowledgements

The author would like to particularly thank Professor Dragos Axinte for all his help and guidance throughout this research programme, Dr Paul Butler-Smith for his valuable suggestions on the research techniques and thesis writing, my family for their encouragement and support, my roommate Dr Qile li for the company through the tough days, Mr Mark Daine for his support on the experimental setup and laser ablation techniques, staffs from NMRC for their support on the nanoscale and microscale images of the research, and my colleagues in the Machining and Condition Monitoring research group at the University of Nottingham for their encouragement and help during this research programmes, special thanks for the EU DIPLAT project for their funding to support my research.

Contents

page

Chapter 1 Introduction **1**

1.1 Research background 1

1.2 Problem definition 4

1.3 Objectives of this study 6

1.4 Outline of this thesis 7

Chapter 2 Literature review **11**

2.1 Introduction to diamond material in grinding applications 11

2.1.1 Abrasives 11

2.1.2 Diamond structure and properties 13

2.1.3 HPHT Synthesis of diamond 16

2.1.4 Chemical vapour deposited (CVD) diamond 20

2.2 Grinding wear mechanism and effects of diamond abrasives on wear 24

2.2.1 Grinding material removal mechanisms 24

2.2.2 Abrasive size 31

2.2.3 Abrasive shape 32

2.3 Diamond grinding tool: design and modelling 33

2.3.1 Conventional diamond grinding tool 33

2.3.2 Engineered diamond grinding tool 36

2.3.3 Development of grinding modelling techniques 45

2.4 Summary and research gaps 47

Chapter 3 Methodology **51**

3.1 Methodology background 51

3.2 Selection of material for the generation of abrasive arrays and workpiece material for grinding test 52

3.3 Design and manufacture ordered abrasive pads 54

3.4 Procedures for the evaluation of plane grinding performance 58

3.4.1 Inverted test setup 59

3.4.2 Procedure for the characterization of abrasive tool 61
3.4.3 Identification of the workpiece surface topography and material removal rate 63
3.4.4 Evaluation of the material removal mechanism 64
3.5 Design and manufacture engineered abrasive pad for study of planar contact area 64
3.6 Approach for the evaluation of micro-hardness and subsurface damage 66
3.7 Approach to determine the planar contact area: linear scratch test setup 69
3.8 Modelling approach and validation for surface roughness prediction 71
3.9 Conclusions 74
Chapter 4 Evaluation of influence of grit geometry on the grinding performance 77
4.1 Characterization of abrasive grits 77
4.2 Preliminary evaluation of the influence of grit geometry on the finishing performance for engineered abrasive grits 81
4.3 Evaluation of tool wear mechanism 83
4.4 Response of surface topography and material removal rate to the engineered and conventional abrasive grits 86
4.4.1 Response of surface topography to the engineered and conventional abrasive grits 88
4.4.2 Response of material removal rate to the engineered and conventional abrasive grits 91
4.5 Material removal mechanism of scratched/ground surfaces 92
4.6 Conclusions and remarks 95
Chapter 5 On modelling of workpiece surface roughness when using rotary abrasive pads with engineered abrasive grits 97
5.1 Kinematic simulation of 2D single abrasive trajectory 98

5.2 3D material removal and surface updating algorithm 101
5.2.1 Abrasive grit model 102
5.2.2 Grit motion discretization 103
5.2.3 Material removal algorithm 105
5.3 Validation and discussion 106
5.4 Conclusions and remarks 110
Chapter 6 Evaluation of influence of planar contact area on the grinding performance 111
6.1 Characterization of abrasive grits 112
6.2 Tool wear mechanism 114
6.3 Evaluation of workpiece surface topography and material removal rate 116
6.4 Evaluation of micro-hardness and subsurface damage 121
6.5 Conclusions and remarks 124
Chapter 7 Design improvement of planar contact area for engineered abrasive pad 126
7.1 Determination of planar contact area and specific material removal 126
7.2 Evaluation of material removal 131
7.3 Conclusions and remarks 134
Chapter 8 Strategy of determining design parameters for engineered abrasive pad 136
8.1 Determination of grit geometry 136
8.2 Determination of planar contact area 137
8.3 Evaluation of the design 137
Chapter 9 Research outcomes and future works 139
9.1 Summary of research, findings and conclusions 139
9.2 Future work 142
References 145
Appendices 156

Appendix 1 Miler indices 156
Appendix 2 FEPA abrasive particle size 158
Appendix 3 Matlab code for surface profile simulation algorithm 160
Appendix 4 Visible grits on the Piano 220 pad 163
Appendix 5 Scratch data for Piano 220 166

Figures

Figure 1.1 Growth of global abrasive market [3] 1
Figure 1.2 SEM images of (a) synthetic diamond abrasive surface (b) CBN abrasive surface [9] 3
Figure 1.3 Flow chart representing the outline of the thesis and each Chapter 10
Figure 2.1 Variation of hardness for different types of abrasive material [24] 12
Figure 2.2 Cubic diamond structure showing the carbon atoms and crystal lattice [27] 13
Figure 2.3 Three common crystalline planes described by Miler indices [37] 16
Figure 2.4 A belt press produced in 1980s by KOBELCO (source: KOBELCO) 17
Figure 2.5 Pressure-temperature phase diagram for carbon [36] 18
Figure 2.6 Schematic illustration of belt press for high pressure high temperature (HPHT) diamond synthesis [46] 19
Figure 2.7 Selection of colorless HPHT synthetic crystals (0.50–0.69 ct) [52] 20
Figure 2.8 (a) Hot filament and (b) microwave plasma CVD diamond reactors [61] 21
Figure 2.9 CVD diamond application in gem industry (Source: Gemological Institute of America) 22

Figure 2.10 Commercially available single crystal CVD diamond in size of 8 × 8 × 2 mm (Source: Element Six [65]) 23
Figure 2.11 Polycrystalline CVD diamond showing correctional columnar structure and surface morphology [61] 24
Figure 2.12 Abrasion wear modes: (a) two-body abrasion; (b) three-body abrasion [66] 25
Figure 2.13 Groove cross-section demonstrating concept of grooving efficiency in: (a) micro-cutting, and (b) micro-cracking [68] 26
Figure 2.14 Influence of fracture toughness and hardness on wear resistance of materials [70] 28
Figure 2.15 Three orthogonal modes of abrasion [71] 29
Figure 2.16 Wear map showing different wear modes for a spherical indenter as a function of degree of penetration D_p and interfacial shear strength f [72] 30
Figure 2.17 Schematic representation showing the typical curves of wear vs. abrasive grain size [79] 31
Figure 2.18 Growth morphologies of diamond [1] 32
Figure 2.19 Electroplated diamond grinding wheel surface [15] 36
Figure 2.20 Arrangement of CBN grains on the engineered grinding wheel [97] 37
Figure 2.21 Manually positioned engineered grinding wheel and conventional electroplated grinding wheel [98] 38
Figure 2.22 Parameters of grain patterns [102] 39
Figure 2.24 Micro-arrays produced by laser ablation on CVD diamond [13] 41
Figure 2.25 Laser ablated micro-arrays with controlled cutting elements geometry [10] 42
Figure 2.26 Laser ablated solid diamond rotary micro-grinding tool [110] 43
Figure 2.27 Pyramid-shaped engineered abrasives generated by

microreplication [123] 43
Figure 2.28 (a) Normal and (b) tangential forces produced by diamond micro-arrays and electroplated elements [10] 44
Figure 3.1 Flow chart of methodology for the research programme 52
Figure 3.2 Variation of hardness for different types of abrasive material [24] 53
Figure 3.3 MD-Piano 80 grinding pad and enlarged abrasive element with SEM image of one grit buried in the bonding material 55
Figure 3.4 Schematic illustration of Concept image of engineered abrasive pad with ordered abrasive grits based on MD Piano pad 55
Figure 3.5 Examples of saw tooth and square frustum abrasive grit and their effective cutting directions under planetary movements 56
Figure 3.6 Schematic illustration of cross-hatch beam paths for generating engineered abrasive grits 57
Figure 3.7 Optical micrograph of one ordered abrasive pellet with square frustum grits 58
Figure 3.8 Setup of inverted grinding test 60
Figure 3.9 Seven abrasvie pellets cut from MD-Piano 80 glued on the resin dummy (left) and seven PLA micro arrays glued on the resin dummy 60
Figure 3.10 Example (a) SEM image of MD 80 abrasive pad surface after inverted grinding test; (b) BSE image of MD 80 abrasive pad surface after inverted grinding test 61
Figure 3.11 Example SEM images of (a) Embedded abrasive grit on the MD 80 abrasive pad surface (b) details of abrasive grit features 62
Figure 3.12 Example SEM image of (a) engineered abrasive pellet with square frustum grits (b) single square frustum grit 62
Figure 3.13 Examples of workpiece surface topography: generated by (a) conventional abrasive pad (MD 80) (b) engineered abrasive pad with square frustum grits after 5min of grinding 63

Figure 3.14 Schematic illustration of grit arrangement of new engineered abrasive pad 65
Figure 3.15 Buehler MicroMet micro-hardness tester-Vickers for micro-hardness testing and Vickers micro-hardness test scheme 68
Figure 3.16 Example image of machined subsurface characteristics of 304 stainless steel 68
Figure 3.17 Linear scratch test setup on Tegremin-20 system 70
Figure 3.18 Cross-sectional profile of a scratch generated by conventional abrasive grit and the spherical interpolation of this active grit to calculate planar contact area 70
Figure 3.19 Experimental Setup for capturing the slippage between abrasive pad and workpiece by PST-360 rotary senor 72
Figure 3.20 Wireless signal transmission system 73
Figure. 3.21 Example of analog angle data conversion to actual angle data 73
Figure. 3.22 Schematic illustration of grits arrangement and SEM image of the micro array for validation test (25 grits in total) 74
Figure 4.1 SEM images (before grinding) of (a) conventional abrasive surface (b) BSE of conventional abrasive pellet 78
Figure 4.2 SEM images (before grinding) of (a) conventional abrasive grit bounded by resin and (b) uncovered conventional abrasive grit .. 79
Figure 4.3 EDX analysis of (a) buried diamond grit (b) nickel coating on the diamond grit 80
Figure 4.4 SEM images of PLA engineered abrasive pad with: (a) square frustum girts (b) saw tooth grits 81
Figure 4.6 Surface micro-topography generated after 5 minutes of grinding by: (a) square frustum abrasive (b) saw tooth abrasives 82
Figure 4.7 The conventional abrasive surface after (a) 0 min (b) 10 min and (c) 20 min of grinding 84
Figure 4.8 (a) Conventional abrasive grit after 20min grinding; (b) High

magnification image of conventional abrasive grit after 20min grinding; (c) Uncovered conventional abrasive grit after 20min grinding; (d) High magnification image of uncovered conventional abrasive grit after 20min grinding 85
Figure 4.9 (a) Square frustum engineered grit after 20min grinding; (b) Higher magnification image at the grit corner 86
Figure 4.10 Variation of surface roughness generated by square frustum and conventional abrasives through the entire grinding process..... 87
Figure 4.11 Variation of material removal rate generated by square frustum and conventional abrasives through the entire grinding process 88
Figure 4.12 Surface topography generated by conventional abrasive grits after: (a) 10 minutes (b) 15 minutes (c) 20 minutes of grinding; Surface topography generated by square frustum engineered abrasive grits /pellet after: (d) 10 minutes (e) 15 minutes (f) 20 minutes of grinding 89
Figure 4.13 Scratched workpiece surface ground by: (a) conventional abrasive grits (b) square frustum grits after 20min of grinding 93
Figure 4.14 Void volumes after 5min of grinding for (a)conventional abrasive grits (b)square frustum grits 94
Figure 5.1 Schematic illustration of inverted test setup for modelling 98
Figure 5.2 Schematic illustration of kinematic system for plane grinding process 99
Figure 5.4 (a) geometry of square pyramid grit (b) parametrically described grit 102
Figure 5.5 (a) Transient projections of a single grit (b) transient orientation of a single grit 104
Figure 5.6 Projection view of grit on the workpiece surface 105
Figure 5.7 Algorithm for 3D updating the surface texture..... 106
Figure 5.8 Data of measured slippage $\boldsymbol{\varphi}(\boldsymbol{t})$ in Equation (5)..... 107

Figure 5.9 Workpiece surface topography for three spots (20mm, 40mm, 60 radially away from the disc centre): (a) experiment (b) simulation 108
Figure 5.10 Cross section profile of experimental and simulated surfaces: (a) 20mm (b) 40mm (c) 60mm radially away from the centre..... 109
Figure 5.11 Predicted and experimental surface roughness 109
Figure 6.1 SEM images (before grinding) of (a) BSE of MD-Piano 220 abrasive pellet (b) half buried single grit (c) uncovered MD-Piano 220 grit 112
Figure 6.2 SEM images of new design of PLA micro-arrays: (a) Micro-array structure (b) 50x50μm grit (c) 40x40μm grit 113
Figure 6.3 SEM images of wear mechanism of conventional abrasive grits (MD 220) (a) microfracture and cracking (b) flattening and cracking 115
Figure 6.4 SEM images of PLA grits after 20 minutes of grinding (a) 50x50μm grit (b) 40x40μm grit 116
Figure 6.5 Surface topography of workpiece surface after 20 minutes of grinding by (a) PLA 40x40μm (medium) (b) PLA 50x50μm (high) (c) Piano 220 (low) 117
Figure 6.6 Progression of workpiece surface roughness generated by three types of abrasive grits (Piano 220 (low), PLA 40X40 (medium) and PLA 50x50 (high)) 118
Figure 6.7 Material removal rate of workpiece generated by three types of abrasive grits (Piano 220 (low), PLA 40X40 (medium) and PLA 50x50 (high)) 120
Figure 6.8 Variation of micro-hardness beneath the machined workpiece surface generated by three types of abrasive grits (Piano 220 (low), PLA 40X40(medium) and PLA 50x50(high)) 122
Figure 6.9 SEM images of workpiece cross sections after 20 Minutes grinding (a) Piano 220 (low) (b) PLA 50x50μm (high) (c) PLA 40x40μm

(medium) 123
Figure 7.1 Example of visible grits on conventional abrasive pad (MD 220) after 20 minutes of grinding 127
Figure 7.2 Characterization of conventional abrasive grit (MD 220) protrusion and height 128
Figure 7.3 Example of scratch profile generated by conventional abrasive pad (MD 220) captured by Alicona 129
Figure 7.4 Schematic illustration of grit arrangement and cutting directions as well as SEM images of population 2 and 3 130
Figure 7.5 Material removal rates produced by conventional abrasive pad (MD 220) and the engineered Population 1 from the load controlled inverted grinding test at 30N 131
Figure 7.6 Scratch profile of a) Population 2 and b) Population 3 at 30N 133
Figure 8.1 Procedures of the preliminary benchmark methodology for design and evaluation of engineered abrasive pad 138

Tables

Table 2.1 Hardness of different types of abrasives [1] 12
Table 2.2 Classification of diamond [36] 15
Table 2.3 Theoretical cleavage energy of diamond for different crystalline planes [39] 16
Table 2.4 Grades of CVD diamond types [62] 23
Table 3.1 Specifications of two new engineered abrasive pad 65
Table 3.2 Surface preparation steps for micro-hardess and subsurface analysis 67
Table 3.3 Specifications of micro array for validation test 74
Table 4.1 Comparison between worn and fresh conventional grits 90
Table 7.1 Planar contact areas of exposed abrasive grits vs. engaged

abrasive grits on conventional abrasive pads (MD 220) at 10N, 20N and 30N applied loads 129
Table 7.2 Specific volume removed of 0.1mm scratch length for conventional abrasive pad (MD 220) and engineered, Population 2 and 3 at 30N load 132

Abbreviations

CBN	Cubic Boron Nitride
PCBN	Polycrystalline Cubic Boron Nitride
ADD	Advanced diamond dresser
SEM	Scanning Electron Microscope
BSE	Back-scatter detector
EDX	Energy-dispersive X-ray
PLA	Pulsed laser ablation
CVD	Chemical vapour deposition
PCD	Polycrystalline diamond
HPHT	High pressure high temperature
Nd:YAG	Neodymium-doped Yttrium Aluminum Garnet (laser)
FEPA	Federation of European Producers of Abrasives

Nomenclature

ω_1	angular speed of grinding platen (radi/s)
ω_2	angular speed of mover plate (radi/s)
ω_3	angular speed of cylindrical dummy (radi/s)
θ	angle travelled by abrasive particle (radi)
α	angle travelled by grinding platen (radi)
θ_0	initial value of θ (radi)
α_0	initial value of α (radi)
t	grinding time (s)

r_p	distance from grinding platen centre to an abrasive particle (mm)
x_p'	x coordinate of trajectory on the moving coordinate
y_p'	y coordinate of trajectory on the moving coordinate
$\varphi(t)$	slippage angle varies with time (radi)
$\Delta X \& \Delta Y$	mesh size in X and Y directions
H	protrusion of pyramid grit (mm)
H'	threshold of the protrusion height (mm)
w	half bottom side length of pyramid grit (mm)
γ	shift in orientation of the grit relative to the workpiece move coordinate (radi)
Z_w	surface heights of mesh points (mm)

Chapter 1

Introduction

1.1 Research background

As the rapid development of modern industry, the requirement of mass production with better accuracy, higher reliability and lower cost become one of the most important concerns for machining. With this increasing requirement of modern industrial technology and high performance products for part precision, surface integrity, production quality stability, grinding has played a major role [1]. As a result, during the last few decades, the demands of superabrasive grinding has strongly increased. These demands have grown in various industrial fields including optical, automotive, aerospace and life science etc. For example, CBN grinding technology can be used for both the manufacturing of aircraft engine components and land-based turbine engine components. Efficient manufacturing needs shorter production runs and longer cycle times, and electroplated CBN wheels are the preferred choice for high precision form grinding applications of this nature [2]. Figure 1.1 shows the increase of global abrasive market in recent years.

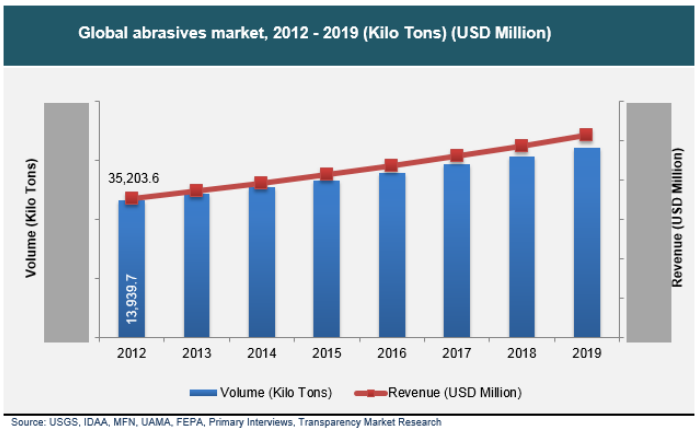
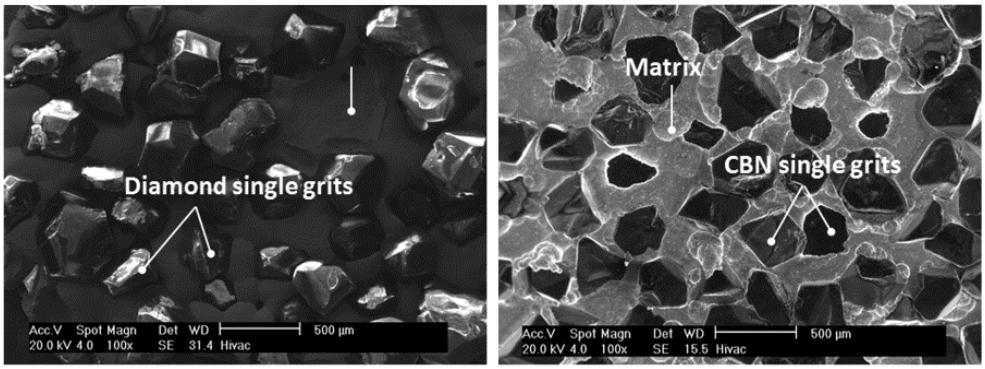


Figure 1.1 Growth of global abrasive market [3]

Although, grinding has been employed in manufacturing for more than 100 years, the earliest practice can be tracked back to Neolithic times [1]. With the development of current machining technology, grinding is now regarded as a modern process. Publications by Alden and Guest contributed to the understanding of the grinding process of by advancing it from an art into a science [4, 5]. Nowadays, grinding technology is highly developed process [6] according to particular product and process requirement. Modern grinding machines can be an inexpensive structure with a simple reciprocating table, or can be an expensive highly-integrated machine. Many grinding machines combine computer-controlled feed-drives and slide-way motions, allowing complex shapes to be manufactured free from manual intervention. Modern systems will usually incorporate algorithms to compensate for wheel and dressing tool wear process [7]. Programmable controls may also allow fast push-button set-up. Monitoring sensors and intelligent control introduce the potential for a degree of self-optimization [8].

Advances in productivity and tool performance have relied on increasing sophistication in the application of abrasives. As a result of the growing innovation on new synthesis technologies, the range of superabrasives employed in grinding tools has increased. Various synthetic diamond and boron nitride products are available for the development of tools for grinding applications: mono-crystalline and polycrystalline chemical vapour deposition diamond (CVD), mono-crystalline and polycrystalline high pressure high temperature (HPHT) diamond abrasives, polycrystalline diamond (PCD) and polycrystalline cubic boron nitride (PCBN) with metallic or ceramic binders. Due to the unique combinations of their exceptional mechanical and thermal properties (e.g. hardness, electrical conductivity, thermal stability) diamond and boron nitrides find suitable fields of application in precision grinding industries.



(a) (b)

Figure 1.2 SEM images of (a) synthetic diamond abrasive surface (b) CBN abrasive surface [9]

It is worthnoting that, although by controlling the growth conditions, especially time and nucleation density, it is possible to grow much higher quality diamonds with well-defined crystal forms. Nonetheless the shapes of the synthetic diamond abrasives are generally irregular and due to the process by which grinding wheels are made, the abrasives exhibit random cutting edges and different heights of protrusion from the bond, which result in a lack of process predictability (i.e. a stochastic distribution). In addition to this, the particle spacing also varies across the tool surface (Figure 1.2). The consequence of this random layout inhibits the optimal performance of individual abrasives in the process of material removal, and where particles are clustered, chip flow is negatively affected [10]. For this reason, researches have been reported to develop techniques for generating engineered abrasive tools with ordered grain patterns and shapes. Luo et al. utilized a LIGA-like process to fabricate abrasive pellets with regular micro cutting edges to investigate their wear and grinding characteristics [11]. Tsai et al. proposed a newly designed diamond conditioner with identically shaped tips with diamond edges of equal height, called the advanced diamond dresser (ADD), based on the forming of a pattern in a strong polycrystalline diamond material that is sintered at ultra-high pressure and high temperature [12]. Besides these two techniques, Butler-Smith et al. generated preferentially oriented micro-

crystallites/arrays made of thick-film CVD diamond-based structures by utilizing a laser ablation [13], this is a very versatile technique able to generate complex micro-scale shapes of the abrasives features. These studies have opened the possibility for the application of diamond abrasives with engineered grain patterns and shapes in precision grinding operations.

1.2 Problem definition

By adopting technologies such as laser ablation, abrasive tools can now be manufactured with abrasives having defined geometries, size and spacing. Studies on comparisons of the cutting performance between tools having ordered and conventional abrasives have been made, which reveal smoother workpiece surface roughness, less clogging/wear of abrasive grits and lower cutting forces [10,13]. Although, these studies have given an indication the advances of the engineered abrasive tools, reported results of the tests carried out are under condition of grinding were for linear tool paths. However this is not the general case for rotary abrasive machining processes with more complex planetary kinematics where the produced surface texture on the workpiece result as superposition on the abrasives having planetary trajectories; moreover, in this case the direction of the cutting edges change their orientation relative to the workpiece surface depending on their position on the cycloidal path. The literature has shown that there is lacking of researches have reported on the studying the application of engineered abrasives for abrasive machining processes with planetary movements (e.g. plane grinding) [109]. In particular, no literature has been identified on how the tool wear of the single abrasive (within the compounded grinding pads) and the workpiece material surface roughness and removal evolve with the

machining time under planetary movements for engineered abrasive tools.

Considering that the conventional abrasive pads have a high randomness in the distribution, orientation and protrusions of the abrasive grits, it is quite difficult to predict the resultant workpiece surface topography. Researches have been conducted to solve this problem in terms of statistical analysis, some models to establish the distribution function of the protrusion heights of grits on grinding wheel [14,15]. Moreover, models have been developed to try and idealize the geometry of the abrasives as primitive features (spheres, pyramids) [16].

Once the wheel model has been determined there are two predominant methods of generating the surface finish. In the kinematic simulation approach used by Nguyen and Butler [17] and Liu et al. [18] the trajectories of all cutting edges are determined. These trajectories are then combined together and trimmed in the appropriate manner to create a surface. In subtractive methods, used for example by Chakrabarti and Paul [19] as well as Darafon et al. [20], the cutting edge models are subtracted from a workpiece model in a stepwise manner as the cutting edges move along their trajectories. However, these existing models in grinding operations are difficult to be applied on plane grinding process with planetary movements since their complexity, i.e. planetary trajectories are affected by slippages; this is because, in contrast with grinding (linear tool path), plane grinding in a typical machine arrangement occurs under not only the planetary movements but also have some slippages between workpiece and abrasive pad, which results in more complex kinematics. In this respect some models have been developed to predict the trajectories of the abrasives of the rotary abrasive pads but they are traced only as points and not as true 3D protruding features [21, 22] and therefore, no real surface roughness parameters can be derived from this to be compared with the experimental results. No modeling has been

identified in the literature which geometrically simulate the workpiece surface roughness that results after plane grinding process with defined grit shapes in real (slippage) contact conditions between workpiece and abrasive tool.

1.3 Objectives of this study

The research work covered in this thesis aims at investigating the performance of plane grinding pads containing engineered diamond abrasive grits manufactured by Pulsed Laser Ablation (PLA), in particular, the influence of two major design parameters (grit geometry and planar contact area), and to develop a geometrical model to predict the surface roughness of workpiece material processed by these engineered plane grinding pads. The main objectives of the present work are:

1) To understand the influence of grain geometry on the performance of load controlled plane grinding process. Study the tool wear mechanism (e.g. microfracture, cracking and flattening) and its influence on the resulted surface topography and material removal rate. Study the material removal mechanism (e.g. cutting, wedge forming and ploughing), enabling the evaluation of finishing performances. Compare the results between conventional and engineered abrasive pad to evaluate the novel abrasive tool.
2) Based on the study of geometry in object 1, develop a 2D geometrical model to illustrate the movements of defined single/multiple grits (square frustum shaped), in order to determine the distribution of scratches (without considering the sample slip in the holder). Design an experimental set-up to capture the slippage of sample in the carrier, and integrate the

experimental slippage into the 2D geometrical model. This allows the full description of scratches on the workpiece material. Develop an algorithm based on Z-map method (i.e. a spatial-decomposition or spatial-partitioning approach) for simulating the workpiece surface profile along the 2D scratches. Predict the surface roughness by utilizing the resultant surface profile data.

3) Understand the influence of grain planar contact area on the performance of load controlled plane grinding process. Evaluate the engineered abrasive pads with different total planar contact area by examination of surface properties have been analyzed in object 1. In addition, set up procedures to capture subsurface damage and micro hardness, which allows the further study of surface integrity.
4) Understand the working population of abrasives in relation to the abrasives visible on the surface of a conventional abrasive pad to enable the determination of planar contact area; in particular study the effects of abrasive planar contact area, contact geometry and overlap in the cutting direction on the material removal rates for conventional and engineered abrasive pad.

1.4 Outline of this thesis

This section briefly outline the content in each chapter. The plan of this thesis is as follows:

1) Chapter 1 serves as an introduction to the study; in particular stating in brief the research which was already done in the field of study, and evaluating the research gaps which would be beneficial to exploit in order to achieve the aims and objectives of this research.

2) Chapter 2 covers a detailed literature review related to the field of study by including the introduction of diamond material, wear mechanism of abrasive tools, material removal mechanism and the techniques to manufacture ordered diamond abrasives. Besides this, it will also cover the development of modelling approach for grinding.
3) Chapter 3 includes the methodology, equipment and techniques used throughout the research in order to conduct experiments, modelling and analysis necessary for the research aims achievements.
4) Chapter 4 includes characterization of abrasives with morphology and their wear mechanism during the operation. Moreover, this chapter presents how the surface roughness and material removal rates evolves with time, and the influence of tool wear mechanism on them. Comparison has been made to evaluate the surface topography and material removal mechanism for symmetric (square frustum) and randomly shaped (MD-Piano 80) grits, enabling the evaluation of their influence of grit geometry on the grinding performance.
5) Based on the results in Chapter 4, square frustum grits was selected to develop a geometrical model that can predict the surface roughness of machined surface. In particular, it aims at presenting the algorithm of how to simulate the scratches in 2D form and then create the 3D surface profile data along these scratches. This chapter also includes the comparison between the simulated and experimental surface roughness, in order to validate the model.
6) Chapter 6 includes the evaluation of three abrasive pads with different planar contact area (MD-Piano 220, two engineered abrasive pad with square frustum grits) on their grinding

performance. Procedures used in Chapter 4 are applied, moreover, further analysis on subsurface microstructural damage and variation of micro-hardness after grinding operation are also presented.

7) Chapter 7 covers the determination of abrasive planar contact area for conventional abrasive pad in terms of circular interpolation by linear scratch test. An assessment of material removal of conventional abrasive pad and engineered abrasive pad with equivalent planar contact area was made to quantitatively evaluate the improvement of material removal rate by adjusting the planar contact area.
8) Chapter 8 briefly summaries the approaches and criteria to determine the two major design parameters (grit geometry and planar contact area) studied in Chapter 4 to 7. A preliminary benchmark methodology was developed for design of engineered abrasive pad.
9) Chapter 9 covers a summary of the discussion of the research work, particularly outlining the outcomes of the project and how those could be beneficial for cutting edge industrial applications. In addition, it shows how the research outcomes in chapter 4 to 7 meet the objectives in chapter 1. It also includes a future work section.

Figure 1.3 presents a flow chart showing the relation between each chapter. As mentioned above, characterization of abrasive grains have been conducted through the operation process. Analysis on their geometry and wear mechanism is a necessary step to build the correlation to workpiece surface topography and material removal rate. After that, the material removal mechanism is examined to evaluate the finishing performance, which leads to a better understanding of effects of abradant geometry on the two-body removal. Based on the results above, the

ordered abrasive pad has controlled features, it is possible to simulate the process and predict surface roughness. Therefore, a geometrical model is developed to simulate the resultant surface profile after grinding by ordered abrasive pad with square frustum grits for surface roughness prediction, the results are validated by experiments. In addition to grit geometry, planar contact area between abrasives and workpiece material is also examined as an important factor that can influence the grinding performance. A study of effects of planar contact area between abrasive and workpiece on material removal is then carried out to enhance the understating of the relation between visible abrasives and engaged abrasives and improve the design of planar contact area for ordered abrasive pad.

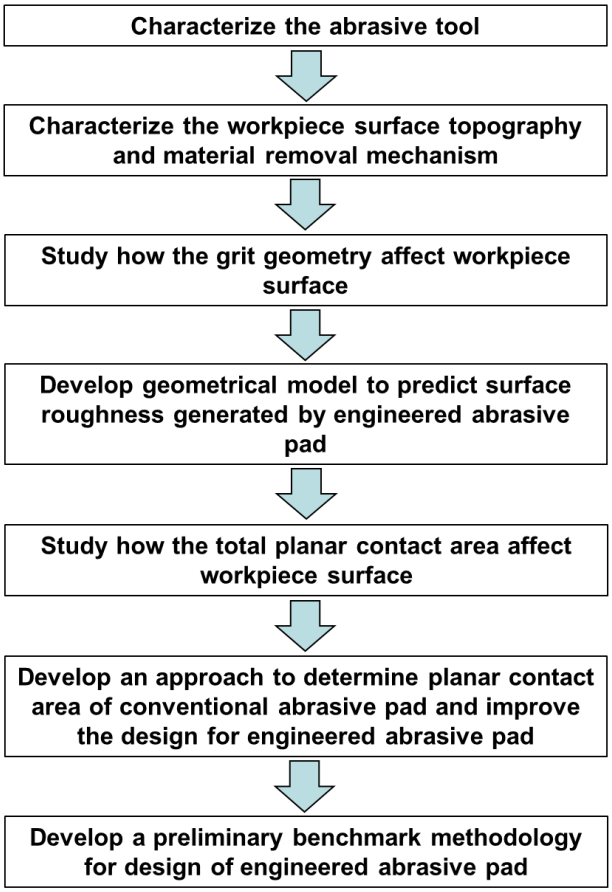


Figure 1. 3 Flow chart representing the outline of the thesis and each Chapter

Chapter 2

Literature review

2.1 Introduction to diamond material in grinding applications

This section presents a comprehensive literature review on the characteristics of diamond and synthetic diamond materials. A thorough review is made of diamond in precision and micro-grinding tools, covering the correlations between diamond characteristics and abrasive machining applications, in order to demonstrate the advantages of diamond material in the application of grinding process. The processes (e.g. HPHT & CVD) used to produce conventional diamond abrasive grits and non-conventional thin film diamond material (used to produce engineered abrasive surface) are reviewed, which enables the understanding of the influence of particular manufacturing process on the characteristics of diamond material and their usage for different types of grinding tools.

2.1.1 Abrasives

In grinding industry, the abrasive grains are mainly divided into two groups:

- Conventional abrasive including silicon carbide (SiC) and aluminum oxide (Al_2O_3) etc.
- Superabrasives including diamond (either nature or synthetic) and cubic boron nitride (CBN) etc.

For grinding abrasives, the most important property is hardness and it is the criteria to divide these two groups. Hardness will directly influence the wear characteristics of abrasives and therefore the grinding performance. It is important that hardness is retained at high temperatures and that the abrasive does not react chemically or diffuse too readily into the workpiece material [1]. Some typical values of hardness for different types of abrasives are shown in Table 2.1:

Table 2.1 Hardness of different types of abrasives [1]

Superabrasives	
Diamond	64GPa
Cubic boron nitride(CBN)	45GPa
Conventional abrasives	
Silicon carbide	24.5GPa
Aluminum oxide	13.5-22.3GPa
Cemented carbides	14-18GPa
Quartz	0.78GPa
Glass	0.3-0.5GPa

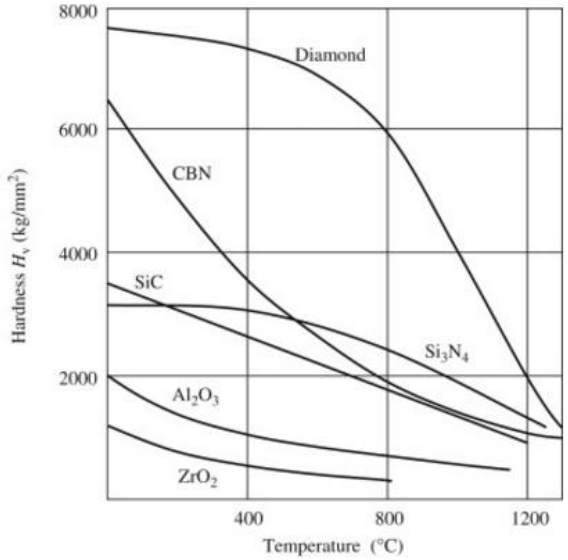


Figure 2.1 Variation of hardness for different types of abrasive material [24]

It is shown that, diamond is the hardest abrasive followed by CBN, other conventional abrasives possess much lower hardness compared with

these two. In most cases, hardness of abrasives will be reduced with temperature [23]. According to Figure. 2.1, diamond and CBN are still the two hardest abrasive material at high temperature, and it explained why superabrasives could be utilized for high temperature conditions.

2.1.2 Diamond structure and properties

It is well known that diamond is a metastable allotrope of carbon [25], in which the carbon atoms are bonded highly compact in a FCC (Face-centered cubic) crystal structure called diamond lattice (Figure 2.2). In a diamond cubic, all the carbon atoms are arranged tetrahedrally [26], where each carbon atom is bonded to four other carbon atoms. This tetrahedral arrangement provides a strong and solid unit structure which spread across the whole diamond structure. Furthermore, this unique structure results in the extraordinary hardness and stiffness for diamond. Besides this, the strong covalent bonding between carbon atoms requires a lot of energy to separate, which accounts for its chemical inertness and high melting and boiling point. Those properties enable the various industrial applications of diamond in cutting, grinding/polishing, as well as the scientific applications in diamond knives and diamond anvil cells.

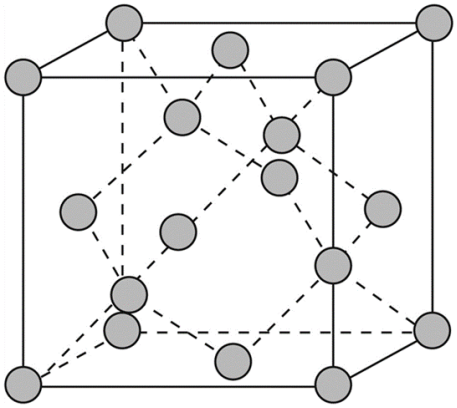


Figure 2.2 Cubic diamond structure showing the carbon atoms and crystal lattice [27]

The covalent bond between each carbon atom is equal to 1/4 of the width

of the unit cell i.e. 0.154nm. There is a total of eight whole carbon atoms located in one cubic cell (Figure 2.2): eight 1/8 at the corners, six 1/2 at the faces and four inside the cubic cell. Combining the atomic mass of carbon and the total numbers of carbon atoms in one cubic cell, also by considering the atomic packing density, the theoretical density of pure diamond can be determined as 3.53 g/cm^3 [28,29]. In real situations, the density of diamond is ranging from 3.15 to 3.53g/cm^3, due to the impurities and voids [30].

Graphite is the most stable allotrope of carbon, where each of the carbon atom is bonded to three other carbon atoms which forms regular hexagons. These hexagons extend in two dimensions to construct a planar hexagonal lattice structure. Compared to graphite, diamond is relatively unstable with a negative free-energy change of 2.88kJ/mol at room temperature and atmospheric pressure [31]. Although the rate of transformation of diamond to graphite is infinitely small under room temperature at atmospheric pressure, if the temperature is increased to 700°C in the air [32], the transformation (oxidation) will initiates, while in the absence of oxygen, e.g. in a flow of high-purity argon gas, the initiation of transformation occurs around 1700°C [33,34]. In addition, the initiation temperature will increase at high pressure, under 20GPa the transformation temperature can be increased to 2500°C [35].

The presence of impurities (e.g. nitrogen, boron and hydrogen) in diamond, even a small amount, can influence the diamond properties dramatically. As a result, it is important to classify diamond in terms of composition of impurities, in order to determine its properties accurately. In general, there are two types of impurities can be found in both natural and synthetic diamond:

1. Foreign atoms replace the carbon atoms in the lattice structure.
2. Individual particles which are not inside the diamond lattice structure.

For the first type of impurities, nitrogen and boron (they are neighbors of carbon in the periodic table) are two major impurities can be found in the lattice structure. Based on the type and amount of impurities, a classification of diamond has been made in Table 2.2

Table 2.2 Classification of diamond [36]

Type	Prevalence (Natural)	Impurities	Colour
Ia	98%	Clustered nitrogen atoms < (3000pm)	Colourless, Light yellow
Ib	0.1%	Scattered nitrogen atoms < (500ppm)	Yellow, Orange, Brown
IIa	1-2%	Highly pure carbon atoms	Colourless, Pink, Yellow, Brown , Purple
IIb	0.1%	Isolated boron atoms < (0.5ppm)	Blue, Grey

It is well known that diamond is an anisotropic material, which implies it has different properties in different directions. According to the lattice structure discussed previously, carbon atoms inside all the lattices can construct regular planes separated by equal distances. In order to designate these crystallographic planes, Miller indices (Appendix 1) is used to specify the orientation of the planes. The three major crystallographic planes (See Figure 2.3) described by Miler indices are (100), (110) and (111), and for each crystalline plane the mechanical and physical characteristics of diamond are different.

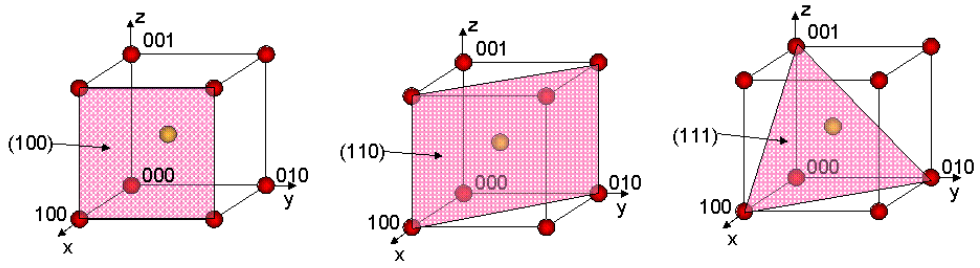


Figure 2.3 Three common crystalline planes described by Miler indices [37]

Table 2.3 listed the cleavage energy with respect to three major crystalline planes. It is shown that plane (111) is the dominant cleavage plane compared to the other two, however, it is also possible to fracture on other planes by orienting properly [38].

Table 2.3 Theoretical cleavage energy of diamond for different crystalline planes [39]

Crystal planes	Angle between plane and (111)	Cleavage energy
(111)	0° and 70°32′	10.6
(110)	35°16′ and 90°	13.0
(100)	54°44′	18.4

2.1.3 HPHT Synthesis of diamond

Although natural diamonds have various superior properties that can be utilized for abrasive machining applications, most of the diamond materials employed in industry are synthetic ones. There are two general types of methods for diamond synthesis, which are HPHT (mainly used for conventional irregular shaped abrasives) and CVD (can be utilized to generate diamond film for engineered abrasives) methods.

In 1797, it was discovered that diamond is another form of carbon [40],

which resulted in many attempts to convert carbon into diamond. Between the late 1800s and early 1900s [41,42], there are some successful cases of conversation were reported, however in 1928 Sir Charles Algernon Parsons [43] suggested that no synthetic diamond has been successfully produced up to that date, and the cases reported so far were likely synthetic spinel [44].

In 1955, General Electric is the first to report their achievement on reproductivity of the conversion of carbon into diamond [45], while it was also achieved by AESA in Sweden and Institute for High-Pressure Physics in the Soviet Union in 1950s. GE have successfully achieved the pressure above 10 GPa and temperature above 2000 °C by the invention of the "belt" press (Figure 2.4). The key step to manufacture the synthetic diamond in the "belt" press is to dissolve the carbon in the suitable solvent i.e. nickel, cobalt and iron, these metal solvent can reduce the pressure/temperature requirement for nucleation of diamond. According to the phase diagram of diamond-carbon (Figure 2.5), when the carbon-metal solution is cooled, carbon will be deposited as diamond within diamond growth region.



Figure 2.4 A belt press produced in 1980s by KOBELCO (source: KOBELCO)

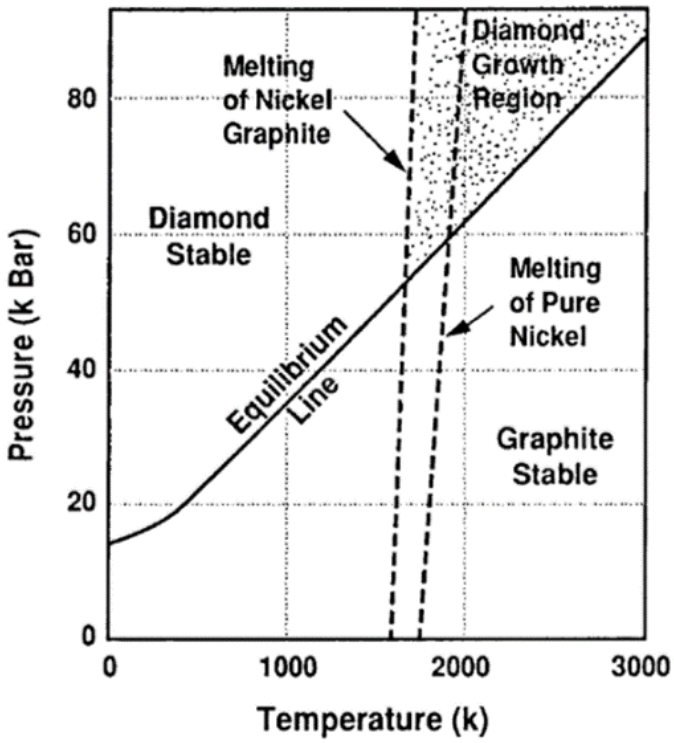


Figure 2.5 Pressure-temperature phase diagram for carbon [36]

The method GE proposed to produce diamond from carbon is called high pressure high temperature (HPHT) method, which aims at reproducing the process of diamond growth in natural. Figure 2.6 shows the scheme of typical belt press HPHT process. Diamond seeds are placed in the growth cell chamber with high-purity carbon and metal solvent (nickel, cobalt or iron). The chamber is then heated above 1400 °C and melts the metal solvent, high-purity carbon dissolved in the molten metal. The upper and lower anvils apply high load and transmitted by pressure transmitting medium to produce high pressure in the chamber. As the pressure released, the dissolved carbon precipitates on the diamond seeds and form synthetic diamonds [47].

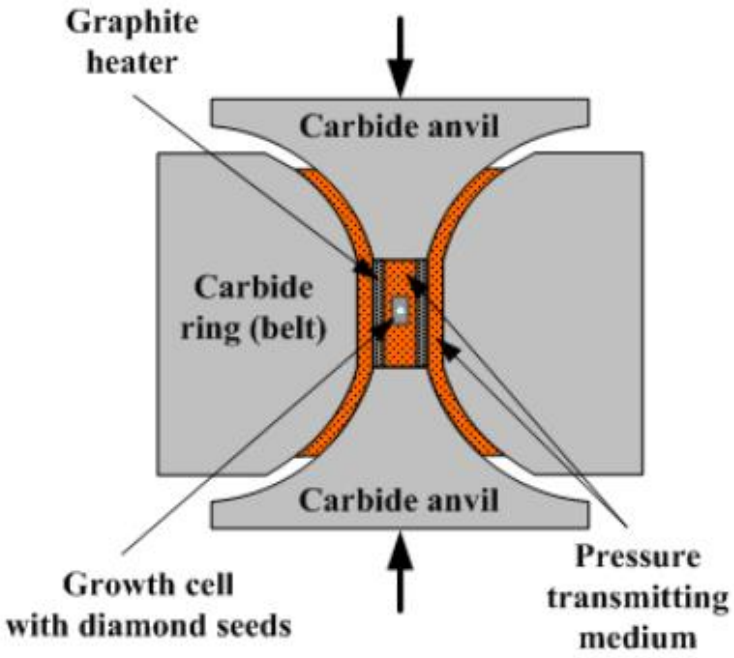


Figure 2.6 Schematic illustration of belt press for high pressure high temperature (HPHT) diamond synthesis [46]

As developments of HPHT method for diamond synthesis since 1950s, the commercial application of HPHT synthetic diamond products has grown rapidly. There are also many improvements has been made on synthesis apparatus, the control of the HPHT process parameters and post synthesis processes. Based on the developments up to date, HPHT synthetic diamond crystals are generally more superior in crystalline quality and consistency than naturally occurring diamonds, especially, type IIa diamond crystals synthesized by advanced control of impurities and crystal defects have extremely high crystalline quality [48-51]. Figure 2.7 shows an example of HPHT synthetic diamonds demonstrating good crystalline consistency and minor impurities.



Figure 2.7 Selection of colorless HPHT synthetic crystals (0.50–0.69 ct) [52]

HPHT synthesis has facilitated the development and enabled the production of polycrystalline diamond (PCD), which are characterized by randomly orientated crystals exhibiting various degrees of intergrowth and supported by a binder phase [46]. This feature allows the recreation of micro cutting edges during the grinding operation, which is helpful to maintain the tool cutting efficiency by refreshing the cutting edges.

2.1.4 Chemical vapour deposited (CVD) diamond

In the 1950s, besides the development of HPHT synthesis method, initial researches on the low pressure conditions using vapour deposition method for diamond synthesis started in the United States and Soviet Union. Eversole reported the success vapour deposition of diamond on the diamond substrate in 1953 [53]. In 1968, Angus reported the experiments on reproducing the diamond film deposition, while around the same time Deryagin and Fedoseev achieved the synthesis of diamond films on non-diamond substrates (e.g. silicon and metals) [54,55]. However, the CVD synthesis methods did not really bring to the table until the Japanese researchers Seiichiro Matsumoto and Nobuo Sekata optimized several deposition methods to produce diamond and

significantly accelerated the growth rate of diamond films in 1980s[55-58].

Similar to HPHT process, CVD process also utilizes diamond seeds on which the diamond precipitates and grows. In general, the CVD process including the elements of diamond seeds, the mixture of hydrocarbon gas (e.g. CH_4) and hydrogen, and method of activating the gas mixture to generate reactive carbon and hydrogen species [59]. The gas mixture is activated by an energy source (e.g. hot filament, microwave plasma) in a vacuum chamber leading to the release of carbon atoms from gas mixture molecules. After that, the carbon atoms are deposited down toward the cooler substrate for precipitation and growth.

Figure 2.8 shows the two most common types of methods to generate CVD diamond i.e. hot filament and microwave plasma. In the hot filament setup a high temperature filament is placed close to the seeds on the substrate in the chamber. The gas mixture in introduced into the chamber over the filament, and the filament is heated to 2000–2500 °C simultaneously activating the gas mixture and heating the seed diamonds. In the microwave plasma setup, the hot filament is energy source is replaced as a microwave generator to form a high energy plasma over the diamond seeds [60].

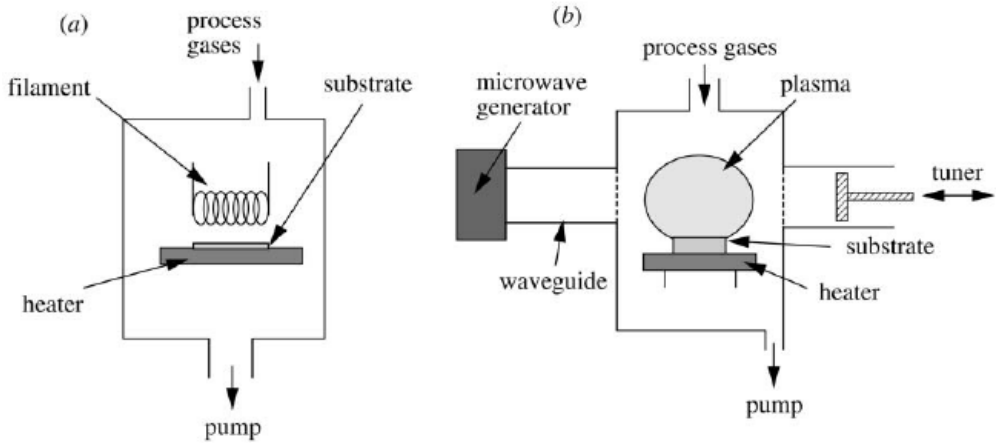


Figure 2.8 (a) Hot filament and (b) microwave plasma CVD diamond reactors [61]

Although the HPHT process is still more popular to manufacture synthetic diamond for industrial applications due to its high quality and capability of mass production, CVD process is proved to be simple and flexible, therefore suitable for both industrial and research purposes. The advantages of CVD process are the ability to produces synthetic diamond over a large area and on various substrates. Moreover, it does not require high pressure to produce, which reduce the cost of production compared to HPHT requiring the high pressure condition and catalysts.

As the development of CVD diamond synthesis in terms of size and quality, many advances has been achieved in the gem industry (Figure 2.9). Since 2008, CVD synthetic diamonds of improved color and quality have gone into limited commercial production [59].



Figure 2.9 CVD diamond application in gem industry (Source: Gemological Institute of America)

In addition to the gem industry, the very low chemical reactively and its high resistance to corrosion and wear also provide CVD synthetic diamond with various engineering applications. Table 2.4 shows the grades of single crystal and polycrystalline CVD diamond classified by grain size. The grain size depends on the synthesis conditions, substrate and layer thickness. CVD diamond with the layer thickness greater than 50 μm can be removed

from the substrate as free standing solid diamond material.

Table 2.4 Grades of CVD diamond types [62]

	Crystal size	**Appearance**
Single Crystals	Wide range	Clear-colored
Microcrystalline Diamond (MCD) films	0.5–50 μm	Black - clear
Nano Crystalline diamond (NCD)	10- 500 nm	Black
Ultra-nano crystalline diamond (UNCD)	5-10 nm	Black

Both of single crystal and polycrystalline CVD diamond have increasing demand for mechanical applications and proved to have good performance in precision machining where required superior surface finish [63,64]. They can offer a cost effective alternative to either natural diamond or larger synthetic diamond, which cover the applications of defined edge tools and tool coatings. For single crystal CVD diamond, the material size available is generally up to 8 x 8 x 2 mm (Figure 2.10).

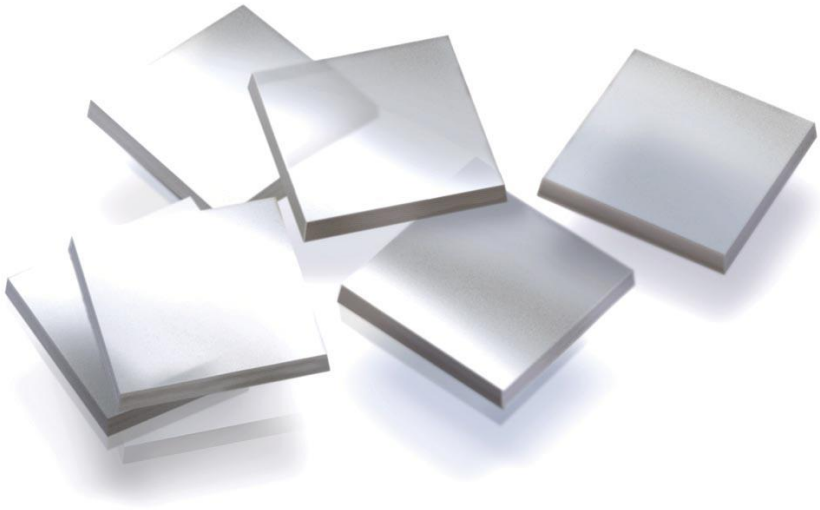


Figure 2.10 Commercially available single crystal CVD diamond in size of 8 × 8 × 2 mm (Source: Element Six [65])

Polycrystalline CVD diamond is specifically characterized by its diverging columnar structure in the CVD growth orientation. The structure culminates in randomly orientated morphological features growth results in a cubic feature (Figure 2.17).

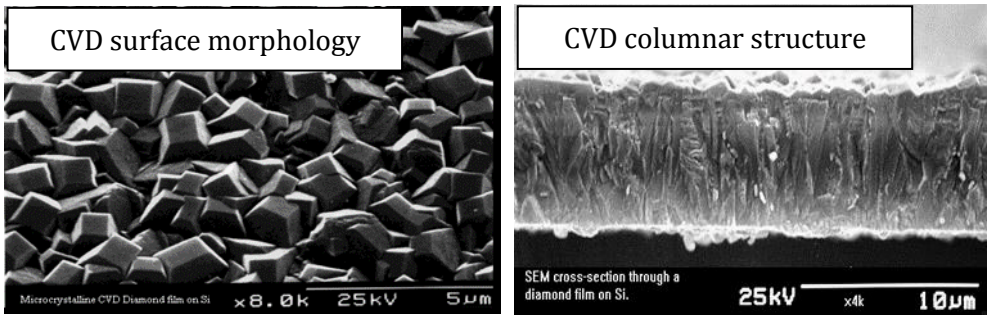


Figure 2.11 Polycrystalline CVD diamond showing correctional columnar structure and surface morphology [61]

2.2 Grinding wear mechanism and effects of diamond abrasives on wear

2.2.1 Grinding material removal mechanisms

Grinding is an abrasive machining process which is generally the last step for manufacturing engineering components. It can produce very high surface finish and accurate dimension by utilizing the relative motion between abrasive grains and workpiece material. Abrasive machining process, in terms of tribology, is referred to abrasion process, and can be classified as two categories: a) two-body abrasion b) three-body abrasion. Figure 2.12 shows the two abrasion modes proposed by Rabinowicz [66].

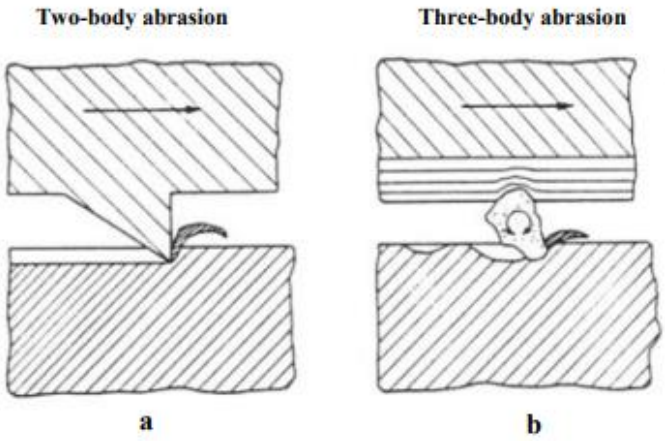


Figure 2.12 Abrasion wear modes: (a) two-body abrasion; (b) three-body abrasion [66]

In the two-body abrasion, the abrasive grains are fixed (bonded) on the abrasive tool (e.g. grinding, honing), and material in removed by pure sliding. The abrasive wear induced in two-body abrasion is groove form of wear. In the three-body abrasion, loose abrasive grains are employed between the tool and workpiece surface. In this case, abrasive grains are free to slide and rotate, contacting with other grains and both tool and workpiece surface. Although, three-body abrasion is less efficient due to the energy loss caused by free motion and collision, it also have the advantage that new cutting edges can be introduced when free rotating [23]. In order to understand the abrasion mechanism and its influence in the grinding process, various models has been developed to study the removal mechanism.

2.2.1.1 Simple abrasive wear model

This simple model is developed by assuming an idealized rigid conical grit sliding across a workpiece surface. The volume of removed material can be described as [66],

$$\mathrm{V} = \frac{kPL}{H} \tag{2.1}$$

where L is the transverse displacement of the grit, H is the hardness of the

material, and P is the normal load applied on the grit. K is the wear coefficient and defined as:

$$K = \frac{2\eta}{\pi tan\theta} \tag{2.2}$$

where θ is the attack angle between grit and workpiece surface, η is the fraction of material displaced from the groove.

This model is varied by experiments conducted by silicon carbide grit abraded on different types of pure metals [67]. However, when tested with other materials, the correlation with material hardness does not match the model very well, which reveals that other material properties also affect the wear resistance in real situations.

2.2.1.2 Deformation wear models

As discussed in 2.2.1.1, other factors can result in a deviation of experimental data compared to simple model predicted data. It can been seen in Figure 2.13, in real cases, stress fields in the deformed material can cause material pile-up and sink-in on the groove profile, which deviate from the predicted profile (dashed line).

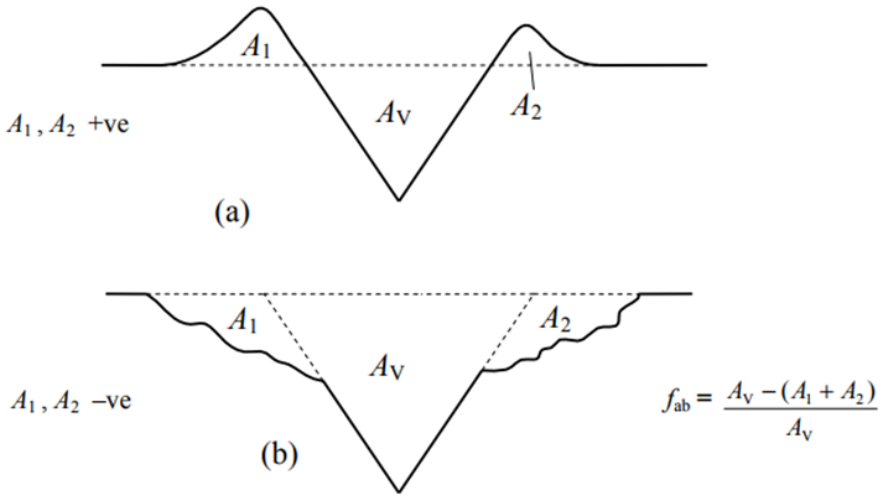


Figure 2.13 Groove cross-section demonstrating concept of grooving efficiency in: (a) micro-cutting, and (b) micro-cracking [68]

Zuhm Gahr [69] classifies wear into four categories including micro-cutting, micro-ploughing, micro-fatigue and micro-fracture. Micro-ploughing involves formation of grooves without direct removal of material, while micro-cutting separates the material as microchips and cut away from the surface. In real situations, there are always a combination of the two mechanisms to some extent. As a result, an abrasion mechanism model is derived in terms of efficiency due to the combination of wear mechanisms. The abrasion efficiency is given as follows:

$$f_{ab} = \frac{A_V - (A_1 + A_2)}{A_V} \tag{2.3}$$

where f_{ab} is the ratio of material removed to the scratch volume, A_v is the measured scratch area relative to the original surface, A_1 and A_2 are the areas of the pile-up ridges on the both sides of the scratch. The values of A_1 and A_2 can be negative if the micro-cracking occurs for brittle material (Figure 2.13 b). f_{ab} tends to be less than 1 for ductile material as the pile-up feature is dominant, while for brittle material can be greater than 1 as sink-in feature may occurs due to micro-cracking. It has been found that the values of f_{ab} is ranging from 0.15 -1 for 30 types of metals and alloys (ductile material) [69]. In these cases, efficiency can be estimated as,

$$f_{ab} = \ 1 - \left(\frac{\varphi_{lim}}{\varphi_s}\right)\sqrt[3]{\frac{8H}{H_{def}}} \tag{2.4}$$

where φ_{lim} represents the effective strain required for cutting, φ_s is the effective strain imposed by the scratch, H is the unreformed material hardness, H_{def} is the hardness of the deformed material or wear chips. Equation (2.4) is only valid when $\varphi_s \geq \varphi_{lim}$ ($f_{ab} > 0$), otherwise no material removal is possible.

The linear wear rate per unit length w can be given as,

$$w = C \cdot f_{ab} \cdot \frac{P}{H_{def}} = C \cdot \left[1 - \left(\frac{\varphi_{lim}}{\varphi_s}\right)^{\sqrt[3]{\frac{8H}{H_{def}}}}\right] \cdot \frac{P}{H_{def}} \qquad (2.5)$$

where p is the applied surface pressure and C is a geometrical factor that takes into consideration the geometry of the contact and the average shape of the abrasive particles. Equation (2.5) reveals that the wear is decreased with the increasing H_{def} (deformed material hardness) or φ_{lim} (capacity for plastic deformation).

Unlike the abrasion of ductile metals and alloy, the fracture toughness becomes more important for abrasion of brittle material when micro-cracking occurs. For these conditions, the model to describe the wear rate w as function of unreformed material hardness H and fracture toughness K_c is given as [70],

$$w = C \cdot \frac{D^{\frac{1}{2}} p^{\frac{5}{4}}}{K_C^{\frac{3}{4}} H^{\frac{1}{2}}} \qquad (2.6)$$

where C is a constant and D is the abrasive size. Figure 2.14 shows how the toughness and hardness affect the wear resistance.

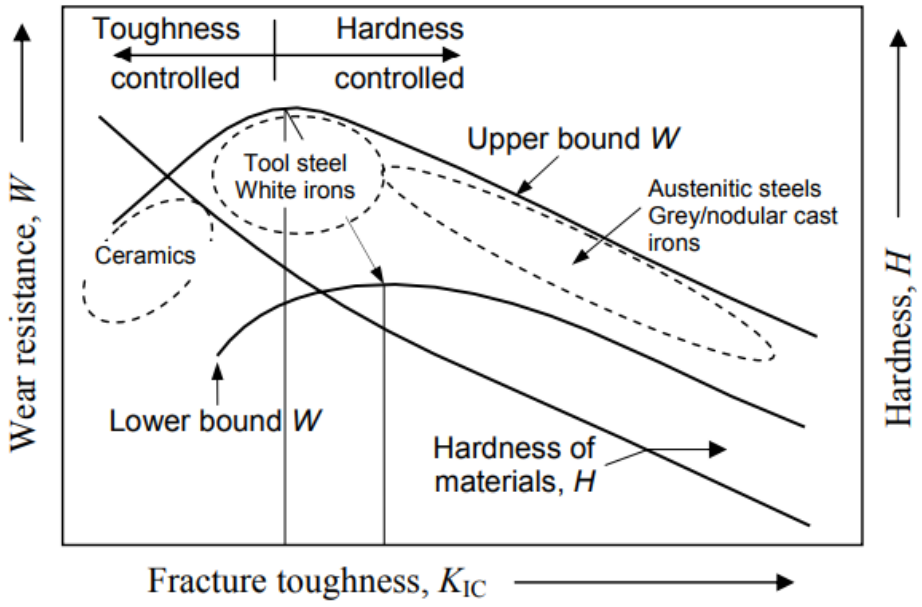


Figure 2.14 Influence of fracture toughness and hardness on wear resistance of materials [70]

It is noteworthy that, in equation (2.6) the applied pressure p does not increase with the exponent of 1 but 5/4. This is because in the micro-cracking dominant mode, the grit pressure can cause a non-linear increase in the tendency to separate the surface by lateral cracking [70].

2.2.1.3 Orthogonal cutting models

The deformation models discussed in 2.2.1.2 mainly focused on the material properties, while the abrasive shape and geometry of contact are described by an empirical constant C. Challen and Oxley proposed a different model using two-dimensional slip-line fields to predict corresponding coefficient of friction and wear rate [71]. The three types of wear mechanisms described by the model are illustrated in Figure 2.15.

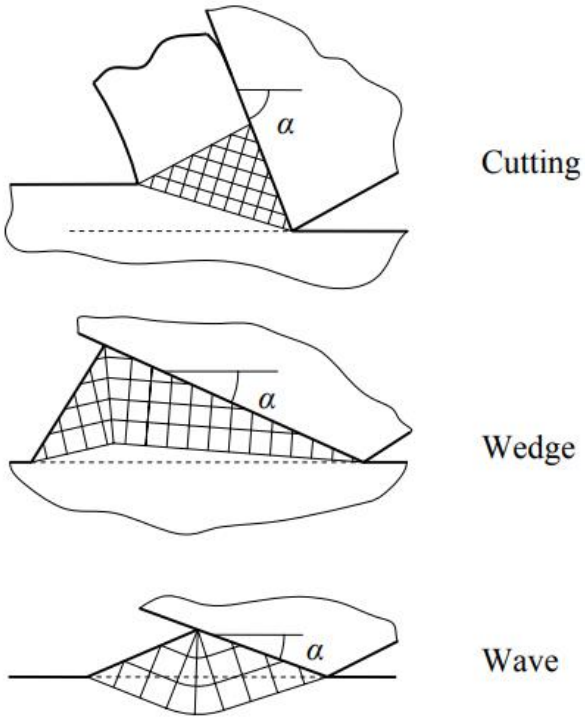


Figure 2.15 Three orthogonal modes of abrasion [71]

This model enables the estimation of forces and the conditions of cutting initiation. It was reported that the cutting is likely to happen at attack angle α as small as 22°. This finding is important as the average attack fall

into this region. As a result, the abrasion mechanism is very sensitive to the variation of attack angle, and only a small change can cause a transition from moderate wedge/wave modes to aggressive cutting modes [71].

2.2.1.4 Wear map

Although the orthogonal cutting model can be used to study the different interactions between asperity and surfaces, it is limited to two-dimensional conditions. In real cases, the asperity is not three-dimensional and not necessarily contact with the surface perpendicularly. A test with spherical indenter was carried out by Hokkirigawa and Kato [72] to experimentally observe the wear modes with the parameters of degree of penetration D_p and interfacial shear strength f for brass, cast iron and stainless steel. The three wear regimes are classified as cutting, ploughing and wedge forming as shown in Figure 2.16. It was found that, when interfacial shear strength f is small (i.e. well lubricated conditions), the effective attack angle for initiation of cutting is close to the estimation of orthogonal cutting model i.e. around 22°.

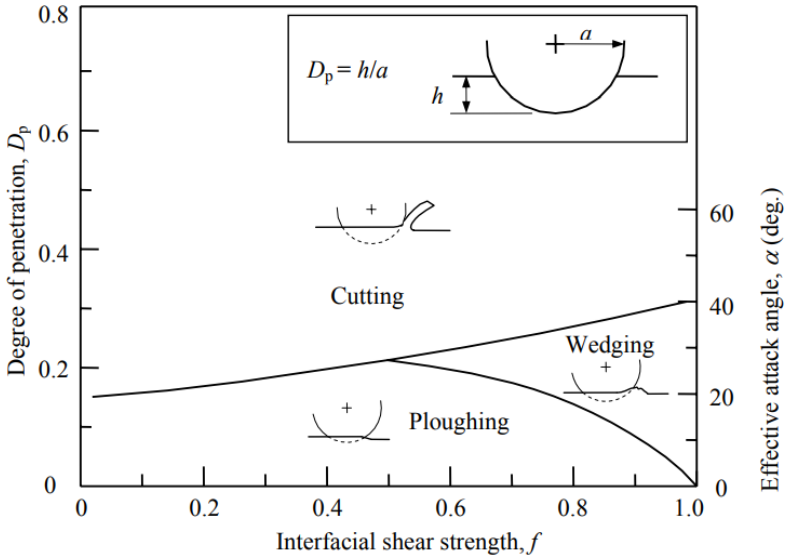


Figure 2.16 Wear map showing different wear modes for a spherical indenter as a function of degree of penetration D_p and interfacial shear strength f [72]

2.2.2 Abrasive size

In general, abrasive grit sizes are measured by the fraction of grits that can pass through a series of vibrating meshes or screens having a specified numbers of holes per square inch [23]. There are numerous international standards have been developed to define the grain size by sieving, a table of FEPA (Federation of European Producers of Abrasives) standard is listed in Appendix 2.

The effect of abrasive particle size on the material wear rate has been studied extensively over the last several decades [73-80]. It was reported that there is a linear correlation between abrasive particle size and mass loss for small abrasives [74]. The wear rate will increase with the increasing abrasive particle sizes until it reaches a critical particle size (CPS), after which the relationship will change accordingly. Figure 2.17 illustrates three trends of wear rate above the CPS conditions [79]. In the trend 1, the wear rate still increase but becomes slower with the particle size increase (curve 1) [78]. In the trend 2, wear rate does not vary with particle size [73-75, 81]. In the trend 3, wear rate decrease linearly with the increasing particle size [82]. There are many hypotheses to explain this phenomenon [73, 76, 79 , 82, 83], however, there is still no explanation generally accepted by the entire scientific community.

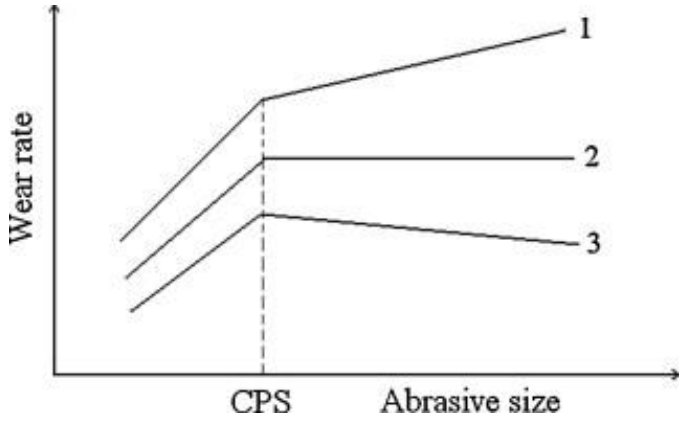


Figure 2.17 Schematic representation showing the typical curves of wear vs. abrasive grain size [79]

The studies on the particle size effect enables the understanding of material removal mechanism for diamond grinding process in relation the abrasive sizes. It can provide a guidance for manufacture of diamond abrasive for different surface finish and material removal requirement, and improve the design of current grinding wheels for optimal wear behavior.

2.2.3 Abrasive shape

The high quality of synthetic diamond crystals can be achieved by controlling the growth conditions (e.g. temperature, pressure, time, nucleation density) in HPHT process. For example, cubic shape at low temperature (growth on {100} or {001} planes), octahedral shape at highest temperatures (growth on {111} planes). Figure 2.18 shows the crystallographic morphologies of synthetic diamond.

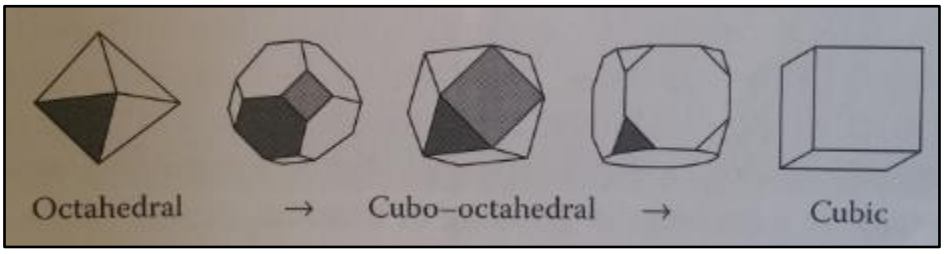


Figure 2.18 Growth morphologies of diamond [1]

It can be seen that, the typical growth of synthetic diamond would fall into the combination of growth on various primary planes, which results in cubo-octahedral shapes rather than pure octahedral or cubic shape. Moreover, commercial abrasive products also includes abrasives which are processed by crushing or ball milling from as-synthesized diamond abrasives. As a result, the shapes of abrasive are not definitive and difficult to fully describe. In theory, there is an infinite number of parameters required to fully define the abrasive shape, however, in practice, only a few of them are useful to evaluate the wear behavior [84].

De Pellegrin et al. [85] carried out an wear experiment to study the trends

and correlations of shape properties of diamond particles including major diameter, minor diameter, minimum diameter, projection area, aspect ratio, convexity and sharpness with material wear rate. A digital-camera-equipped optical microscope was used to capture the electronic boundary projections of a set of sample diamond particles with nominal diameters ranging from 65 to 197 μm.

It was found that sharpness has a 0.99 correlation coefficient with wear rate, while convexity has a 0.98 correlation coefficient with wear rate. Aspect ratio only reaches the correlation coefficient of 0.82. It can be conclude that sharpness and convexity gave the best correlation with wear rate for grinding process. The study on abrasive shape effects allowed the prediction of wear rate based on shape properties and evaluate the grinding performance.

2.3 Diamond grinding tool: design and modelling

This section aims at describing the characteristics of conventional diamond grinding tool (with randomly shaped abrasives) and engineered diamond grinding tool. In particular, novel design of engineered grinding tool and their improvement of grinding performance will be discussed as the main difference between conventional and engineered tool is the design of highly controlled abrasive features. In addition to various experimental work conducted to study grinding performance, the current state of modelling approach will also be covered.

2.3.1 Conventional diamond grinding tool

Diamond grinding process has been established for processing various hard non-ferrous material, which can produce superior surface finish and high material removal rate with relatively long tool life (low wear).

Compared to other grinding wheel with conventional abrasive material such as aluminum oxide or silicon carbide, the demand for diamond grinding wheels becomes higher due to the excellent performance in holding force, abrasion, molding, lifetime together with high accuracy in profile formation and efficiency [86,88].

In order to hold the conventional diamond abrasives during grinding, a bond system is required to retain the grits without the premature pullout from the surface, as well as, offer the sufficient strength to transfer the grinding force and assist the heat dissipation [89]. The bond system can be divided into two types: single-layer type for those holding a single layer of abrasive on a solid hub and multilayer type for those providing several layers of abrasives within the bond material.

For multilayer diamond wheel, three major types of bond are used including resin bonds, vitrified bonds and metal bonds. In the case of multilayer arrangement, the abrasive surface is typically produced by mixing the abrasives and bonding materials (soften or liquid form) in a mold with required profile and then pressing or sintering. Diamond abrasives are either half-buried on the abrasive surface or completely embedded within the bonding material. The advantage of multilayer arrangement is the continuous regeneration of abrasive cutting edges by the exposure of embedded grits during grinding process, and the tool form and girt sharpness can be maintained by regular dressing. Resin bonded diamond grinding tool tends to be more elastic than other wheels, and it is usually selected for diamond abrasives to achieve extremely low roughness. Generally, a new resin bonded diamond grinding tool cannot remove material efficiently until the heat and abrasion remove some of the resin material on top of the surface to expose more embedded cutting edges. Vitrified bond is much harder than resin bond and it can be trued to produce a form for grinding various profiles. Metal bond is the hardest and toughest among the three, providing a firm retention of diamond grits

and high abrasive wear resistance. It is often employed to produce low surface roughness with accurate, predictable removal of stock material. A new ELID (Electrolytic In-Process Dressing) grinding can be used to grind the metallic bond wheel surface to keep its sharpness and form [90].

Unlike multilayer diamond wheel, only metal bond is used for single-layer diamond wheel. The common method of fixing the diamond grits on the tool surface is deposition of metal (e.g. nickel) by electroplating. An alternative method is to chemically bond the diamond grits by brazing. Brazing has a thinner metal coating around the diamond grits which can offer higher grinding efficiency due to the much greater exposure of grits. However, brazed wheel is fabricated under much higher temperature (1000°C) than electroplated grinding tool, resulting in a less controlled profile and possible damage on grits [91]. As the high expense to set grits on single-layer wheel and common dressing process for multi-layer wheel cannot be used, single-layer wheel required to be set with high accuracy, therefore can operate with stability during the operation.

The surface topography of diamond grinding tool manufactured by the bonding process mentioned above tends to have stochastic nature in terms of random grit size, geometry, crystallinegraphic orientation and spacing (Figure 2.19). In addition, the exposure and protrusion of grits are also varying across the wheel surface due to their irregular shapes, orientations and radial locations in the bond [15]. Then number of active grits and their cutting effectiveness during grinding are dependent on factors such as the abrasive concentration and the extent of grits protrusion from the wheel surface. The stochastic arrangement can adversely affect the material removal efficiency and chip flow where diamond grits are clustered. The large numbers of inactive or less effective grits during the grinding are not only increase the manufacturing cost but also interfere with normal operation of active grits causing higher grinding temperature and reduce the tool life [92].

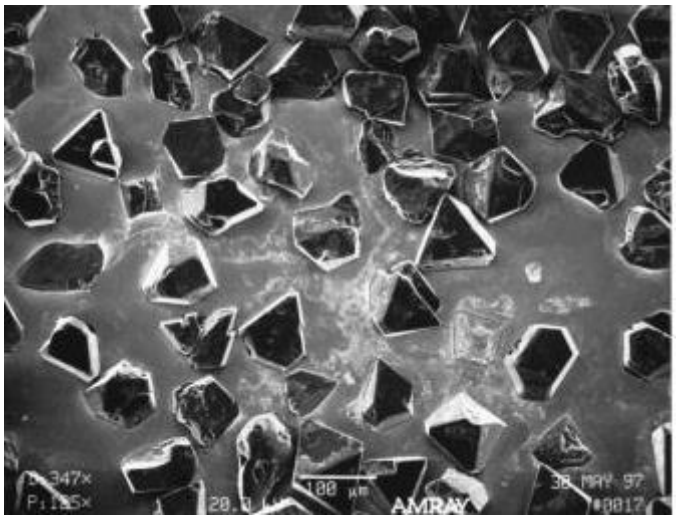


Figure 2.19 Electroplated diamond grinding wheel surface [15]

2.3.2 Engineered diamond grinding tool

The conventional grinding tool topography has been reviewed in section 2.3.1, showing that the abrasive size, geometry, distribution and orientation are random due the nature of manufacture process. As a result, the grinding process becomes less efficient (e.g. inactive grits involved, less controllable ground surface topography) and can introduce surface damage and wheel deterioration (e.g. insufficient heat dissipation, more micofractures and burns, pull-out of grits) [93,94].

Many researches has been done to investigate the texturing/patterning of abrasive grits, in order to reduce the negative influences of the stochastic topography of grinding tool surface. The engineered grinding tool developed based on this concept can be divided as 1) positioning the grits in a pre-defined format 2) texturing the grits as regular shapes and identical orientations. The section will review the developments of these two types of engineered grinding tool and their improvements on performance of grinding process.

2.3.2.1 Engineered grinding tool with defined grain pattern

In this type of engineered grinding tool, abrasive girts are planted on the tool surface by special positioning techniques in a pre-defined arrangement. The ordered arrangement of grits can reduce the number of grits required and increase the uniformity of cutting edge positions, thus makes the process a more predictable one enabling the easier control and optimization of grinding process [95,96].

Burkhard proposed a design of grinding wheel with defined grits arrangement in 2002, where the grits were glued in a pre-defined pattern before brazing. The arrangement is shown in Figure 2.20, the grit density was reduced by 75% by selecting the glue dot center as 0.5mm, while the machining time is reduced by 1/3 without any sacrifice on the workpiece surface finish [97].

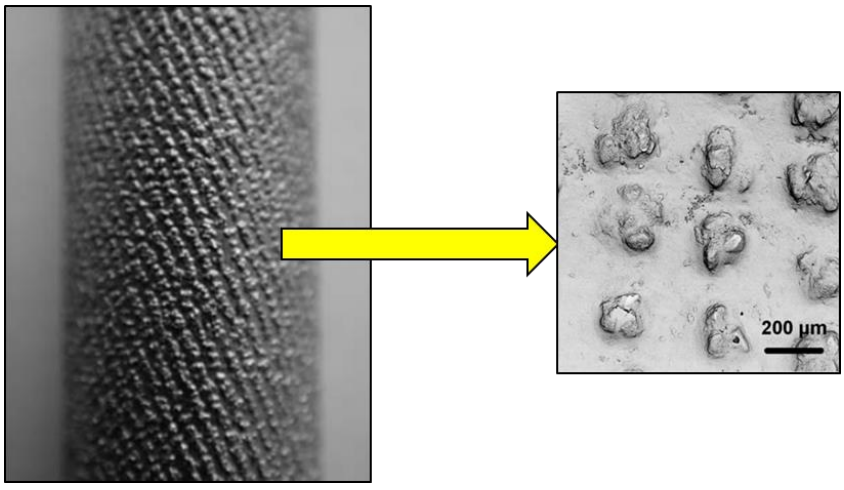


Figure 2.20 Arrangement of CBN grains on the engineered grinding wheel [97]

Another engineered grinding wheel was designed and produced by manually fixing the grits by cement at pre-defined positions followed by electroplating process (Figure 2.21) [98]. However, manual positioning is very time consuming and can significantly increase the tool cost.

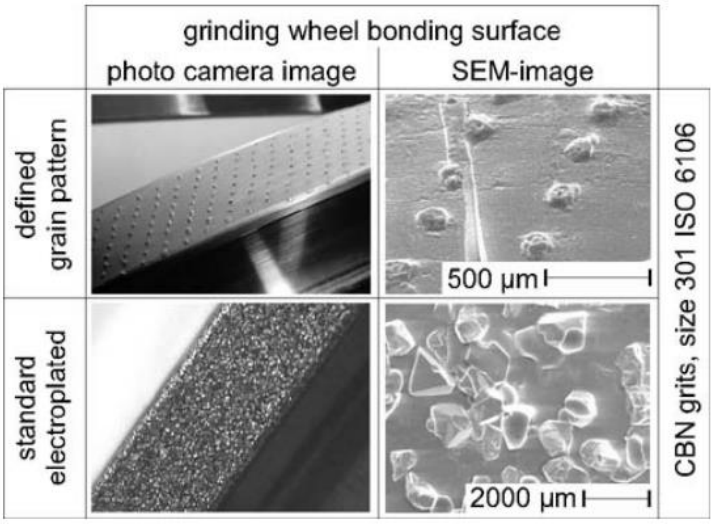


Figure 2.21 Manually positioned engineered grinding wheel and conventional electroplated grinding wheel [98]

In a later study, the positioning was improved by using masking technologies for preliminary adhesion of the grains on the wheel hub, and then completed by electroplating process. Although it has significantly reduced the tool cost compared to the manually positioned wheel, the cost is still considerable higher than the conventional wheels [99,100].

Further studies has been carried out based on the Burkhard's design of semi-automatic system for positioning grain pattern. The precision of the grain pattern was evaluated as a circular region (with diameter D_{edge}, Figure 2.22) around the nominal position of the grain's edge. Three different grain patterns were produced to be compared with conventional electroplated wheels (Figure 2.22). It was found that for pattern A and B with Δz_2 (parallel distance between adjacent grains) equals to 3.2 µm and 1.6 µm respectively can provide superior finishing performance, while pattern C with Δz_2 equals to 0.8 µm exhibited a poor control of positioning [101].

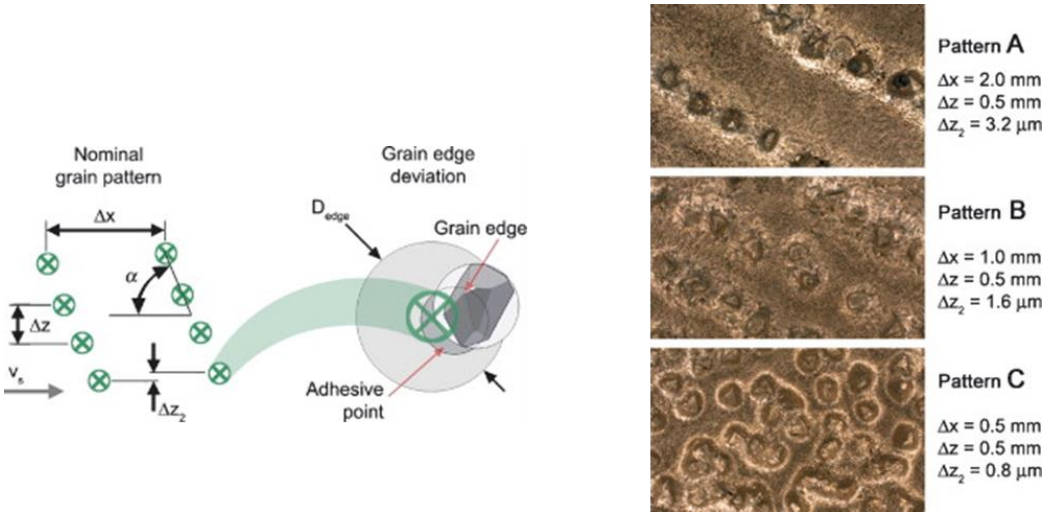


Figure 2.22 Parameters of grain patterns [102]

A LIGA-like technology was also utilized to fabricate engineered grinding pad consisting of micro-diamond abrasive pellets for grinding silicon wafers. There are two different shape of abrasive pellets were produced: hexagonal and cylindrical (Figure 2.23). The surface roughness of R_a = 0.05 µm was achieved on the silicon wafer, moreover, the engineered construction also shows higher grinding efficiency and good chip removal [11].

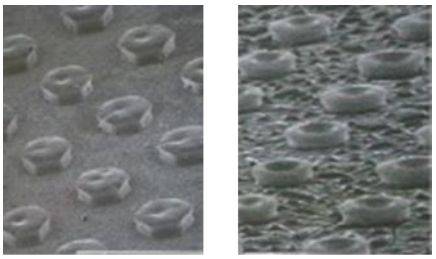


Figure 2.23 LIGA –like technology produced abrasive pellets a) hexagonal b) cylindrical [11]

Recently, more developments of engineered grinding pad was made by using LIGA-like technology. Some novel designs of abrasive grits arrangement based on the biological structures (e.g. sunflower). The evaluation tests showed improvement of surface roughness (at least 10%) indicating their good surface finishing performance [103-105].

As the advances in design of engineered grind tool with ordered grain

patterns, various improvements of grinding performance has been achieved [106]. Lower grinding temperature and reduced grinding force are two direct improvements due to reduced number of abrasive grits and controlled distribution pattern. The experiment conducted by engineered grinding wheel on 42CrMo4 (65 HRC) indicates that the maximum normal and tangential grinding force was reduced by 60% and 80% compared to that of conventional wheels [98]. In another test for grinding heat-treated steel AISI 4140H of 60 ± 2 HRC, the normal and tangential force reduction of 30–40% and 20–35% were achieved. At the depth of cut of 2mm, the grinding temperature was lowered by 230°C [99]. It was also found a trend that the ratio between normal and tangential grinding force for engineered grinding wheel is larger than that of conventional wheel [95]. This suggested that the interaction between workpiece surface and conventional wheel surface is more aggressive than that of engineered wheel, indicating that conventional wheel undergoes more severe friction conditions.

Although some of the studies have proved engineered grinding tool can produce better surface roughness due their superior chip flow, cooling performance and better load distribution [105, 107], conventional wheels with higher grit density tend to produce smaller unreformed chip thickness leading to better surface roughness, which is also proved by some other experiments [95,98,108]. As a result, further researches are needed to specify the critical design parameters for engineered grinding wheel with defined grain pattern, in order to optimize its surface finishing performance.

2.3.2.2 Engineered grinding tool with defined grain geometry

The engineered grinding tools reviewed in the previous section are

produced with defined grain pattern by brazing, electroplating and LIGA-like technology, which position the abrasive grits in a defined pattern on the wheel hub or backing plate. Unlike these types of engineered tools, novel concept of grinding tools with defined geometry of micro abrasive elements were produced on the solid monocrystalline thick-film CVD diamond by using Nd:YAG Q-switched pulsed laser in 2009 [13]. The laser ablation technique has provided an effective approach in the rapid generation of highly uniform abrasive surface with micro cutting elements having identical size, shape, protrusion and spacing. Technically, any shape and arrangement of micorfeatures can be produced as the high flexibility of laser ablation techniques. Three types of micro-arrays were produced to demonstrate the capability of laser ablation for engineered grinding tools (Figure 2.24).

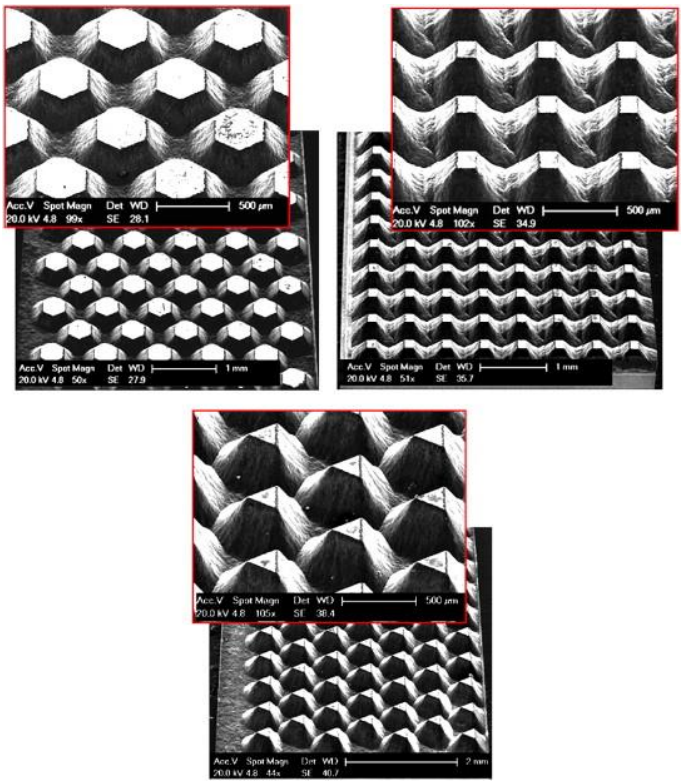


Figure 2.24 Micro-arrays produced by laser ablation on CVD diamond [13]

It was reported that a more advanced design of engineered grinding tools with micro cutting arrays was proposed and evaluated by grinding on the

Ti–6Al–4V [10]. The abrasive micro-array was produced with cutting elements having (1 0 0) crystallographic orientation on the flank face and (1 1 0) orientation on the rake face. Each micro cutting element was produced with a cutting edge width of 100μm with a supporting flank of 50μm to provide additional strength (Figure 2.25). In addition, the primary/secondary rake angles γ=−32°/+1° and clearance angle α=4.5° was generated for each of the micro cutting element in order to enhance their cutting performance. This technique was also introduced to produce engineered grinding pad with square frustum and saw tooth abrasive grits on the polycrystalline CVD diamond film [109].

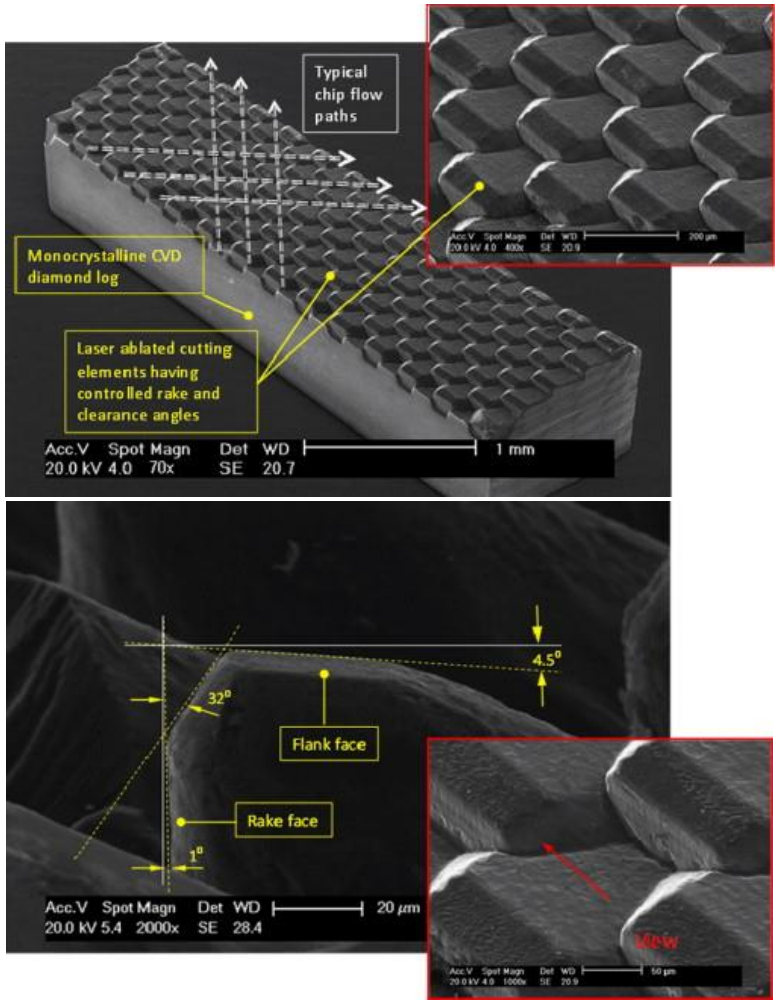


Figure 2.25 Laser ablated micro-arrays with controlled cutting elements geometry [10]

In addition to generate micro cutting elements on flat diamond film, it was also successfully produced on the curved surface for rotary micro-

grinding tool by laser ablation technique. Figure 2.26 illustrates the rotary grinding tool surface featuring staggered array of uniformly shaped symmetrical cutting elements around the periphery of the diamond structure, and the regular pattern of the cutting element was clearly visible, providing unrestricted chip flow paths between adjacent elements [110].

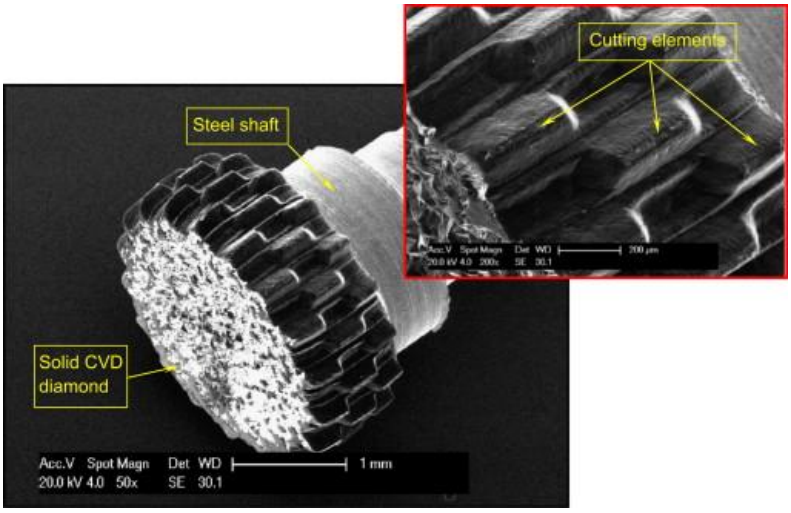


Figure 2.26 Laser ablated solid diamond rotary micro-grinding tool [110]

Another technology called microreplication can be used to generate grits with defined geometry on the abrasive pad surface [123]. This patented technology for the deposition of abrasives particles can provide a controlled size, distribution and orientation of coated abrasive particles.

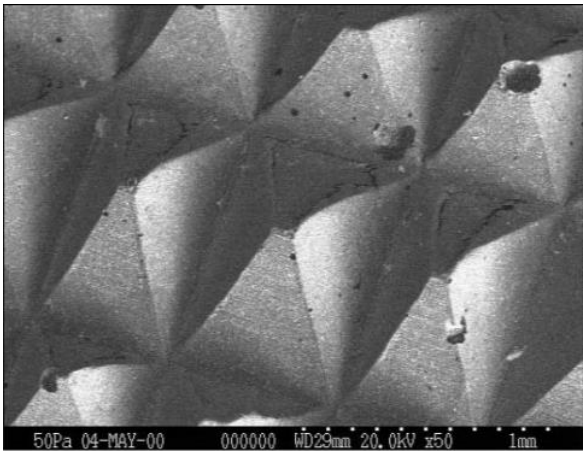


Figure 2.27 Pyramid-shaped engineered abrasives generated by microreplication [123]

Figure 2.27 illustrates the abrasive pad surface with defined grits deposited by microreplication. In this case, the abrasive surface consists of pyramidal structures containing micron-graded minerals that are uniformly applied to a backing material

Similar to the improvements reviewed in section 2.3.2.1, one of the most obvious improvements can be found is reduction in grinding force for engineered grind tool with PLA micro-arrays. It was reported that the grinding force of diamond micro-array is generally lower than that of conventional diamond electroplated grinding tool (Figure 2.28) [10]. In addition, the grinding force variation during the process is more consistent for diamond micro-array thanks to the highly uniformly shaped and distributed cutting elements which remained intact for the duration of the test. It also showed that tangential grinding force of micro-array is much lower that of conventional electroplated wheel, indicating the friction condition for micro-array is less severe.

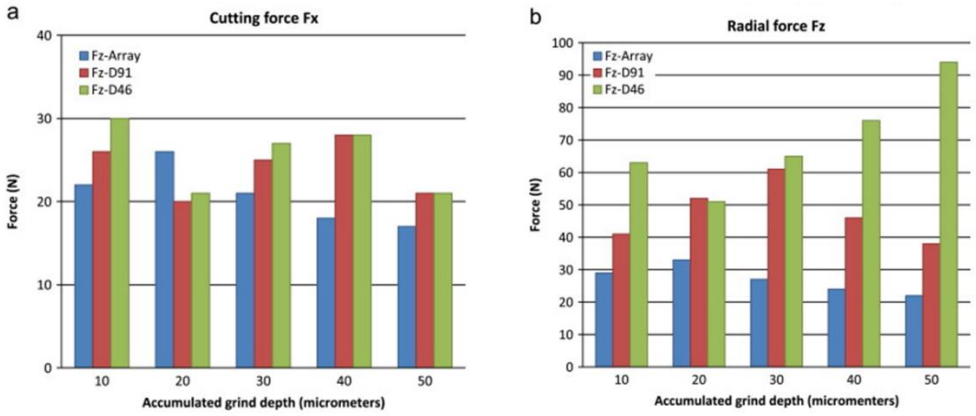


Figure 2.28 (a) Normal and (b) tangential forces produced by diamond micro-arrays and electroplated elements [10]

Significant improvement on workpiece surface quality has been reported by comparing between PLA engineered grinding tool and conventional grinding tool. For the comparison between diamond micro-arrays on flat surface and grinding wheel with D91 grits (comparative size to the array cutting elements), surface roughness was improved by greater than 3.5 times, while surface waviness was improved by 21.5 times. Even when

comparing with D46 grits (half equivalent-size to the array cutting elements, there are still 1.6 and 3.3 times improvements for surface roughness and surface waviness respectively [10]. Similar results was also reported for rotary micro-grinding tool, 3 times improvement on best surface roughness and 7 times improvement on surface waviness [110].

The PLA micro cutting elements remain intact after grinding operation, no obvious sign of mico-fracuture can be observed. In addition, the tool surface showed minimal material clogging and the debris are distributed over the tool surface, indicating clear chip flow paths help the migration of material debris. All the cutting elements remain active resulting in a longer tool time [10]. The improvements of tool wear characteristics and superior chip flow was also proved by PLA rotary micro-grinding tool [10]. These encouraging findings of engineered grinding wheel have enhanced the understanding of influence of grinding wheel topography on grinding performance, and brought more new concepts for development of innovative grinding tool. Although engineered grinding tools have great potential to achieve highly controlled surface finish and forms, the design parameters are still needs to be extensively studied to optimize its performance. Moreover, the relatively high cost on positioning and texturing also needs to be addressed before massive industrial applications.

2.3.3 Development of grinding modelling techniques

It has been discussed in section 2.3.1, conventional grinding wheel has abrasive grits distributed randomly on the tool surface with different shapes, sizes and protrusions. As a result, each cutting edge will act individually in grinding process to remove the material and produce final workpiece surface topography. Taking the stochastic nature of abrasive surface topography and various working parameters involved into

consideration, optimize the design and working conditions solely by experiments is quite difficult, thus modelling approach is important to help understand and predict grinding process.

The shape and distribution of abrasive grits can significantly influence the surface finish and force. Tönshoff characterize the kinematics of the grinding process by a series of statistically irregular and separate engagements [111]. Topography models are used to describe the grinding wheel structure by considering the quantities of motion and geometric parameters, while chip thickness models are used to describe chip formation. Another research described the grinding process as a sum of interactions between abrasive grains and workpiece material [112]. In order to simulate the surface roughness, grinding wheel topography needs to be specified first.

In general, empirical (i.e. model coefficients are fit to experimental data) and mechanistic (i.e. based more on physical grinding processes) methods are two main types of methods used to develop wheel topography models [113]. For the empirical models, simplifications based on experimentally measured data, such as average distance between grits and average grit protrusion, are employed to describe the wheel topography. For example, an empirical grinding wheel topography model was developed having the identical grit protrusions and autocorrelation functions [17]. Empirical models have the advantage of relatively easy to be generated, however, they are lack of accuracy and require excessive experiments for each specific application. The analytical model can be divided into two groups: statistical and kinematic. Statistical part is to study the distribution function of the grit protrusion heights, while kinematic part is to study the kinematic interaction between grains and workpiece. Hecker et al. predicted surface roughness based on a probabilistic undeformed chip thickness model, where surface roughness was expressed as a function of wheel microstructure, the process kinematic conditions and the material

properties [114]. After that, several models based on probability distribution of chip thickness were developed to predict surface roughness [115-117]. A typical research work for kinematic model took the random distribution of grit protrusion height into consideration, and develop a numerical solution for that [118]. In the subsequent work, Yueming et al. established a kinematic model to predict the workpiece surface roughness by using three types of grain shapes (i.e. sphere, truncated cone and cone) [119].

The extensive research work conducted on the modelling of grinding process have provided various solutions to address the stochastic nature of wheel surface topography. However, the distribution and grain shapes can be controlled for engineered grinding tool, little researches has been reported to establish surface roughness model for such kind of engineered grinding tool. Moreover, the current models are mainly focused on linear grinding process, very little researches have been reported on grinding with planetary movements (i.e. plane grinding).

2.4 Summary and research gaps

An extensive literature review has been carried out covering the structure, properties and characteristics of nature of synthetic diamond material. The superior mechanical and chemical properties allows diamond to be employed in various industrial applications, in particular, abrasive machining processing (e.g. grinding/polishing) due to its high hardness value among the typical abrasive materials. HTHP and CVD synthesis methods provide the opportunity to control the growth of diamond to enable the production of diamond with more customized properties, less impurities and higher consistency in crystalline structures. Therefore, as the development of synthetic diamond production, their versatility in structure and properties will provide wider scientific and engineering

applications.

For the conventional diamond grinding tool, it has been found that the abrasive surface having a stochastic nature. The diamond grits are random in size, shape, orientation and distribution, moreover, the protrusion heights are also varying from one grit to another. These stochastic characteristics are caused by manufacturing process for conventional grinding tools, which can negatively affect the chip flow and grinding temperature, resulting in less cutting efficiency and introduction of more damage. Many researches has been carried out to provide solutions in term of engineered grinding tool with controlled tool surface. By positioning the abrasive grits in a pre-defined arrangement has successfully reduced the grinding force and temperature with longer tool life. Further improvements has been made by producing micro cutting elements with controlled features on the monocrystalline and polycrystalline CVD diamond, in particular, utilizing a novel laser ablation technique. High accuracy of micro cutting elements was achieved. These PLA engineered grinding tool showed a significant improvement in grinding force and temperature, in addition workpiece surface finish was also improved a lot compared with conventional electroplated grinding tool. However, the reported researches for engineered grinding tool are mainly focused the grinding operation with linear kinematics, there is a lack of knowledge on the engineered grinding tool with planetary kinematics (i.e. plane grinding).

In the case of conventional grinding tool, in order to predict the workpiece surface roughness, grinding process has been extensively studied by modelling approach. Two main methods (i.e. empirical and analytical) were developed to provide solutions to express the stochastic grinding tool surface topography. Most of the related work are conducting for conventional grinding tool, less information is available for engineered grinding tool, especially the one with planetary kinematics (i.e. plane

grinding).

Research challenge 1 (Refers to objective 1 and 3 in section 1.3)

While many researches have been conducted to generate engineered abrasive tool with controlled features, and various preliminary evaluations have shown the advantages of engineered abrasive tool over conventional abrasive tool with stochastic nature, it seems there have not been many studies to examine the influence of specific design parameters of engineered abrasive tool (e.g. grit geometry, total planar contact area) on the performance of grinding, especially lacking of study for the process with planetary movements (i.e. load controlled plane grinding). Considering the possible optimization requirement for future industrial applications, an important research challenge is to understand the influence of design parameters of these novel abrasive tools on the machined surface quality to enable the generation of desired workpiece surface.

Research challenge 2 (Refers to objective 2 in section 1.3)

Although previous researches have been focusing on modelling the grinding process employing conventional grinding tool, there is still a lack in study of engineered abrasive tool by modelling approach, especially under the abrasive processing with planetary movement (i.e. load controlled plane grinding) due to its complex kinematics. There is also a need to take the slippage between workpiece and abrasives into consideration when simulating the process with planetary movements (experimentally).

Research challenge 3 (Refers to objective 4 in section 1.3)

In spite of all the reported literature in the comparison between conventional grinding tool and engineered grinding tool, there is no

quantitatively evaluation has been done between grit working population and visible abrasives on the tool surface, no studies has been done to determine the engaging planar contact area of conventional grinding pad and adjust the design of engineered abrasive pad based this to improve the material removal performance.

Chapter 3

Methodology

This chapter is the key chapter to understand the methods, instrumentations and algorithms. In this chapter, it will introduce the material been used and the experimental procedures and research approaches been utilized to conduct the research and achieve the objectives.

3.1 Methodology background

Based on the research work demonstrated in section 2.3.2.2, it can be found that previous researches have been conducted to generate abrasives with regular geometry and spacing [13,110]. In this research work, the already established PLA technique has been applied to develop the engineered abrasive pad. According to Chapter 1 and Chapter 2, there is a lack in understanding the wear progression and material removal mechanism for engineered abrasive pad under the condition of abrasive machining with planetary movement (e.g. plane grinding). Moreover, no researches have reported to develop a geometrical model for predicting workpiece surface roughness for engineered abrasive tool under planetary grinding process. The steps of research works are summarized below in Figure 3.1.

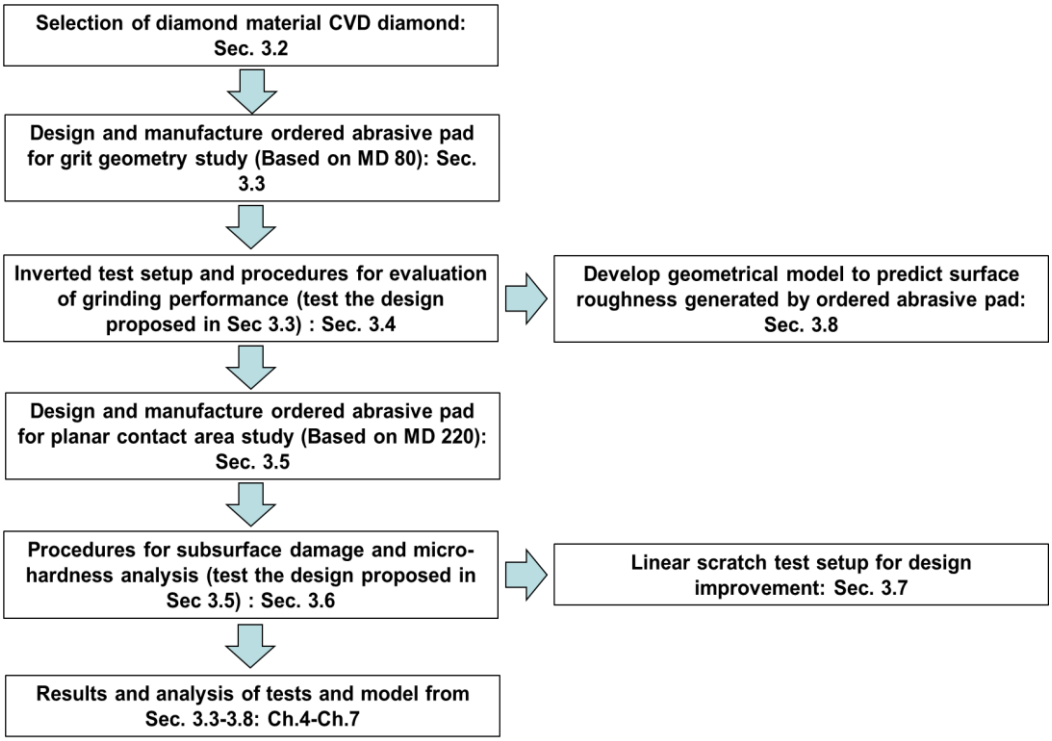


Figure 3.1 Flow chart of methodology for the research programme

3.2 Selection of material for the generation of abrasive arrays and workpiece material for grinding test

Polycrystalline chemical vapour deposition (CVD) synthetic diamond has been selected for generation of ordered abrasive pad to achieve the objectives of this research. The polycrystalline CVD diamond thick films (0.5 mm) used in the experiments are directly synthetized on a WC substrate (10 mm x 10 mm x 1 mm). The literature review in Chapter 2 has covered that diamond and cubic boron nitride (CBN) are two main types of superabraisves used in grinding industry, as the hardness of diamond is superior (Figure 3.2) to CBN both at room temperature and high temperature (typical in high-speed operation), diamond is chosen as the material to generate abrasive pad.

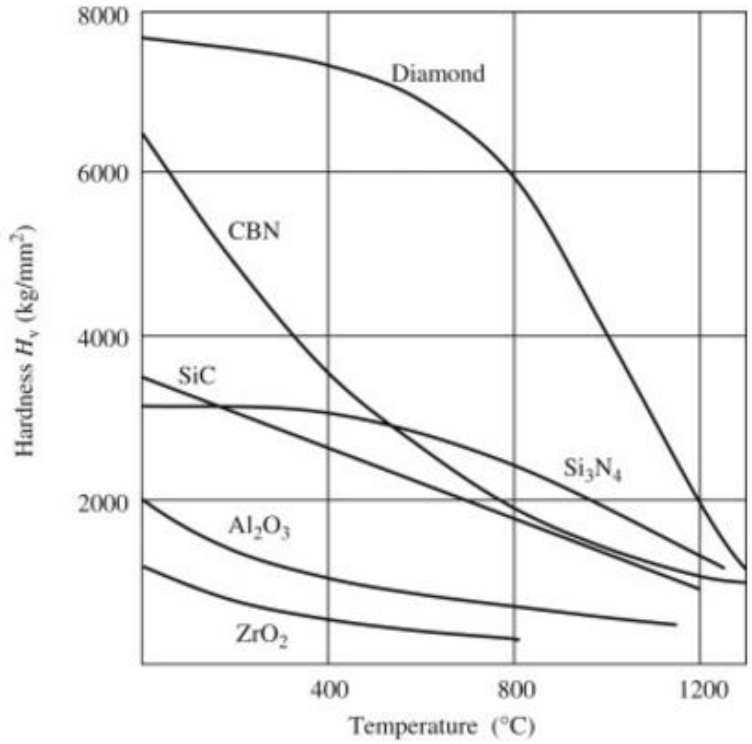


Figure 3.2 Variation of hardness for different types of abrasive material [24]

In the majority of applications, monocrystalline diamond tools give good results in terms of cutting performance and relatively low cost. However, for certain applications, in particular grinding/polishing hard or sintered material, polycrystalline diamond has proved to achieve better performance in terms of higher removal rate and outstanding surface finish than that of monocrystalline diamond [120]. This is due the differences in their structure, the distinct cleavage planes of monocrystalline diamond may cause facture when operating under stress. Compared to monocrystalline diamond, polycrystalline diamond has numerous particles whose sizes are less than 0.01 μm bonded together in a random structure. This structure prevents major fracture of diamond from occurring when under high stress, the fracture are limited in a small group of crystallites on the perimeter, and only some microfracture may occur. In addition to this, other advantages of polycrystalline are listed below [120]:

- Polycrystalline diamond tools can cut material very fast due to its ultra rough nature and more cutting edges compared to monocrystalline diamond
- Polycrystalline diamond produce less random scratches and subsurface damage which gives a smoother finish compared to monocrystalline diamond
- Polycrystalline structure tends to produce more cutting edges due to microfracture during operation which can maintain its cutting performance throughout the machining process

304 stainless steel disc (diameter 200mm) is selected as the workpiece material for grinding test. Stainless steels are commonly regarded as difficult to machine material by diamond tools due to the diffusion wear caused by the chemical affinity of the diamond with carbon in the steel being machined, which can cause reduced tool life and inferior surface finish. As a result, 304 stainless steel is a good option to demonstrate the capability of novel engineered diamond abrasive pad on grinding widely used ferrous material.

3.3 Design and manufacture ordered abrasive pads

As discussed in section 1.3, in order to fully exploit the advantages of the grinding pad with controlled features, it is important to understand how the workpiece surface roughness and wear responds to different grit geometries, which needs to compare the performance of engineered tool with conventional tool. In order to achieve this, the dimensional characteristics of engineered abrasive grains are supposed to be comparable to conventional tools. In this research, Stuers MD-Piano plane grinding pad is chosen as the benchmark conventional tool, as this series of products are used for surface preparation under planetary movements,

and the abrasive grits are resin bonded, which is a good example of conventional abrasive pad with stochastic nature. Figure 3.3 shows the MD-Piano 80 grinding pad, the nickel coated abrasives are mixed with resin bonding in the abrasive element (pellet), and the abrasive element is attached to the metal backing. Based on the small hexagonal abrasive pellet on the MD-Piano pad, the design concept of engineered abrasive pad is proposed in Figure 3.4. The abrasive grits are distributed regularly on the hexagonal pellet, and the girt geometries are identical.

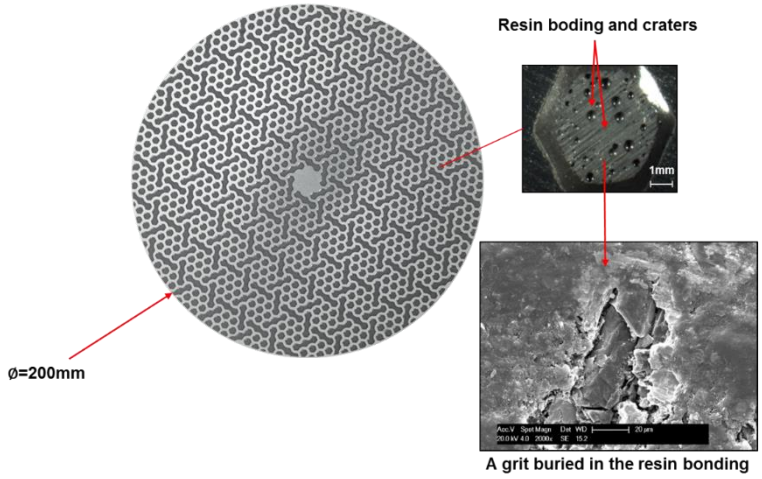


Figure 3.3 MD-Piano 80 grinding pad and enlarged abrasive element with SEM image of one grit buried in the bonding material

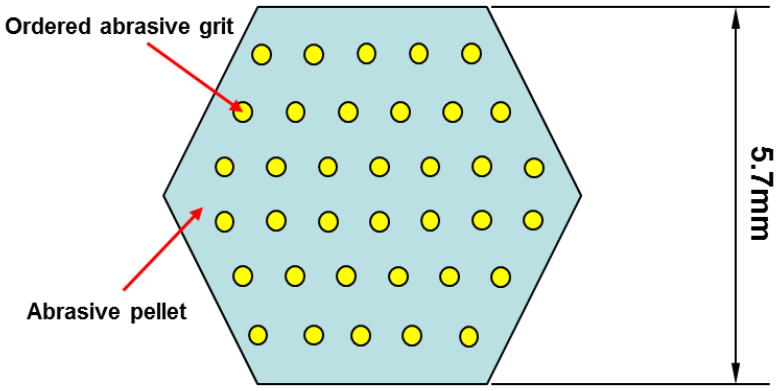
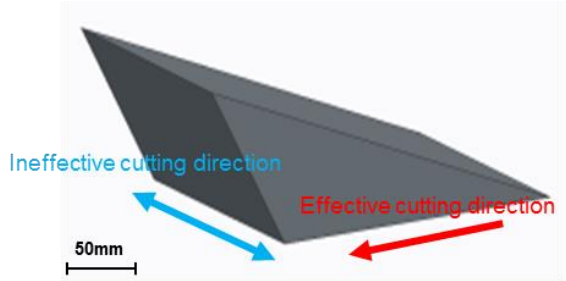
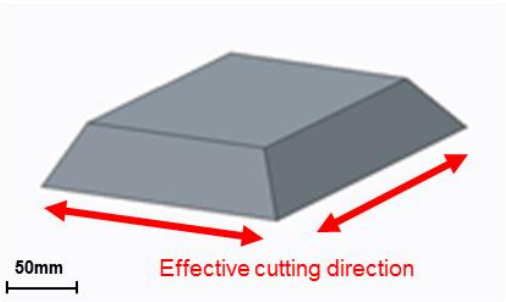


Figure 3.4 Schematic illustration of Concept image of engineered abrasive pad with ordered abrasive grits based on MD Piano pad

The dimensional characteristics of the grit sizes were chosen to be approximate as the abrasive tools situation of the MD-Piano 80 (i.e. grit size of FEPA D252, appx. 200mm). Into these hexagonal features two types of abrasive grits (Figure 3.5) which either have symmetric cutting edges (e.g. square frustum) or asymmetric cutting edges (e.g. saw tooth), which enables the evaluation of the effect of abrasive grits geometry (cutting edges arrangement) on the finishing performance. The selection of grit geometry is not based on the possible geometry, theoretically of infinite variation which can be generated, but on the utilization of cutting edges when operated in rotary motions. For example, when employing the square frustum grits, the cutting edges are axially symmetrical relating to its own axis, which means it can provide relatively uniform cutting edge in cutting direction when driven by planetary movements. It is the different case for a saw tooth grit, as it can only provide effective cutting in one direction under the condition of linear tool path (Figure 3.5).



Saw tooth abrasive grit



Square frustum abrasive grit

Figure 3.5 Examples of saw tooth and square frustum abrasive grit and their effective cutting directions under planetary movements

Previous researches have demonstrated that Pulsed laser ablation (PLA) technique can be used to shape CVD diamond material into cutting tool [10]. The laser processing is enabled by a hybrid laser machining centre equipped with a Nd: YAGQ-switched pulsed laser (wavelength 1064 nm; 100 W max. Output power; 50 kHz max. pulse frequency; focal point size 40 μm) which mounted on a linear stage to allow the three axis motion under pre-optimised process/beam path parameters [10]. The laser beam parameters employed were, 20% of max output powver, 25 kHz Frequency, and transverse speed of 100mm/s. The adopted beam path strategy is cross hatch scan, which is shown in Figure 3.6. The cross-hatch beam paths ablate the material around defined profiles in horizontal and vertical directions and initiate the protrusion of the features, the size and overall protrusion of the abrasive is determined by the numbers paths move across the material.

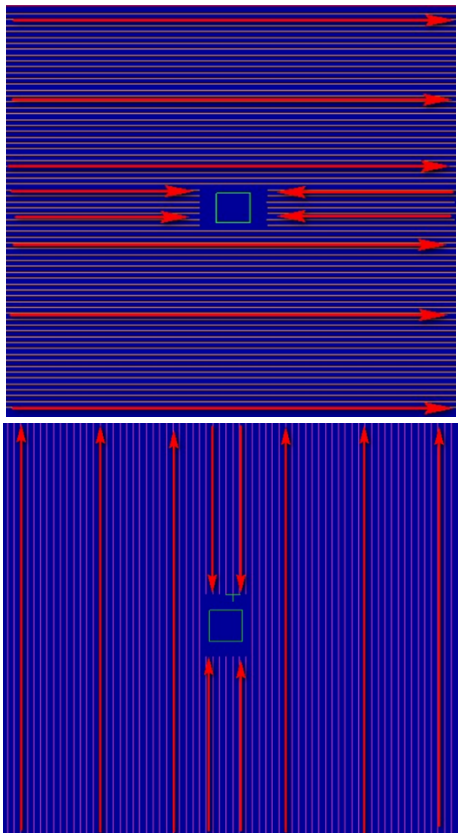


Figure 3.6 Schematic illustration of cross-hatch beam paths for generating engineered abrasive grits

As discussed previously, the engineered abrasive pad will emulate the dimensional characteristics of MD-Piano 80 plane grinding pad. Therefore, the ordered abrasives are generated on the small hexagonal pellet as the MD-Piano 80 pad. An example design of one pellet with the square frustum grits is shown in Figure 3.7. The minor dimensional errors introduced in manufacturing process are ignored.

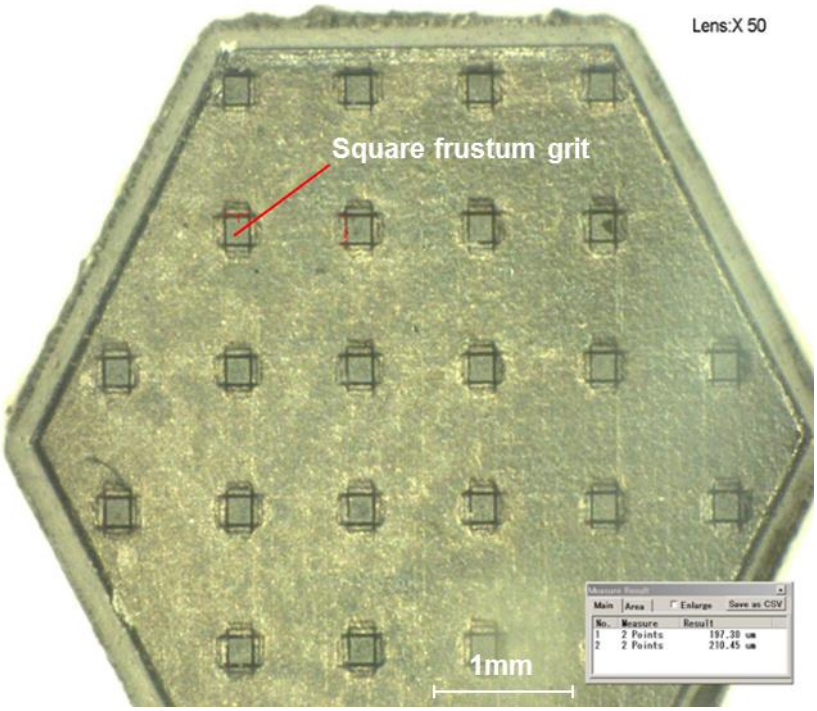


Figure 3.7 Optical micrograph of one ordered abrasive pellet with square frustum grits

3.4 Procedures for the evaluation of plane grinding performance

The key parameters needs to be analyzed for evaluation of the grinding performance including abrasive tool wear mechanism, workpiece surface topography, material removal rate and mechanism. As shown in section 1.3, these key parameters will be analyzed and compared between

conventional tool and engineered abrasive tool under load controlled plane grinding process.

A benchmark procedure is set to allow the evaluation of these parameters for both conventional and engineered abrasive grits:

- Characterization of tool geometry and examine their wear mechanism. Identification of the influence of wear mechanism on the workpiece material.
- Identification of the workpiece surface topography progression and material removal rate.
- Evaluation of the material removal mechanism.

3.4.1 Inverted test setup

The grinding system used to conduct the test is Struers LabPol-5 (Fig. 3.8). Generally, the grinding pad is mounted on the grinding platen (diameter of 200mm) while workpieces are mounted in the mover plate (diameter of 100mm), and the eccentricity between platen center to mover plate center is 50mm. However, in this research, the position of workpiece and grinding pad is reversed to facilitate an accelerated wear test setup. The inverted test setup can minimize the number of hexagonal grinding elements to be generated, which is more time and cost efficient for a laboratory investigation. The micro arrays are generated on the hexagonal diamond pellets, and seven pellets are mounted on a ø30 mm cylindrical dummy (Figure 3.9) to perform the grinding test on 304 stainless steel disc (diameter 200mm). The MD-Piano 80 pad was also cut to the same arrangements as PLA micro arrays and mounted on the cylindrical resin dummy.

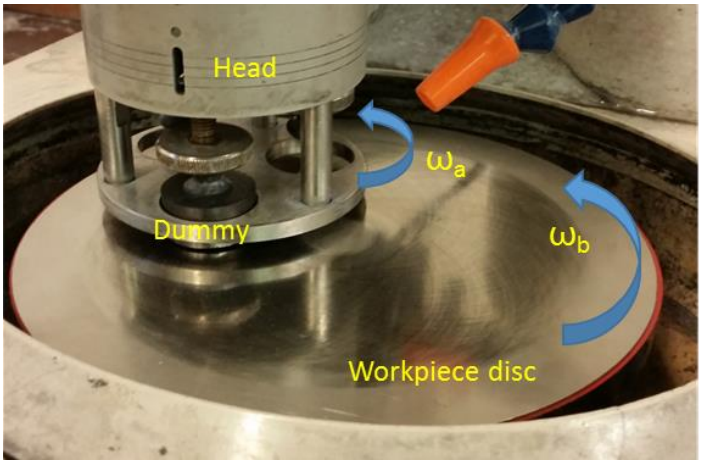


Figure 3.8 Setup of inverted grinding test

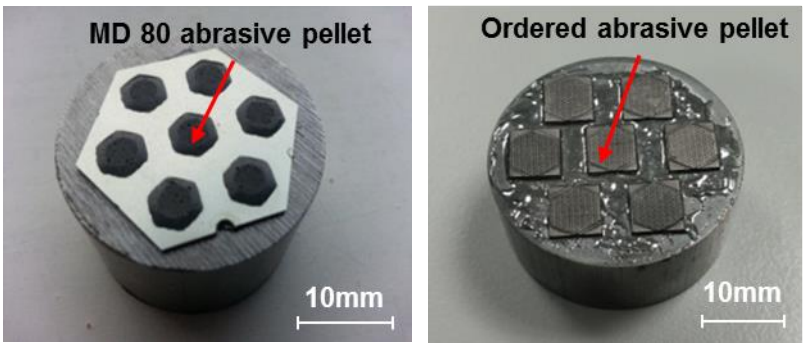
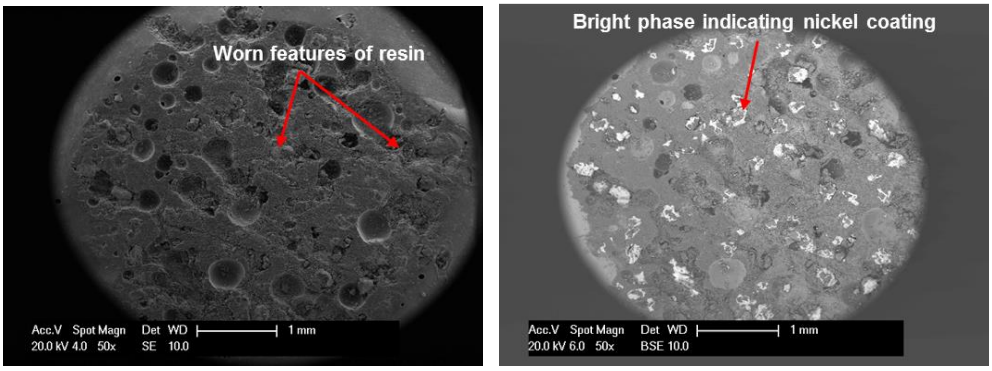


Figure 3.9 Seven abrasvie pellets cut from MD-Piano 80 glued on the resin dummy (left) and seven PLA micro arrays glued on the resin dummy

The 2:1 relationship for rotation speed between head (150rpm) and disc (300rpm) was found to give the best distribution of wear on the grinding surface. This speed combination is reduced by 1/3 (200rpm/100rpm), as high speed may cause stability problem under the setup when only one specimen is mounted in the mover plate. Cutting force was chosen based on the standard grinding pressure of approximate 40kPa between the workpiece and the cutting elements, which is 20N for 30mm diameter specimen. The test time is split into 4 intervals, and each of them is 5min. Measurements and evaluations will be done for these test intervals, the procedures are described in the following sections, and only one set of data was captured for each design parameter due to the limitations on the resources (provided by Element Six and processed by EWAG).

3.4.2 Procedure for the characterization of abrasive tool

In this research, it is important to characterize the geometry and distribution of conventional and engineered abrasive grits. The geometry and distribution of grits can affect their wear progression during the operation, and then influence the scratches across the workpiece material. This will result in different surface topography and material removal mechanism. The characterization is done by Scanning Electron Microscope, SEM (Philips XL30). As shown in Figure 3.10, an overview image was taken for the conventional pad, this allows the understanding of the morphology of conventional pad and the how the grits distributed across the pad surface. Back Scatter Electron (BSE) image was also taken, as the grits are mixed with resin bonding, BSE can differentiate between the bonding and grits (nickel coating) in terms of different phase color.

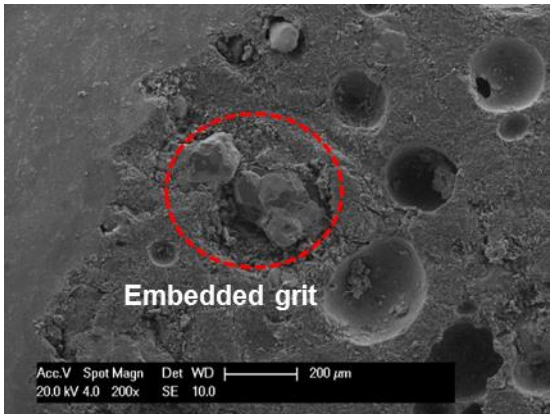


(a) (b)

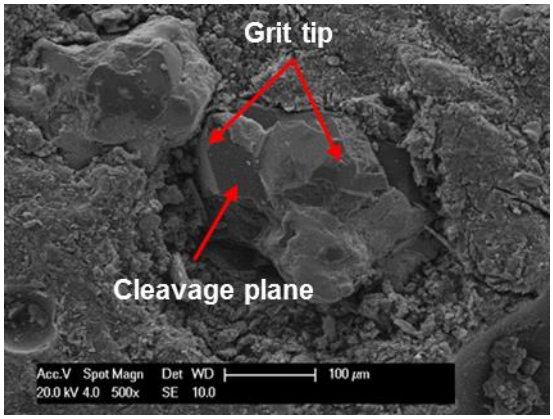
Figure 3.10 Example (a) SEM image of MD 80 abrasive pad surface after inverted grinding test; (b) BSE image of MD 80 abrasive pad surface after inverted grinding test

Higher magnification images were also taken to further characterize single grits, some typical grits (Figure 3.1.1) was selected to examine the geometry and therefore their influence on the finishing performance. Features like cutting edges and cleavage are of concern during the characterization, these information can tell how the grits remove the material and how the wear progression may occur. For the engineered

abrasive pad, same characterization procedure was adopted to analyses the abrasive features (Figure 3.12).

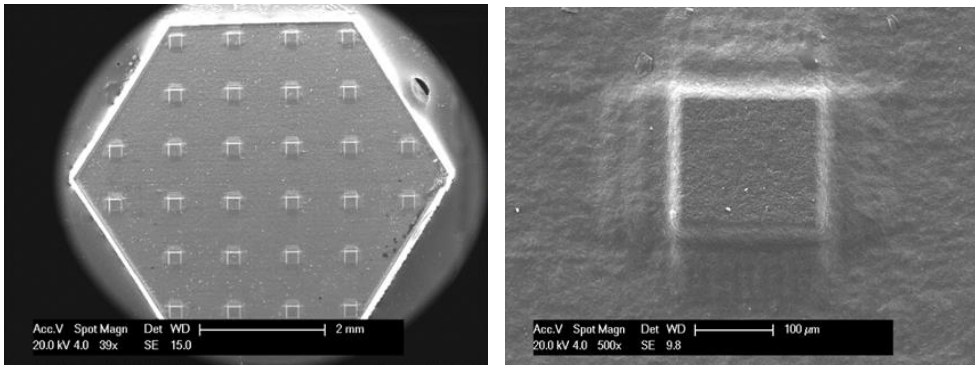


(a)



(b)

Figure 3.11 Example SEM images of (a) Embedded abrasive grit on the MD 80 abrasive pad surface (b) details of abrasive grit features

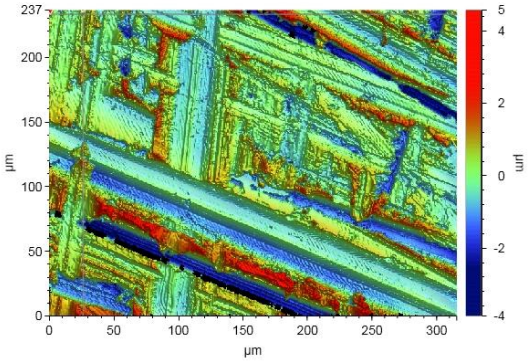


(a) (b)

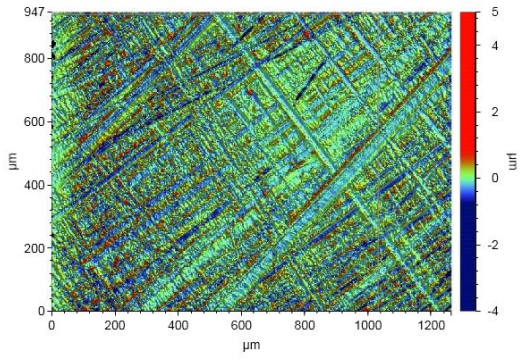
Figure 3.12 Example SEM image of (a) engineered abrasive pellet with square frustum grits (b) single square frustum grit

3.4.3 Identification of the workpiece surface topography and material removal rate

The surface topography of workpiece material was captured by white light interferometry (Brucker Contour GT 3-D). After each test interval, the workpiece disc was sent to Brucker for surface characterization, this topographical measurement enabled the analysis of surface topography of workpiece including the evaluation of surface roughness. The profile and distributions of scratches were examined based on the surface topography (Figure 3.13), which allows the evaluation of generated surface texture. Surface roughness values are also studied to validate the finishing performance reflected by surface texture.



(a)



(b)

Figure 3.13 Examples of workpiece surface topography: generated by (a) conventional abrasive pad (MD 80) (b) engineered abrasive pad with square frustum grits after 5min of grinding

In order to evaluate the efficiency of material removal for abrasive pad, material removal rate was measured between each test interval. The mass difference was weighed by analytical balance and then divided by the time interval to reflect the material removal rate. By analyzing the material removal rate, the correlation between tool properties (e.g. geometry, wear mechanism) and material removal efficiency can be built, enabling the understanding of how conventional and engineered abrasive pad affect the material removal of workpiece material.

3.4.4 Evaluation of the material removal mechanism

Material removal mechanism is important when study the machined surface topography. The removal mechanism can demonstrate how the wear occurs on the surface during machining which enables the understanding of different efficiency of material removal (e.g. cutting mechanism is more efficient than ploughing mechanism in terms of removing material). SEM images with different magnifications were taken to study the removal mechanism by identifying certain removal mechanism across the workpiece surface. Referring to literature on material removal mechanism in Chapter 2, the influence of removal mechanism on removal efficiency and surface texture were then analyzed.

3.5 Design and manufacture engineered abrasive pad for study of planar contact area

In addition to the grit geometry, planar contact area was also evaluated to study its influence on grinding performance. One conventional abrasive pad and two engineered abrasive pad (square frustum grit) with different planar contact area was used to conduct the test. Unlike the study for grit

geometry, the conventional abrasive pad employed for planar contact area study is MD-Piano 220 pad (FEPA D68), which has smaller grit size compared to MD-Piano 80 pad (FEPA D252), as MD-Piano 220 pad tends to remain the planar contact area (number of exposed grits) during the operation. Although all MD series pads are multilayered pad, MD-Piano 80 is more like monolyaered pad due to its largest grit size among the series, which is lacking of continuous regeneration of grits compared to MD-Piano 220 pad. This section will briefly introduce the design specifications of the new engineered abrasive pad as an emulation of MD-Piano 220.

Table 3.1 shows the specifications of two engineered abrasive pads. Instead of generating grits on seven small hexagonal pellets, all the grits were generated on a single big hexagonal pad in order to reduce the processing time and effort of positioning individual pellet on the dummy, dimensions can be seen in Figure 3.14. Same pulsed laser ablation system and beam parameters described in section 3.3 were used to manufacture these two pads.

Table 3.1 Specifications of two new engineered abrasive pad

	No of grits (on one big hexagon)	Grit size (side length)	Single grit surface area	Total planar contact area
		μm	mm^2	mm^2
Pad 1	840	50	0.0025	2.1
Pad 2	840	40	0.0016	1.344

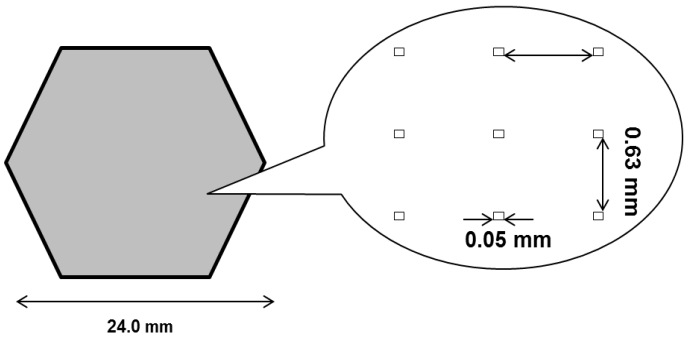


Figure 3.14 Schematic illustration of grit arrangement of new engineered abrasive pad

3.6 Approach for the evaluation of micro-hardness and subsurface damage

In addition to the analysis described in section 3.4, further analysis on the micro-hardness and subsurface damage was also captured for the study of planar contact area, as the purpose of load controlled plane grinding is to finish the workpiece surface and remove the subsurface damage introduced from previous manufacturing process. The procedure to prepare samples for micro-hardness and subsurface evaluation is listed below:

- Firstly, use waterjet to cut a 10mm x 10mm square piece from the machined workpiece disc after the grinding test. Then, use Buehler's AcuThin Cut-off Wheels (5inch in dia) for precision sectioning to reveal the cross section of the piece, and mount the piece by hot mounting press.
- The section was prepared by grinding and polishing processes on Struers Tegramin-20 polishing/grinding machine to reveal the subsurface microstructure. Table 3.2 shows the steps of polishing/grinding process.
- After each step of grinding or polishing, the sample will be cleaned by detergent and Industrial methylated spirit (IMS), and taken to the drier
- Micro etching will be done, after grinding/polishing, to reveal the general microstructure. The enchant used is Glyceregia (15cc HCl +10cc Glycerol + 5cc HNO3).

Table 3.2 Surface preparation steps for micro-hardess and subsurface analysis

Preparation steps	Surface	Abrasive type	Speed(rpm) Platen/head	Force(N)	Time(min)
Plane grinding (water cooled)	Sic Foil # 220	/	300/150	25	1:00
Fine grinding	MD Largo	DiaPro Allegro/Largo 9µm	150/150	40	5:00
Polishing	MD Dac	DiaPro Dac 3µm	150/150	20	4:00
Oxide polishing	MD Chem	OP-S, 0.04µm	150/150	15	3:00

Once the sample has been prepared, it will be sent to Buehler MicroMet micro-hardness tester-Vickers for micro-hardness testing (Figure 3.15). The procedure to conduct this is shown as follows:

- The indenter is pressed into the sample by an accurately controlled test force.
- The force (100gf) is maintained for a specific dwell time, normally 10 -15 seconds to avoid elastic recovery.
- After the dwell time is complete, the indenter is removed leaving an indent in the sample that appears square shaped on the surface.
- The size of the indent is determined optically by measuring the two diagonals of the square indent.
- The Vickers hardness number is a function of the test force divided by the surface area of the indent.
- Loads are applied starting from 20µm (the lowest depth required to leave a clear indentation mark) beneath the machined surface with and increment of 5µm.

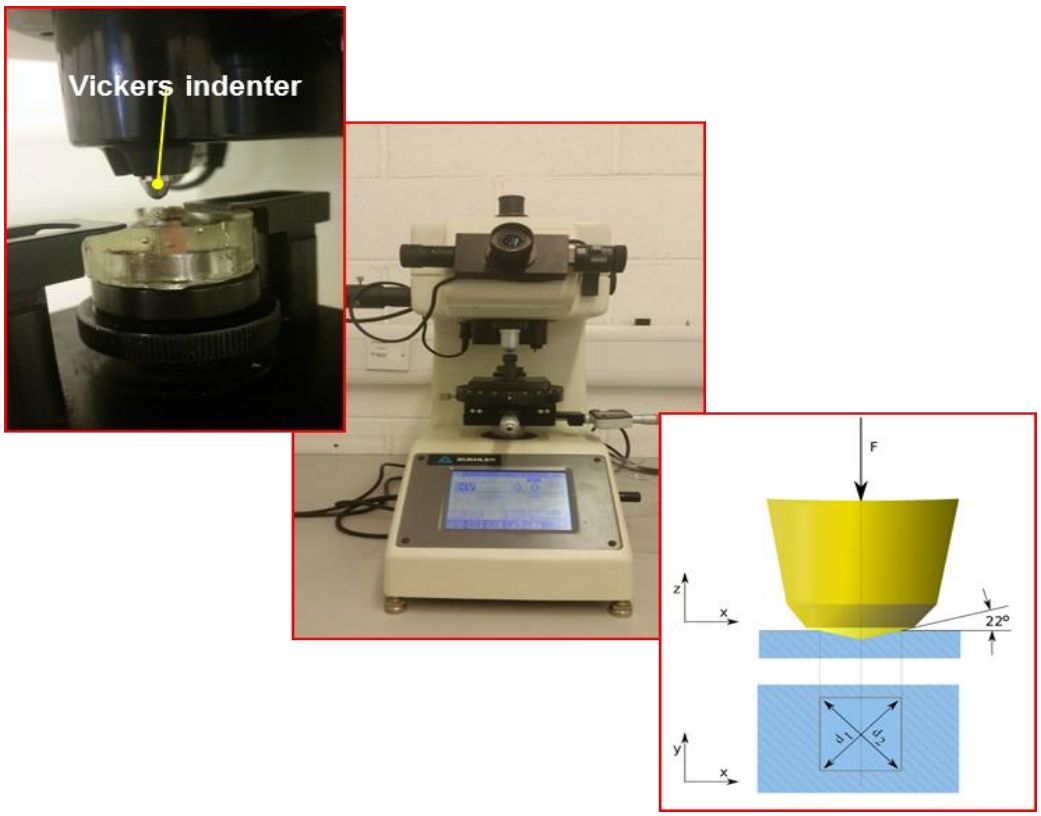


Figure 3.15 Buehler MicroMet micro-hardness tester-Vickers for micro-hardness testing and Vickers micro-hardness test scheme

The Subsurface damage captured by SEM was right beneath the machined surface. Generally, a layer of plastic deformation on the top of the material can be seen from the cross section view as shown in Figure 3.16. By evaluating the thickness of subsurface damage and variation of micro-hardness beneath machined surface, the grinding performance can be further analyzed.

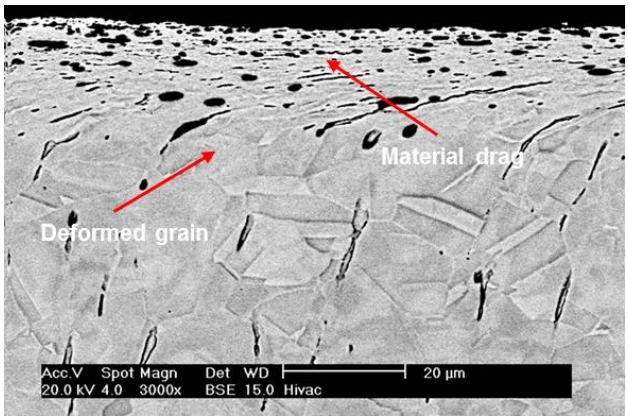


Figure 3.16 Example image of machined subsurface characteristics of 304 stainless steel

3.7 Approach to determine the planar contact area: linear scratch test setup

After evaluation of planar contact area, a scratch test was carried out to determine the engaging planar contact area and specific removal volume of conventional abrasive pad (MD-Piano 220). The approach discussed in section 3.3 were used to produce PLA abrasive pads (square frustum grits) having equivalent engaging planar contact area of conventional abrasive pad. Linear scratch test was also conducted for PLA pad to measure the specific removal volume and made comparison to conventional abrasive pad, which enabling the improvement of engineered pad design by adjusting planar contact area.

During the grinding operation the active grains on the abrasive surface pass through the workpiece and remove the material, therefore only active grains will leave scratches on the workpiece surface. Therefore, scratch test is helpful to determine the real planar contact area and volumetric removal of conventional grinding pad with random protrusions. The scratch test was conducted on the Tegremin-20 grinding/polishing system, the setup is shown in Figure 3.17. The abrasive pad was attached on the dummy as previous inverted tests, the pin is used to apply the load. Tests were conducted on the Piano 220 pad after 20 minutes of grinding at orientations in a selected cutting direction designated as 0^0 followed by a repeat test at 90^0 to the initial cutting direction ensure the capture of the material removal information of overlapped abrasives. During the test, sample material (304 stainless steel) was carefully guided through the machine for a distance of approximately 20 mm at approximately 50 $mm.s^{-1}$. Measurements were made of the scratch depth at selected sites and the specific volume of material removed was demined using a measured

distance of 0.1mm on the Alicona G5 (at 20X objective). Similar tests and measurements were conducted on two laser generated abrasive pads designed to have an equivalent total planar contact area to a Piano 220 pad at 30N. One pad having square frustum grits and the other having an equal abrasive size and layout but incorporating a dimpled relief of 40um diameter and 10μm deep on the abrasive grit contact face.

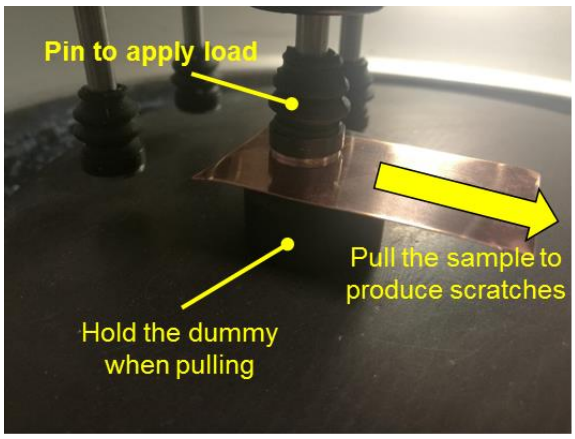


Figure 3.17 Linear scratch test setup on Tegremin-20 system

The cross-sectional scratch profile was taken by Alicona to determine the planar contact area. Assume the general geometry of grains are spheres based on Chen's model [16], planar contact area of each active grain can be calculated by the profile of scratches. In Figure 3.18, the diameter of the spherical grit is assumed to be the width of the scratch, and the planar contact area can be calculated as the area of the circle.

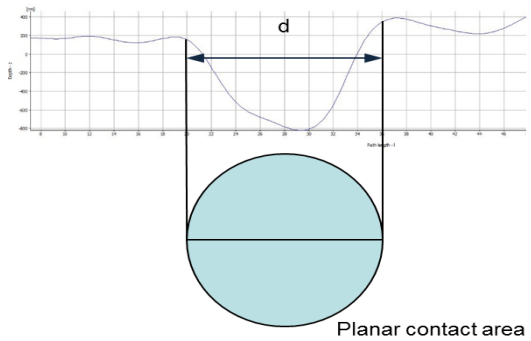


Figure 3.18 Cross-sectional profile of a scratch generated by conventional abrasive grit and the spherical interpolation of this active grit to calculate planar contact area

3.8 Modelling approach and validation for surface roughness prediction

In order to predict the surface roughness produced by engineered abrasive grits, this section will briefly introduce how to geometrically model the workpiece surface roughness that results after grinding process with defined grit shapes in real (slippage) contact conditions between workpiece and abrasive tool. In this respect, the 2D kinematic model of single and multiple grits trajectories in planetary grinding system was combined with the z-axis map of the geometrically defined abrasive grits (obtained by laser ablation) and used to output a real 3D workpiece surface profile. To emulate the real grinding process, the model contains the experimentally measured slippage of the abrasives relative to the workpiece, the setup for capturing the slippage is shown in Figure 3.19. The setup is based on the inverted setup described in section 3.4.1, the abrasive pad was fixed on the cylindrical dummy and located in the mover plate, and an aluminum pin was fixed on the top of dummy and go through a PST-360 rotational sensor. When the dummy rotates, the rotational sensor was able to capture the variation of angles. The details of model are covered in Chapte 5.

The validation trails was conducted on the Tegremin-20 grinding/polishing system, while the position of workpiece material and abrasive pad were reversed (Figure 3.8).

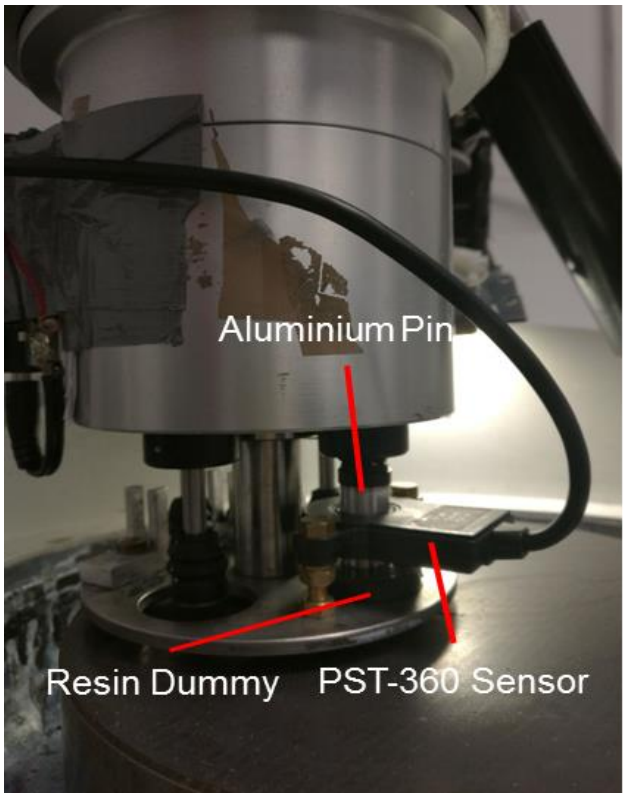


Figure 3.19 Experimental Setup for capturing the slippage between abrasive pad and workpiece by PST-360 rotary senor

By using the inverted setup, the following working parameters (same as section 3.4.1) were used: head speed=100rpm; disc speed=200rpm; Force= 20N, which are pre-optimized in previous work [8], and the operation time is 10s. Figure 3.20 shows that the induced slippages of abrasive pad were captured by PST-360 angular position sensor, and then the signals were transmitted wirelessly between two series 1 Xbee modules. The setup are two Arduinos micro controller, each attached to an XBee Series 1. The coordinator XBee reads the analog values from PST-360 sensor and tranfer the values via the XBee to the other Arduino attached with end XBee. The analog data read from the sensor is between 0 and 1023, in order to convert these to actual angles (degree), they need to be multiplied by 0.44. An example of conversion is shown in Figure 3.21.

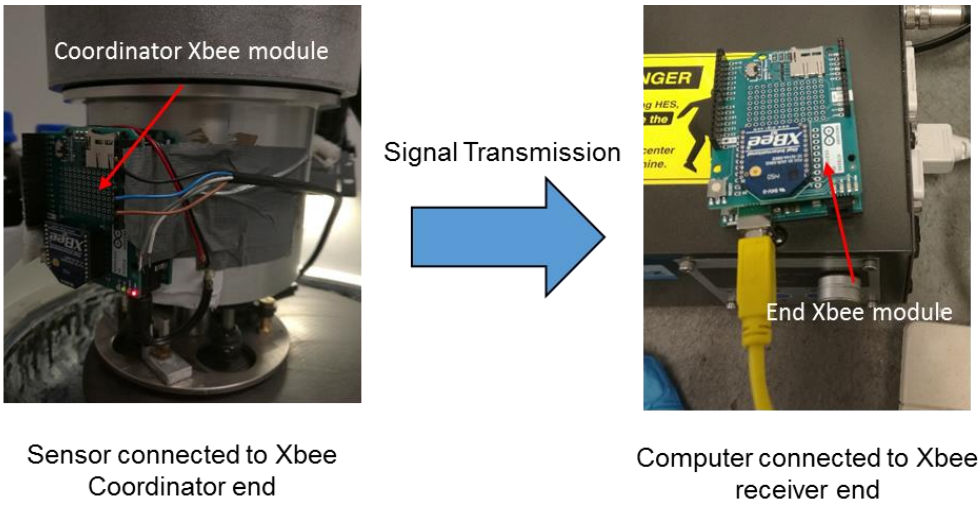


Figure 3.20 Wireless signal transmission system

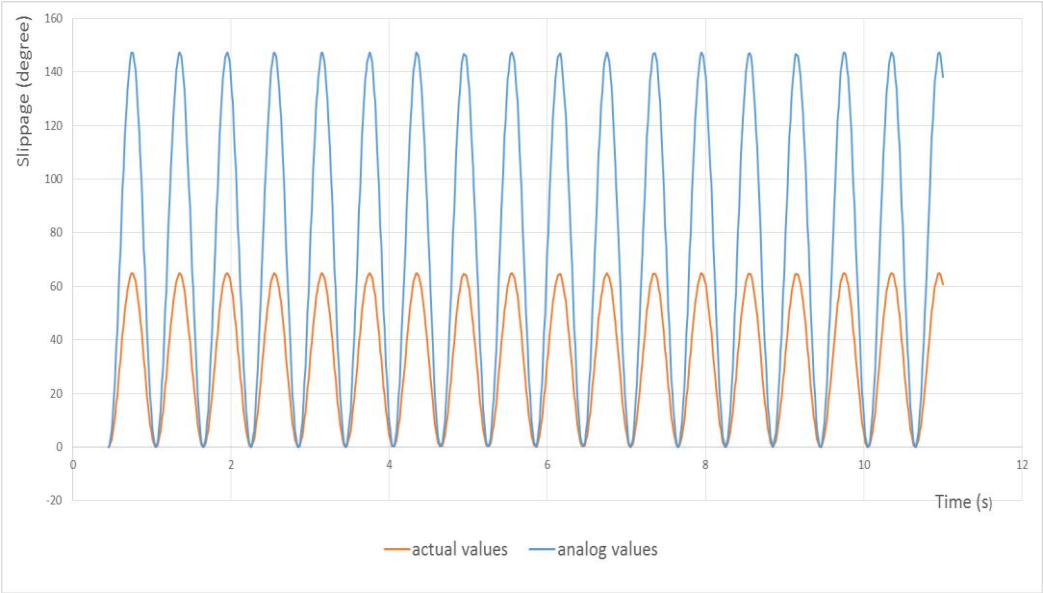


Figure. 3.21 Example of analog angle data conversion to actual angle data

The micro array (Figure 3.22) for validation test has been generated by utilizing proprietary technology for the laser generation of abrasive surfaces on polycrystalline chemical vapour deposition diamond solid structures described in section 3.3. Table 3.3 shows the specifications of the micro array for validation test.

Table 3.3 Specifications of micro array for validation test

No. of grits	Grit size	Single grit surface area	Total contact area	Base area	Distance between grits
	μm	mm^2	mm^2	mm^2	μm
25	50	0.0025	0.0625	100	950

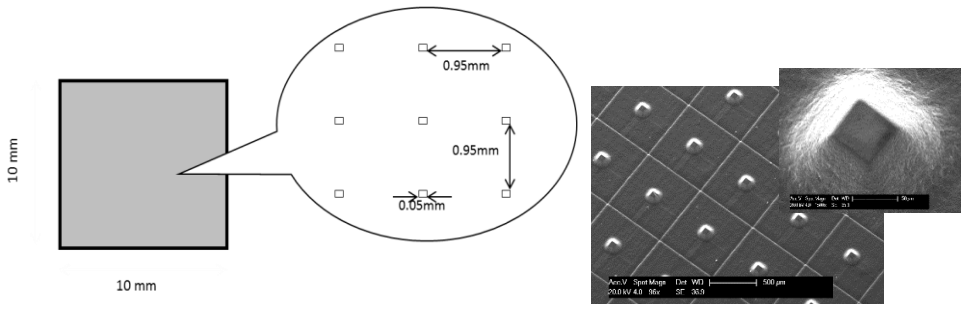


Figure. 3.22 Schematic illustration of grits arrangement and SEM image of the micro array for validation test (25 grits in total)

Once the validation trial is done, the scratched surface was scanned using an Alicona on three locations (20mm, 40mm, 60mm away from the centre) radially across workpiece disc with equal area as simulated surface to allow the evaluation of surface roughness. The scanned surface roughness have been compared with the geometrically simulated surface roughness (Done by Matlab, the code is shown in appendices) for the validation.

3.9 Conclusions

This section aims at summarizing the previously described methodology used to conduct the research and achieve the objectives of this thesis. According to section 3.2-3.8, the key points can be summarized as follows:

1. The selection of material (described in section 3.2) for manufacture of laser ablated micro arrays was done based on the hardness (resistance to wear) and structure, which enables the

understanding of how the material may influence the cutting performance. For this reason, polycrystalline CVD diamond was selected as its superior performance other superabrasive materials. In addition, 304 stainless steel was selected to be the workpiece material as its hard to grind nature can be used to test the capability of engineered abrasive tool.

2. As described in section 3.3, PLA abrasive array was generated as an emulation of Struers MD-Piano 80 plane grinding pad, in order to compare the performance with conventional tools. The criteria to select the grit geometry for PLA pad is the utilization of cutting edges during operation (symmetry), as a result square frustum and saw tooth grits were manufactured for the test. The laser processing is enabled by a hybrid laser machining centre equipped with a Nd: YAGQ-switched pulsed laser, and the parameters adopted are preoptimised.
3. In the process of testing PLA abrasive array and conventional abrasive array (described in section 3.4), an inverted test setup was adopted which allows to minimize the PLA abrasive grits to be manufactured for cost and time efficiency purpose (section 3.4.1). A benchmark procedure is set to allow the evaluation of the data from the grinding test for both conventional and engineered abrasive grits:
    a) Characterization of tool geometry and examine their wear mechanism. Identification of the influence of wear mechanism on the workpiece material. (section 3.4.2)
    b) Identification of the workpiece surface topography progression and material removal rate. (section 3.4.3)
    c) Evaluation of the material removal mechanism. (section 3.4.4)
4. Two PLA engineered abrasive pad (different planar contact area) emulates the dimensional characteristic of MD-Piano 220 pad was

produced to study the influence of planar contact area on grinding performance (specification details in section 3.5). Same testing conditions and procedures described in section 3.4 was employed. In addition, further analysis on the micro-hardness and subsurface damage was also studied (section 3.6).

5. Linear scratch test (section 3.7) was used to determine the engaging planar contact area and volumetric removal of Piano 220 pad. Spherical interpolation was adopted to calculate the planar contact from grit cross-sectional profile. Based on the planar contact area derived from scratch test, PLA abrasive pads emulating the planar contact area of Piano 220 was produced (with and without dimple on the top), in order to study the influence of planar contact area on the material removal rate.
6. Section 3.8 explains the geometrical model, which allows to predict the surface roughness generated by engineered abrasive grits. The model was developed under the inverted test condition, and also took the consideration of the slippage between abrasives and workpiece (experimentally determined). A testing PLA array with 25 grits was generated on the laser system described in section 3.3. A wireless transmitting system consists of two Xbee units and one PST-360 angular position sensor were employed to measure the slippage between abrasive grits and workpiece. Once the validation trial is done, the workpiece surface was scanned by Alicona on three locations, and then compared with corresponding simulated surfaces in terms of surface roughness.

Chapter 4

Evaluation of influence of grit geometry on the grinding performance

This chapter contains the results achieved in testing the PLA micro arrays with engineered abrasives (i.e. square frustum and saw tooth) and conventional abrasive grits (irregular shape as discussed in section 2.2.3), which enables the study of influence of different grit geometries on their performance in load controlled plane grinding operation. It also allows the evaluation of engineered abrasive grits over conventional abrasive grits, providing specific types of geometries can be employed for design of engineered abrasive tool for future studies. In particular, it contains:

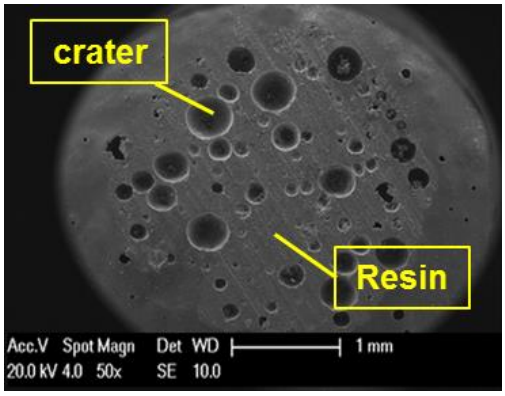
1) Characterization of conventional/engineered abrasives before testing
2) Evaluation of tool wear mechanism
3) Response of surface topography and material removal rate to the engineered and conventional abrasive grits
4) Material removal mechanism of scratched/ground surfaces

4.1 Characterization of abrasive grits

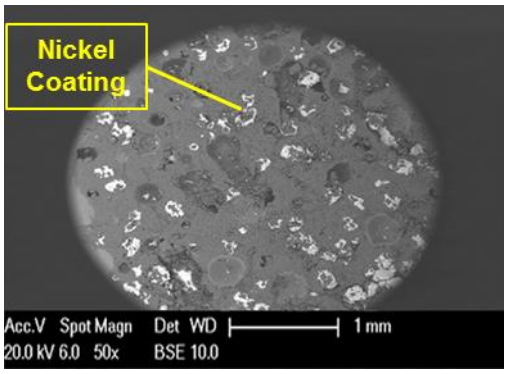
As described in section 3.2, conventional abrasive grits were cut from Struers MD-80 Piano plane grinding pad, while PLA abrasive grits were emulating the size and arrangement of MD-80 Piano pad. For PLA grits, both square frustum and saw tooth geometries were generated. In order to acquire an in-depth understanding of how the surface topography and material removal rate are influenced by grit geometry, it is necessary to conduct a full characterization of abrasive grits before the grinding test.

The methodology and procedure to characterize abrasive pad and grits are described in section 3.3.2 in detail.

Both the conventional and PLA abrasive grits have been characterized by SEM. The overview images of conventional abrasive pad (as discussed in section 3.2) before grinding (i.e. in fresh conditions) are shown in Figure. 4.1 (a) and (b). It can be observed, in this stage, most of the abrasive grits are not visible due to the resin bonding (Figure. 4.1 a), and some craters are located across the abrasive pad surface, which are deliberately introduced during the manufacturing process which are likely to hold fluids and help chip flow.



(a)

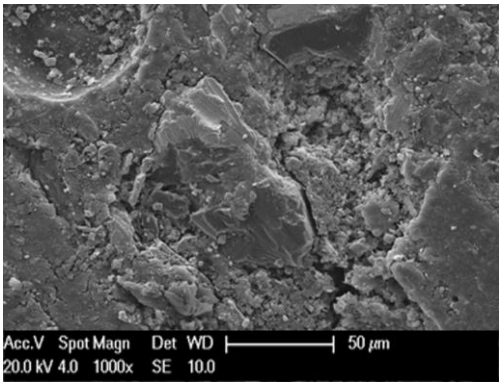


(b)

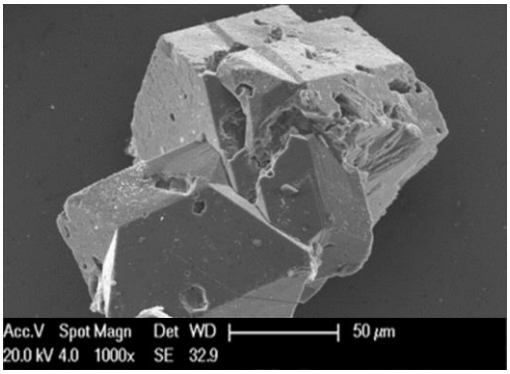
Figure 4.1 SEM images (before grinding) of (a) conventional abrasive surface (b) BSE of conventional abrasive pellet

In order to give some indications on where the grits are located and the approximate number of grits, BSE image also has been taken for the overview of abrasive pad (Figure 4.1 b). It can be found that the zones

surrounded by bright sites are the locations of diamond grits as indicated by their nickel coating encapsulations (Figure. 4 a).



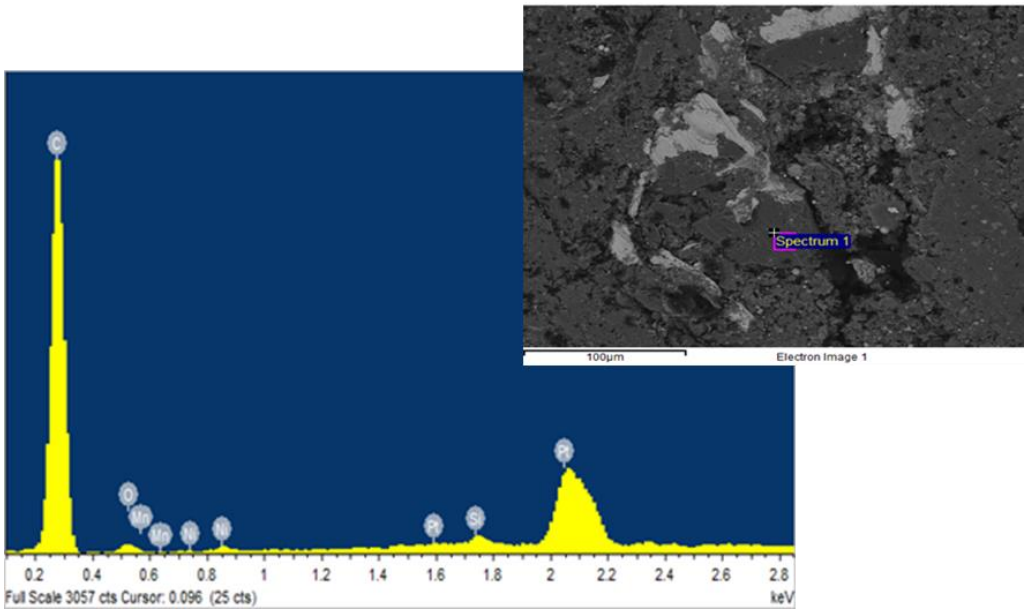
(a)



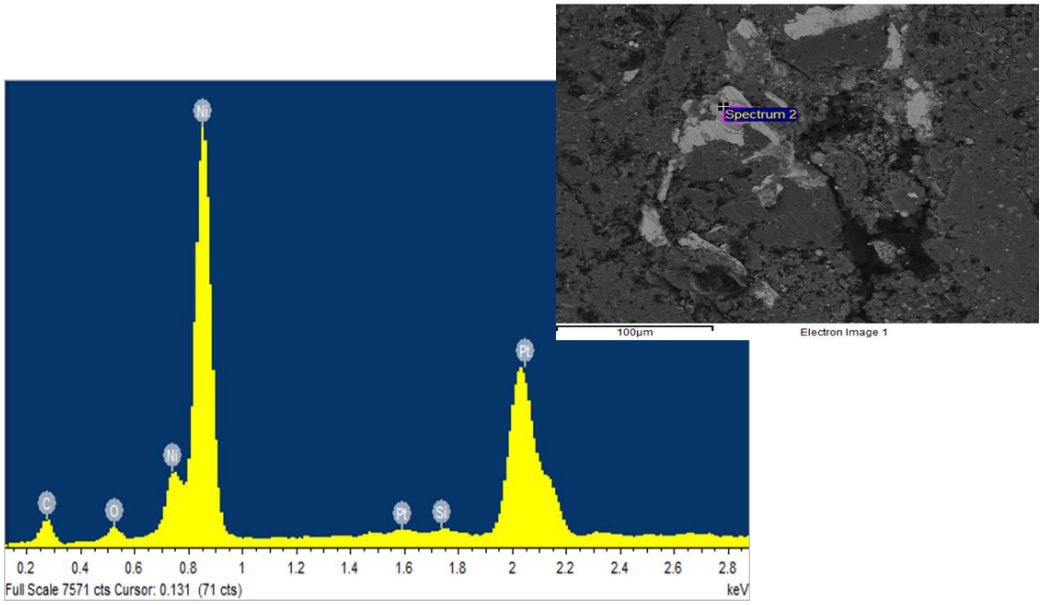
(b)

Figure 4.2 SEM images (before grinding) of (a) conventional abrasive grit bounded by resin and (b) uncovered conventional abrasive grit

Figure. 4.2 (a) presents one selected abrasive diamond partially buried in the resin and it shows clear evidence of stochastic nature of conventional abrasive grits of irregular shape. Figure 4.2 (b) further illustrates the stochastic nature by showing the uncovered grit, features like cleavage planes and micro cutting edges can be clearly observed from it. Besides the crystallographic features, Energy-dispersive X-ray (EDX) analysis is also used to identify the existence of diamond. As shown in Figure 4.3, the element composition reveals that the dark phase surrounded by the bright phase is diamond grit, and the bright phase is nickel coating on the diamond grit.



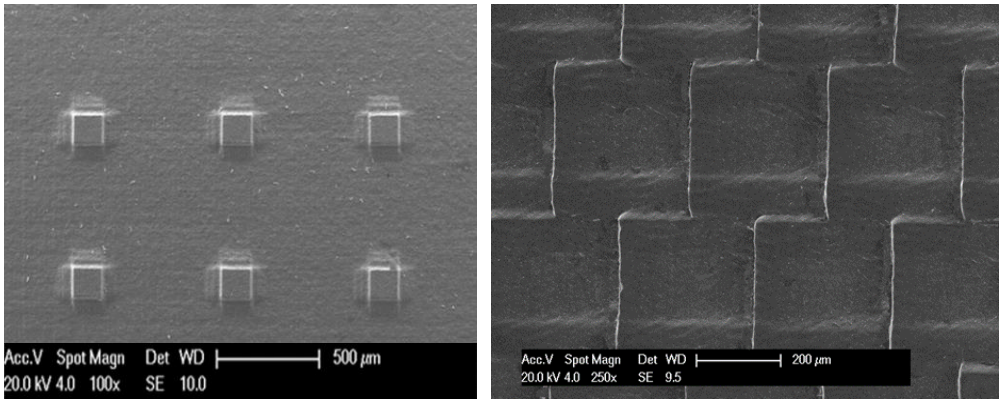
(a)



(b)

Figure 4.3 EDX analysis of (a) buried diamond grit (b) nickel coating on the diamond grit

The polycrystalline structure of conventional grits contributes to multiple cutting edges and make the edges easier to break down by abrasion and to facilitate the cutting. Besides this, the cleavage planes and relatively weak grain boundaries are likely to fracture (split apart) during grinding process.



(a) (b)

Figure 4.4 SEM images of PLA engineered abrasive pad with: (a) square frustum girts (b) saw tooth grits

In contrast to conventional abrasive grits, both PLA square frustum and saw tooth grits (Figure. 4.4) in each case have identical protrusion heights and defined cutting edges. It can be observed that the spacing between grits are well defined which can provide good chip flow paths. As the engineered cutting edges are made of polycrystalline CVD (no binder phase) diamond, and with its columnar structure with integral growth planes (as discussed in Chapter 2) due to the well-controlled nucleation process, during the grinding process grain fracture is likely to occur across the nucleation face or along the growth boundaries of its columnar structure, being the weaker regions of this material.

4.2 Preliminary evaluation of the influence of grit geometry on the finishing performance for engineered abrasive grits

Before conducting the grinding test described in section 3.3.1, the preliminary test was conducted to evaluate the performance of two types of grits with different geometries: symmetric (i.e. square frustum) and

asymmetric (i.e. saw tooth). As the possible options for defined grit geometry are numerous, it is important to set these two generic types and gain an understanding of their finishing performances, in order to select appropriate geometry for further analysis. Figure 4.5 shows the proposed types of grits utilized in the test.

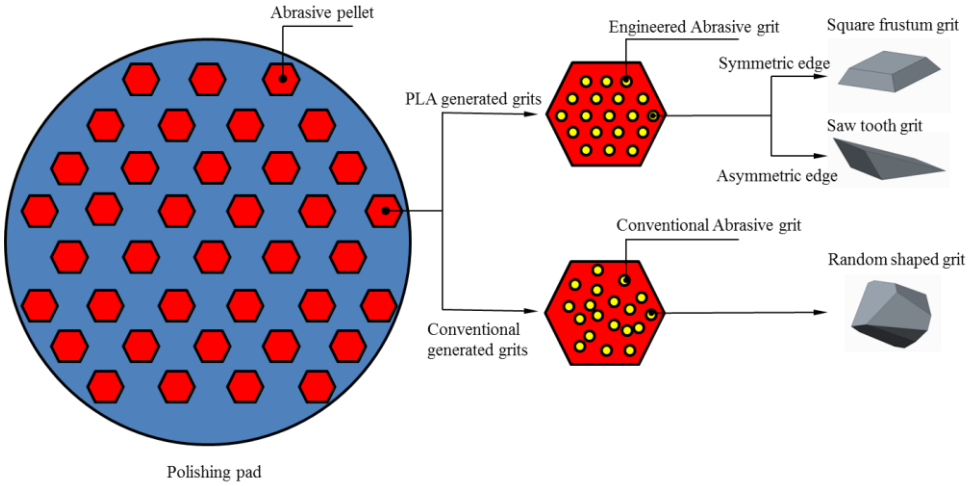
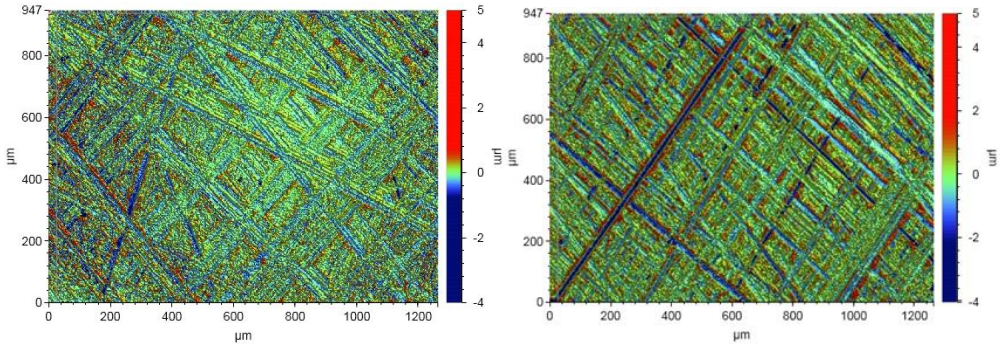


Figure 4.5 Schematic illustration of proposed types of grits

Basically, the main difference between these two types of grits under planetary motion (e.g. plane grinding), as discussed in the section 3.2, is the utilisation of their effective cutting edges during grinding process.



Sa=0.217µm Sa=0.298µm

(a) (b)

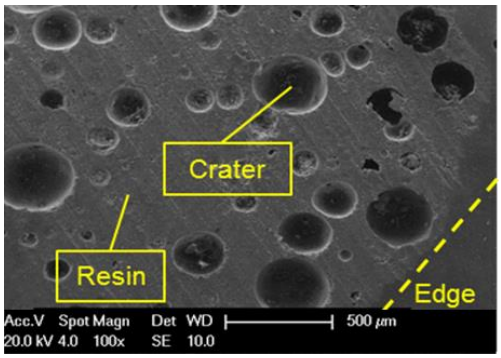
Figure 4.6 Surface micro-topography generated after 5 minutes of grinding by: (a) square frustum abrasive (b) saw tooth abrasives

For the preliminary testing, two surfaces were generated by abrasive pads with square frustum grits and saw tooth grits respectively for 5 minutes, whose details are covered in section 3.2. According to surface topography captured in Figure 4.6, it can be observed that the scratches generated by square frustum grits are more uniform, while the scratches generated by saw tooth grits are more random in width and depth (Fig. 4.6 b). This reveals that the cutting edges of square frustum are more stable in its transient cutting direction when rotating with the grinding pad. It can be concluded that, although, saw tooth grits have excellent cutting performance under a linear tool path, they become less efficient in the aspect of achieving a better surface finish compared with square frustum grits under planetary movements. When both types of grits rotating with respect to a central axis, the effective cutting orientations will be dominant for square frustum grit due to its symmetric geometry. However, it is a different case for saw tooth grit, rotation will deviate the cutting edge from its effective orientation during most of the grinding time. In addition, the values of surface roughness also provide the evidence that square frustum grits can produce better surface finish in grinding process, hence leading to the conclusion that, in the grinding operation (i.e. planetary movement) the grits with symmetric cutting edges (e.g. frustum grits) are superior to the performances of the asymmetric girts (e.g. saw tooth). For this reason, the use of asymmetric grit shapes will not be taken any further, and the follow-up analysis has been focused on examining the symmetrical grits (square frustum) when compared with the conventional randomly shaped abrasive grits.

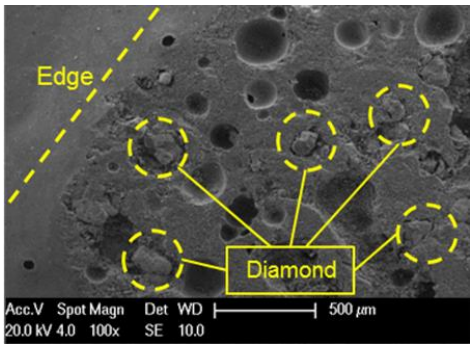
4.3 Evaluation of tool wear mechanism

From the work on the characterization of engineered and conventional abrasive grits before the inverted test (section 4.1), their morphology and

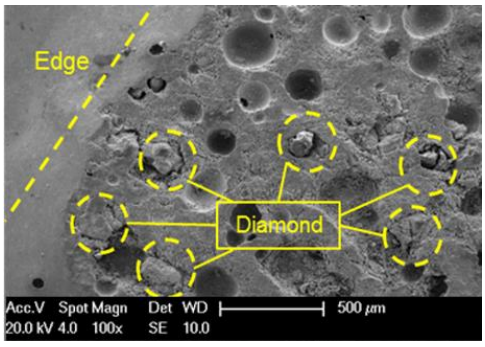
some possible wear mechanism has been discussed. In order to fully exploit the tool wear mechanism and build a correlation between this and finishing performance, characterization of tools after the inverted test was conducted by SEM.



(a)



(b)



(c)

Figure 4.7 The conventional abrasive surface after (a) 0 min (b) 10 min and (c) 20 min of grinding

Overview images of conventional abrasive pad after grinding tests were depicted in Figure 4.7. The progressional time behavior of the conventional abrasive surface caused by abrasion between abrasive surface and workpiece surface shows the resin bonding being gradually broken down and the exposure of grits becames higher compared to its initial state; in addition, some evidences of grit pull-out leaving new craters on the abrasive surface has been observed.

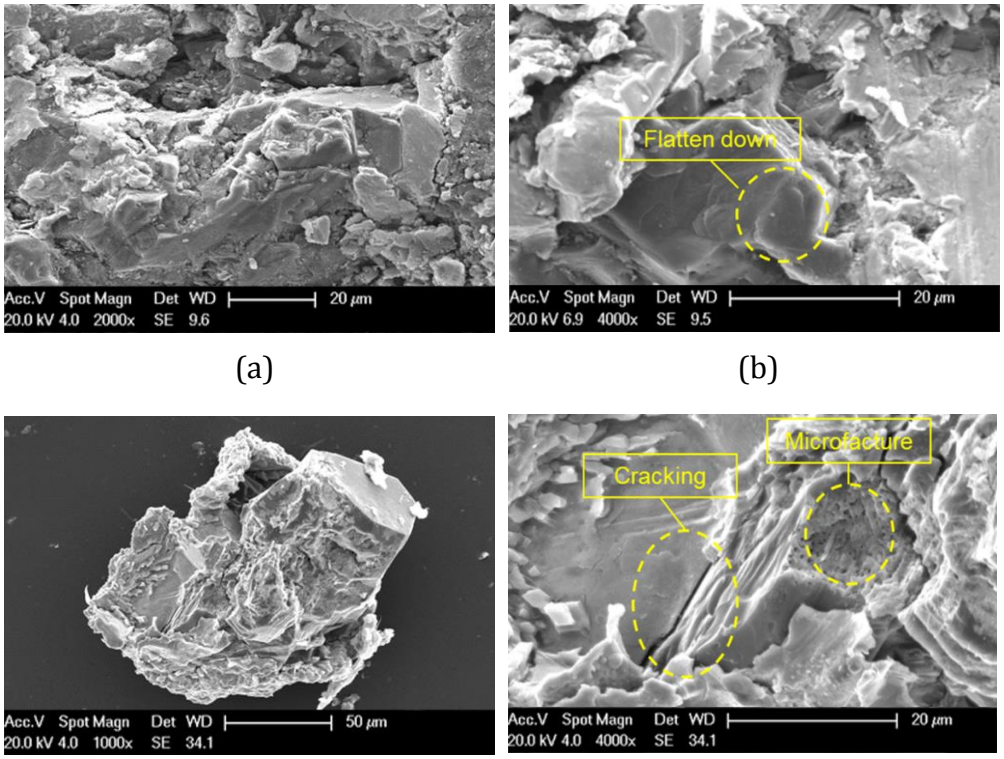
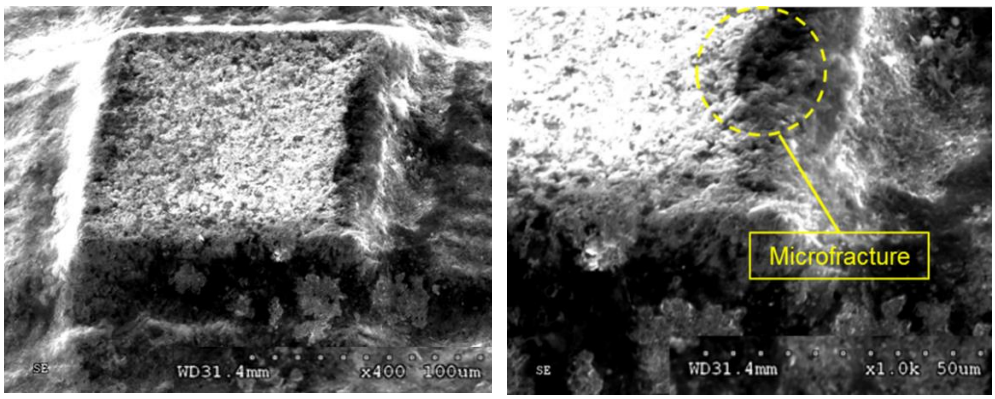


Figure 4.8 (a) Conventional abrasive grit after 20min grinding; (b) High magnification image of conventional abrasive grit after 20min grinding; (c) Uncovered conventional abrasive grit after 20min grinding; (d) High magnification image of uncovered conventional abrasive grit after 20min grinding

SEM images of higher magnifications have been taken to further investigate the wear mechanism of conventional abrasive grits (Figure 4.8). After 20 minutes of grinding, the conventional abrasive grit exhibits clear evidence of microfracture on the grit surface (Figure 4.8d). The original geometry of the grit has broken away to increase the number of secondary cutting edges. In addition to microfracture, cracking can be observed at the center of the grit along the cleavage plane. Due to repeated abrasion, it also can be seen that flattening effects occurred on the abrasive surface (Figure 4.8 b). Referring to Figure 4.8 (a), very few debris and workpiece material built-up can be observed, which is probably due to the large grit size and spacing between grits.



(a) (b)

Figure 4.9 (a) Square frustum engineered grit after 20min grinding; (b) Higher magnification image at the grit corner

For comparison, the micrograph of square frustum grits after 20 minutes of grinding were also taken (Figure 4.9). In contrast to conventional abrasive grits, the edges of square frustum grits nearly remain intact at this test interval. Few microfractures can be found on the nucleation surface around the edges of grit, as well as, the material built-up (Figure 4.9 b). As polycrystalline CVD diamond thick film has a compact integral columnar structure (Refer to Section 2.1.4), its wear resistance is better than the synthetic polycrystalline diamond grits with more haphazard crystalline structure used in the conventional tool. Moreover, the darker phase around the edges also exhibits the trace of ablation from the PLA generation of the grits.

4.4 Response of surface topography and material removal rate to the engineered and conventional abrasive grits

In this section results of progression of surface topography (surface roughness) and material removal rate are illustrated. The influence of

engineered and conventional abrasive grits on the variation of topography and material removal rate has been discussed, which aims at understanding the how the grit geometry and arrangement can affect finishing performance. The progression of surface roughness for both engineered and conventional abrasive pads is reported in Figure 4.10.

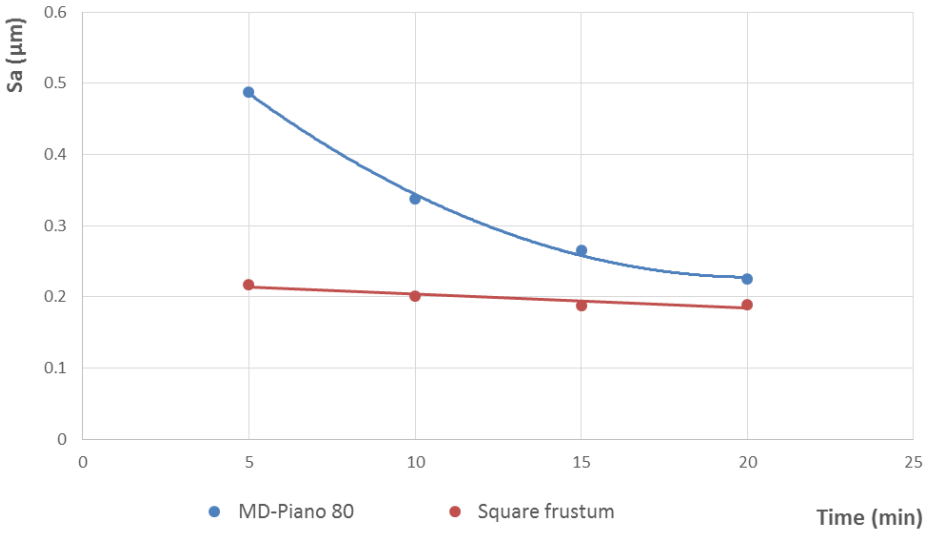


Figure 4.10 Variation of surface roughness generated by square frustum and conventional abrasives through the entire grinding process

The results clearly depicted the difference between surface finish achieved by square frustum abrasive grits and conventional abrasive grits. By analysing the performances of the square frustum grits and that of conventional random grits in Figure 4.10, it was observed that conventional abrasive grits produced worse surface roughness (0.488µm) than square frustum grits (0.217µm) at 5 minutes. This initial analysis revealed the advantage of square frustum grits to achieve better surface finish than that of conventional abrasive grits.

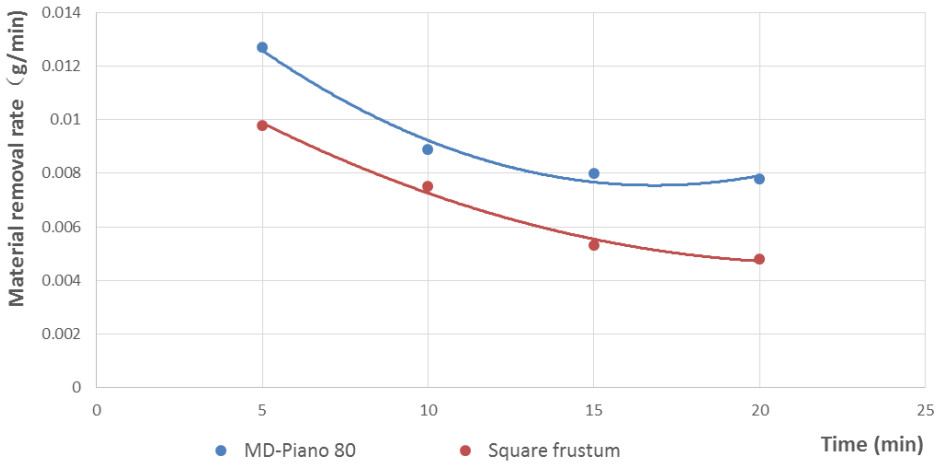


Figure 4.11 Variation of material removal rate generated by square frustum and conventional abrasives through the entire grinding process

The results of progression of material removal rate for both square frustum and conventional abrasive grits are shown in Figure 4.11. By comparing the material removal rates between square frustum grits and conventional grits, it showed that the removal rates of square frustum girts, which is 0.00980g/s at the beginning and 0.0048g/s in the end of the process, are lower than that of conventional grits, which is 0.01270g/s at the beginning and 0.00780g/s in the end of the process. This gives a preliminary indication that conventional grits are superior to square frustum grits in the aspect of material removal.

4.4.1 Response of surface topography to the engineered and conventional abrasive grits

By comparing the surface texture, there is strong evidence that conventional grits produced random and pronounced scratches, resulting in rougher surface texture compared to that produced by square frustum grits (Figure 4.12 a,b,c). In contrast to the previous, square frustum grits with their orderly distributed/defined cutting edges generated smoother

surface texture with more uniform coverage of grinding scratches (Figure 4.12 d,e,f).

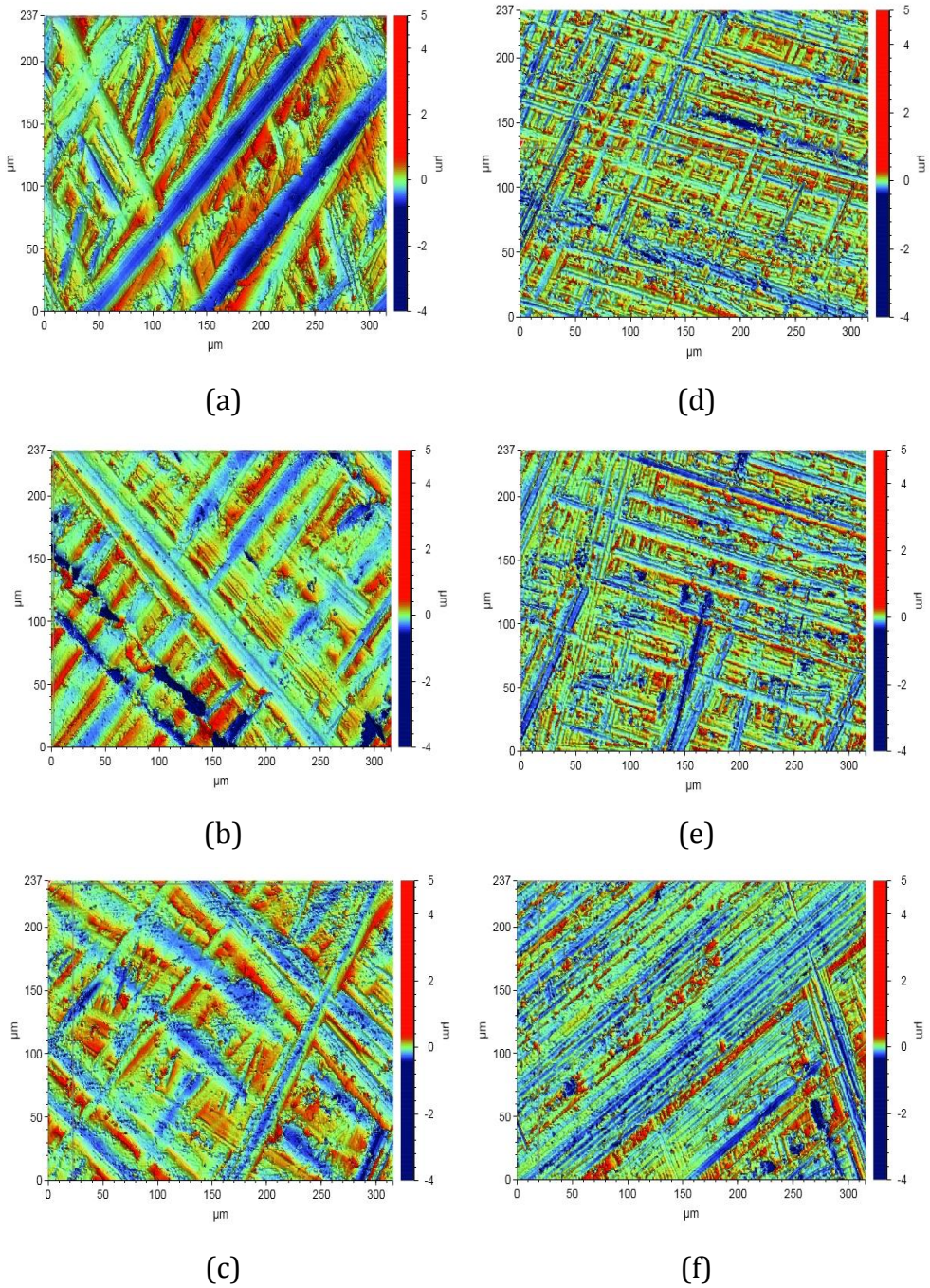


Figure 4.12 Surface topography generated by conventional abrasive grits after: (a) 10 minutes (b) 15 minutes (c) 20 minutes of grinding; Surface topography generated by square frustum engineered abrasive grits /pellet after: (d) 10 minutes (e) 15 minutes (f) 20 minutes of grinding

However, it was observed that the difference in value of surface roughness (Figure 4.10) between conventional and square frustum grits was significant at the beginning of the process (0.271μm) and gradually decreased to a relatively low level (0.036μm). As previously discussed, most of the grits were buried in the resin bonding before the engagement into the workpiece, thus they were inactive at the beginning of the grinding process and the exposure of grits increased with elapsed testing time. Moreover, the pull-out of girts and the micro/macro fracture on the grit surface after several minutes of grinding result in secondary cutting effects on the workpiece. As a result, the transitory stage for conventional grits to achieve a stable level of surface roughness (e.g. Ra= 0.225μm) can be lengthy (e.g. 17min), while square frustum engineered grits are active and their cutting edges remain well defined through the process, which enables better surface roughness (e.g. 0.189μm) right after 5 minutes of grinding (Figure 4.10).

Table 4.1 Comparison between worn and fresh conventional grits

Type of grits	Length of grinding(min)	Surface roughness(μm)
Worn	5	0.328
fresh	5	0.488

In order to investigate the effects of number of grits exposed during the grinding test on the generated surface roughness, a validation test was conducted by using conventional abrasive grits being employed for 20 minutes (full exposure of grits). Result is shown in Table 4.1, after 5 minutes of grinding, the surface roughness was significantly improved (0.328μm) compared to the surface roughness (0.488μm) generated by unworn conventional abrasive surface (low exposure of grits). Taking into consideration of the above results, it can be concluded that abrasive

grits with defined geometries and arrangement not only generate better surface finish but also reduce the time to achieve desirable surface finish.

4.4.2 Response of material removal rate to the engineered and conventional abrasive grits

It is noteworthy that material removal rate follows the similar trend as surface roughness improvement where the removal rate is high initially and then gradually decreases to a stable level (Figure 4.11). The decrease in removal rate is likely to be due to a flattening effect and a clogging effect. Grinding is a process to prefentially remove the high peaks on the workpiece surface by repeated abrasion. The initial abrasion will remove the peaks in a relatively fast rate due to the amplitude differences between peaks and valleys, as the peaks flatten down the contact area between the abrasives and workpiece is increasing resulting in decrease in cutting pressure. In addition to flattening effect caused by increasing contact area, material built-up in the grinding process resulting in clogging which also may decrease the removal rate. Clogging can reduce a greater part of the load on the abrasive particles and the space between the abrasive particles, which will result in lower removal rate. Moreover, clogging could be expected to cause wedging and ploughing rather than cutting and give rise to comparatively less wear. However, in both cases no predominant clogging of the surfaces was observed, which is likely due to the relatively large grit size and spacing for conventional abrasive grits (MD-Piano 80) and well defined chip flow path for square frustum grits. Thus, the flattening effect could have predominant effect on the decreasing removal rate of the grinding pads. The material removal rate of conventional abrasive grits is found to be higher (67%) than the material removal rate of square frustum abrasive grits. This can be explained as the effects of

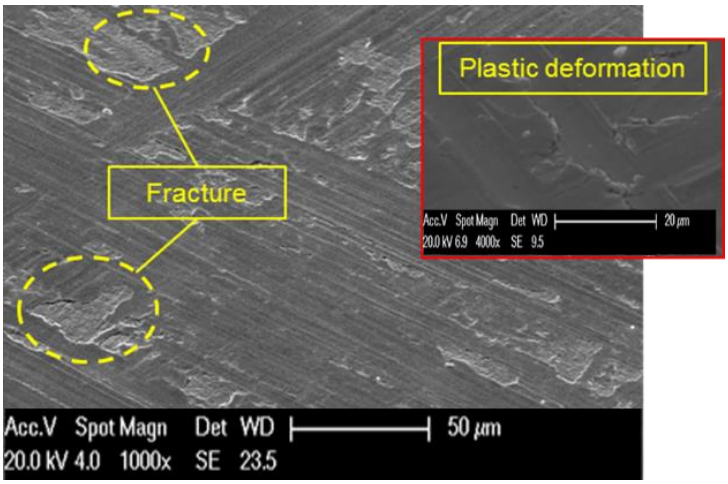
attack angle and sharpness, conventional abrasive grits have random cutting edges which are sharper with higher attack angles, while cutting edges of square frustum grits are blunter with lower attack angles. Rabinowicz and Mutis[73] have studied attack angle dependence on the wear rate and found shaper grits with higher attack angle tends to give higher wear rate. Besides this, the random cutting edges of conventional grits introduced more damage on the surface, the sharp cutting edges and secondary cutting effect (microfacture of grits) both contribute to plough new valleys with various depth of cut rather than remove peaks. In contrast to the above, square frustum abrasives have defined cutting edges resulting in uniform cutting depth, thus introduce less damage. As a result, the predominant effect of square frustum abrasive is flattening the surface rather than removing material.

4.5 Material removal mechanism of scratched/ground surfaces

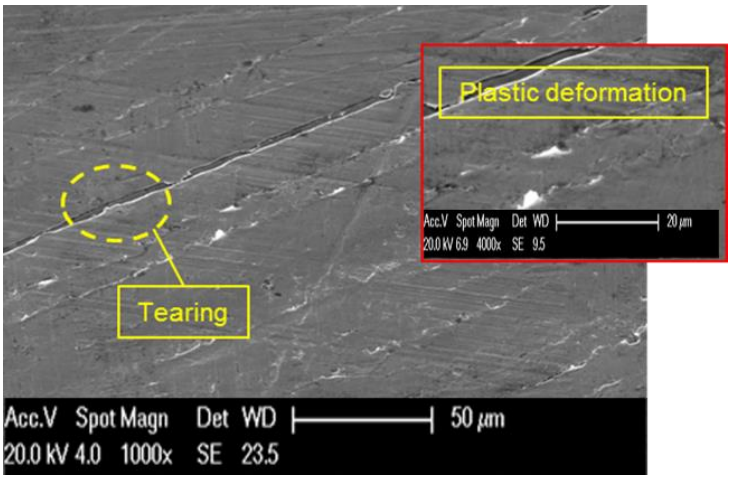
In section 4.4, a study on the topographical properties of the grinded surfaces has been achieved. In this section, it is important to characterize and investigate the mohopological aspects of the grinded surfaces in terms of material removal mechanism.

The SEM imaging gives the opportunity to investigate the mechanism by which the material is removed/ploughed under the engagement of both conventional abrasive grits and square frustum grits. As abrasive grits are well known to be acting with negative rake angles, cutting/ploughing are dominant in the case of negative rake angles. In this study, conventional abrasive grits have sharper tips with various negative rake angle than that of square frustum abrasive grits, hence the material removal mechanism of conventional abrasive grits is expected to be combination of cutting and

ploughing. For square frustum grits, the rake angle is almost negligible and as the clearance angle is zero, its large and flat contact surface is in contact with the workpiece surface. This results in a sliding contact mode between abrasive grits and workpiece material rather than cutting/ploughing mode, as the absence of abrasive grits cutting into the material due to insufficient pressure and inappropriate sharpness of cutting edges (large and flat contact area). Moreover, these two types of material removal mechanism also can be used to explain the higher removal rate for conventional abrasive grits than that of square frustum grits.



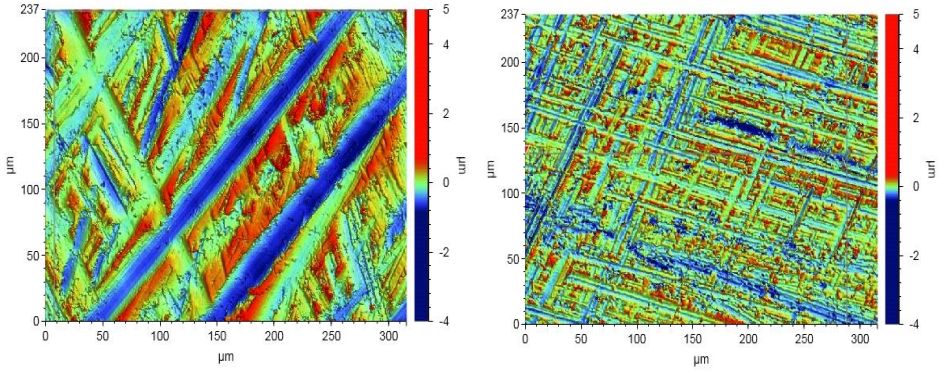
(a)



(b)

Figure 4.13 Scratched workpiece surface ground by: (a) conventional abrasive grits (b) square frustum grits after 20min of grinding

According to SEM images of the workpiece surfaces (Figure 4.13) taken after 20 minutes of grinding, both surfaces generated by conventional abrasive grits and square frustum abrasive grits shows multiple overlapped scratches. For conventional abrasive grits, there are strong evidences of plastic deformation on the surfaces (Figure 4.13a) indicating ploughing is the predominant mechanism rather than cutting. This provides evidence that the material removal on the stainless steel surface is predominantly caused by the macro geometry of the abrasive and not the micro fractures/geometries. Furthermore, except the scratches, large amount of plucking also can be observed on the surface. This is likely due to the damaging material removal caused by conventional abrasive grits with various negative rake angles and sharper tips, which tends to pluck out more material. In contrast to conventional abrasive grits, surface generated by square frustum grits also exhibit the mechanism of plucking and also be predominant by sliding and ploughing as the large amount of plastic deformation across the surface (Figure 4.13b).



Void volumes:
39.274 nm^3/nm^3
(a)

Void volumes:
19.855 nm^3/nm^3
(b)

Figure 4.14 Void volumes after 5min of grinding for (a)conventional abrasive grits (b)square frustum grits

Quantitatively, the amount of plucking can be described by the volume of material has been plucked out per unit surface area. The interferometry is used to capture the typical surface texture and determine the amount of plucking. The specific volume of material bounded by the surface texture from a reference plane at a certain height corresponding to a chosen percentage value (e.g. 80% in general) to the lowest valley is termed as void volume. The void volumes of selected sample area are calculated respectively for surface generated by conventional abrasive grits and square frustum grits. The results in Figure 4.14 showed the amount of plucking of conventional abrasive grits (39.274 nm^3/nm^3) is approximately 2 times greater than that of square frustum grits (19.855 nm^3/nm^3). This indicates conventional abrasive grits are more effective in removing material but also introducing damaging material removal and causing fractures to make the surface rougher.

4.6 Conclusions and remarks

This chapater has exploited novel design of abrasive tool with engineered abrasives for grinding process, and discussed how the workpiece surface roughness and material removal evolve with machining time. An in-depth topographical and morphological study of surfaces generated under abrasive grits with different geometries, i.e. conventional and engineered saw tooth and square frustum is presented. The key findings can be summarized as follows:

- The symmetric engineered abrasive grits (e.g. square frustum) can generate better surface roughness than that of equivalently sized non-symmetric abrasive grits (e.g. saw tooth) which indicating the influence of continuous change in cutting orientations under planetary movement. Symmetric grits tend to provide effective

cutting orientation more often during the grinding process than that of asymmetric grits. This showed that it is beneficial to employ symmetric abrasive grits for achieveing a better workipiece surface finish.

- The wear mechanisms of the conventional abrasive grits are found to be microfracture, cracking and flattening. In contrast with the above, no sign of aggressive wear can be observed for square frustum abrasive grits. Although, conventional abrasive grits have better performance on material removal (67% higher than engineered grits), it took much longer time (17min) to achieve the desired surface finish compared to square frustum grits (7min).
- Metrological examinations of the surface generated by conventional abrasive grits and square frustum grits revealed that plastic deformation is the predominant wear mechanism for both type of grits, however, conventional abrasive grits cause more plucking (approximate two times greater) on the surface than that of engineered square frustum grits. The possible explanation is conventional abrasive grits have more cutting edges with negative rake angles and sharper tips leading to more plucking mechanism. For engineered grits, the large and flat contact area result in sliding contact, hence less damage on the surface.
- Based on the above findings, it can be concluded that symetric engineered abrasvie grits (square frustum) is a good option for surface finishing purpose, while its capability of material reomving is adversely influenced by large plannar contact area. The improvement of this by adjusting planar contact area will be discussed in Ch6 and Ch7.

Chapter 5

On modelling of workpiece surface roughness when using rotary abrasive pads with engineered abrasive grits

According to the results in Chapter 4, it has been found that engineered abrasive pad with square frustum grits have superior finishing performance under load controlled plane grinding process. As the square frustum abrasive pad has defined grit geometry and arrangement, a geometrical model can be utilized to determine the machinated surface texture and surface roughness, which can not only enhance the understanding of abrasive processing with engineered abrasive grits, but also provide a preliminary modelling approach for future study of load controlled plane grinding process with engineered abrasive pad.

This chapter aims to geometrically model the workpiece surface roughness that results after a load controlled plane grinding process with defined grit shapes (square frustum) in real (slippage) contact conditions between workpiece and abrasive tool. In this respect, the 2D kinematic model of single and multiple grits trajectories in planetary polishing system was combined with the z-axis map of the geometrically defined abrasive grits (obtained by laser ablation) and used to output a real 3D workpiece surface profile. To emulate the real plane grinding process, the model contains experimentally determined slippage of the abrasives relative to the workpiece (details in Section 3.8). The validation of the model was carried out by conducting grinding trials on a ductile workpiece surface (i.e. 304 stainless steel) utilizing abrasive elements with identical grit features produced by pulsed laser ablation on thick film

CVD diamond in the common industrial operation conditions while monitoring the grit slippages using a wireless sensing system embedded onto the polishing machine (details in Section 3.8). In particular, it contains:

1) Kinematic simulation of 2D single abrasive trajectory
2) 3D material removal and surface updating algorithm
3) Validation and discussion

5.1 Kinematic simulation of 2D single abrasive trajectory

In order to facilitate accelerated validations tests, the setup of the grinding system was inverted as described in previous chapters, i.e. the position of workpiece material is fixed on the rotating platen while abrasive pad is fitted into the mover plate (Figure 5.1); this allows the simulation and manufacture of reduced number of abrasives on abrasive pads of smaller dimension in comparison with that of the workpiece while without affecting the validity of the modelling procedure.

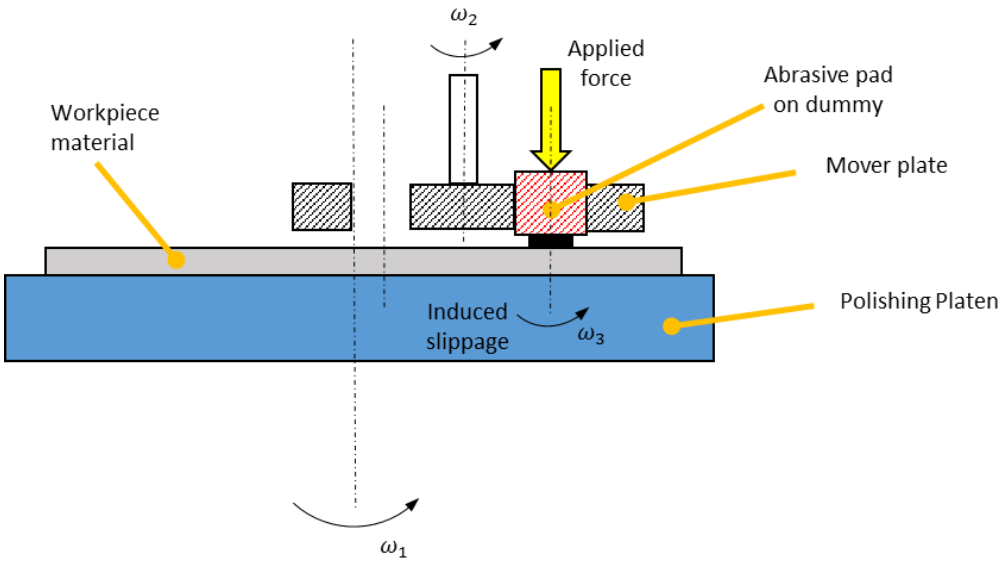


Figure 5.1 Schematic illustration of inverted test setup for modelling

There are two basic motions involved in plane grinding system, which are grinding platen rotation and mover plate rotation. In real cases, there are also some unspecified free rotations of the samples in mover plate due to slippage (ω_3 in Figure 5.1). In order to simplify the analytical derivation of 2D trajectory of abrasive girt, an assumption that abrasive pad is operating without the unspecified free rotation has been made. Alternatively, this unspecified free rotation will be determined by experiments. Thus, in the slippage-free conditions, the trajectory of single abrasive grit, simplified here as a point P, is shown in Figure 5.2.

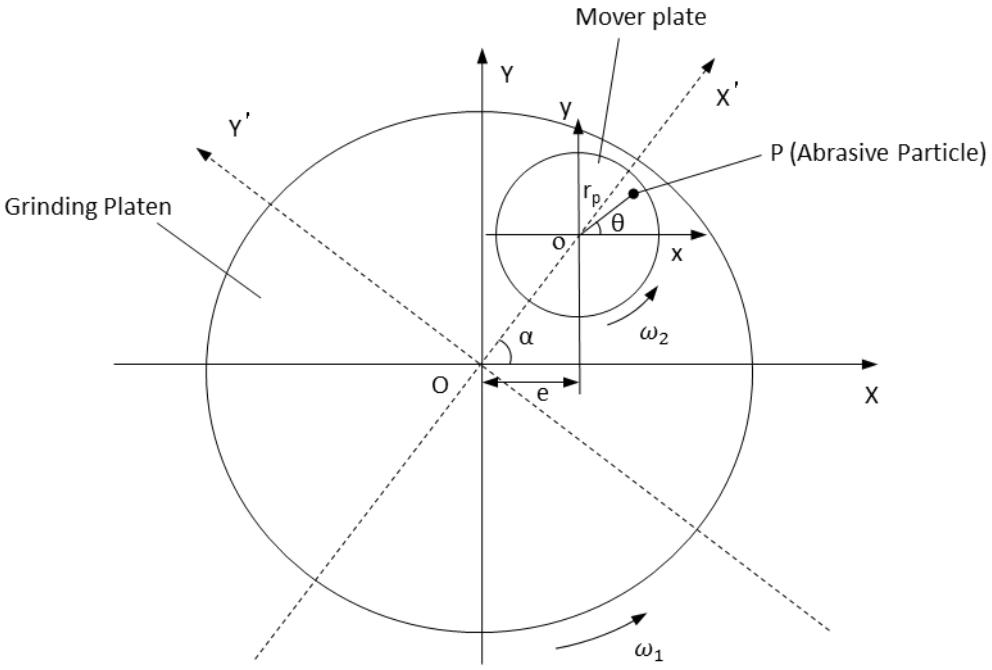


Figure 5.2 Schematic illustration of kinematic system for plane grinding process

Figure 5.2 presents a transient moment in grinding process. Coordinate XOY is a fixed global coordinate and the origin O locates at the centre of grinding platen, while coordinate xoy is a moving local coordinate, the origin of which locates at the centre of mover plate, and it rotates with the mover plate simultaneously. There is an eccentricity e between the grinding platen centre and the mover plate centre. Abrasive P locates at a distance r_p from the centre of the grinding platen. The rotational speed of

the grinding platen and the mover plate are ω_1 and ω_2 respectively. θ is the angle between OP and OX, while α is the angle between ox and OX. They can be described as follows:

$$\begin{cases} \theta = \theta_0 + \omega_1 t \\ \alpha = \alpha_0 + \omega_2 t \end{cases} \tag{5.1}$$

where θ_0 and α_0 are the initial values of angle θ and α. The position of abrasive in coordinate XOY in an arbitrary transient can be derived as:

$$\begin{cases} x_p = r_p \cos\theta \\ y_p = r_p \sin\theta \end{cases} \tag{5.2}$$

It can be further derived by combining Equation (5.1):

$$\begin{cases} x_p = r_p \cos(\theta_0 + \omega_1 t) \\ y_p = r_p \sin(\theta_0 + \omega_1 t) \end{cases} \tag{5.3}$$

From the geometric relationship, the trajectory of abrasive P in the moving coordinate xoy can be given as follows:

$$\begin{cases} x_p' = \cos\big((\theta_0 - \alpha_0) + (\omega_1 - \omega_2)t\big) - e\cos(\alpha_0 + \omega_2 t) \\ y_p' = \sin\big((\theta_0 - \alpha_0) + (\omega_1 - \omega_2)t\big) + e\sin(\alpha_0 + \omega_2 t) \end{cases} \tag{5.4}$$

As Equation (5.4) is the condition without the slippage, in order to take this factor into consideration, the slippage is captured by a wireless sensing system (details in section 3.6), and applied that into Equation (5.4) The equation will then be:

$$\begin{cases} x_p' = r_p\cos\big((\theta_0 - \alpha_0) + (\omega_1 - \omega_2)t + \varphi(t)\big) - e\cos(\alpha_0 + \omega_2 t) \\ y_p' = r_p\sin\big((\theta_0 - \alpha_0) + (\omega_1 - \omega_2)t + \varphi(t)\big) + e\sin(\alpha_0 + \omega_2 t) \end{cases} \tag{5.5}$$

Where $\varphi(t)$ is the slippage angle varies with time.

5.2 3D material removal and surface updating algorithm

Upon have the 2D trajectories of gits, 3D surface profile can be developed based on these trajectories. In this section, a Z-map based method is used to simulate the profile workpiece surface. It is a spatial-decomposition or spatial-partitioning approach, which subdivides the space with grids. In Z-map approach, the heights at meshing points are stored in two-dimensional arrays. Thus, using Z-map method the three-dimensional workpiece surface is decomposed into a two-dimensional mesh shown in Figure 5.3.

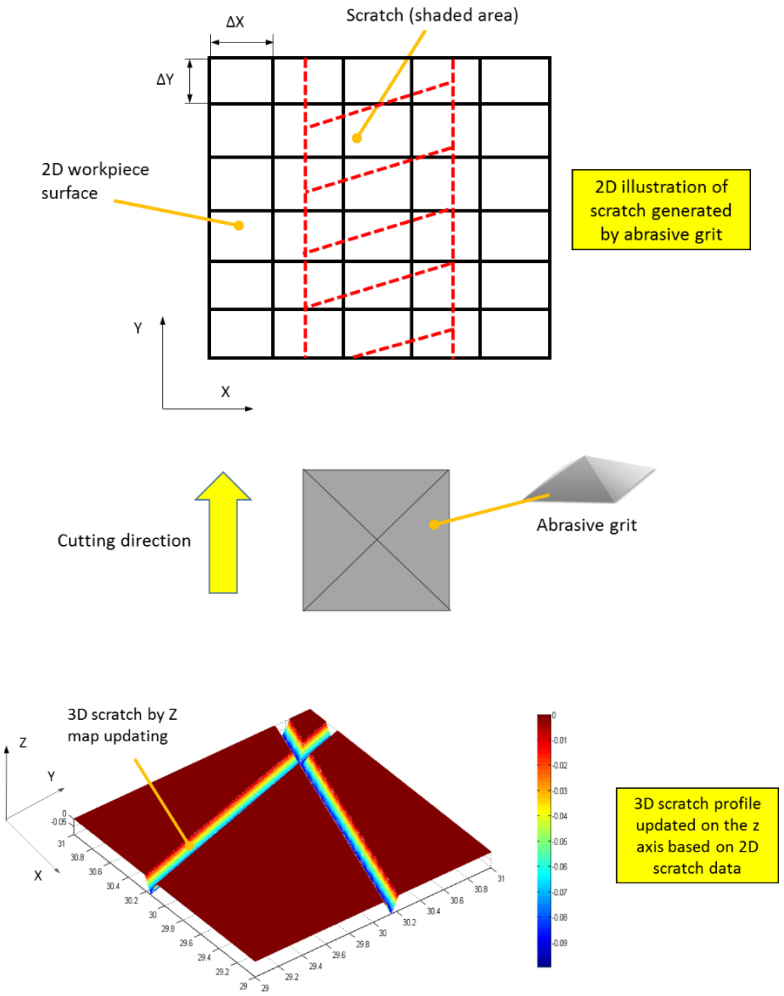
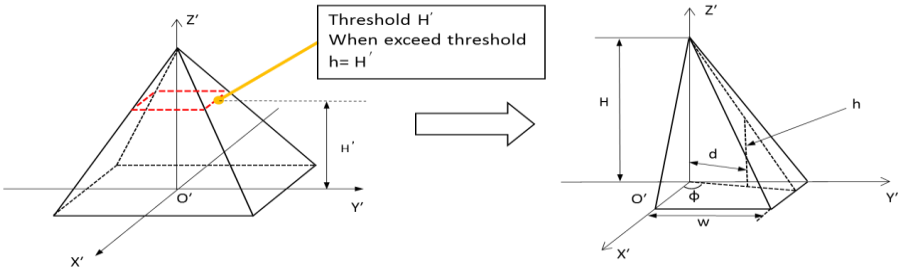


Figure 5.3 Illustration of how Z-map approach updating the surface profile

When conducting the simulation, the simulated abrasive grits are cutting into the workpiece surface and producing scratches based on their macro geometry and cutting depth. The model will update the height Z at each point being cut during the whole process to achieve the resultant workpiece surface texture. ΔX and ΔY are the mesh sizes in X and Y direction respectively, which can influence the accuracy and computation time of simulation.

5.2.1 Abrasive grit model

Square frustum was selected as the abrasive geometry to develop the model, since this type of symmetric engineered grits has been proven to can give good finishing performance and introduce less damage as discussed in Chapters 4. In order to update the surface height cut by one abrasive grit, it is necessary to describe the height of grit at each point across the grit surface parametrically. The parametric form of square frustum is based on the parametric form of a square pyramid, a threshold was set on the top of the square pyramid (in Matlab) to convert it into the square frustum (Figure 5.4 a). The square pyramid grit is located in a local coordinate where the origin is the centre of bottom surface. As square pyramid is axially symmetrical, it can be further simplified as Figure 5.4 (b) for derivation of its parametric form.



(a) (b)

Figure 5.4 (a) geometry of square pyramid grit (b) parametrically described grit

Two parameters, φ and d are employed to describe the position of points in X′O′Y′ plane, where h is the height of points on the surface of pyramid grit. Height of any point on the grit surface can be given as:

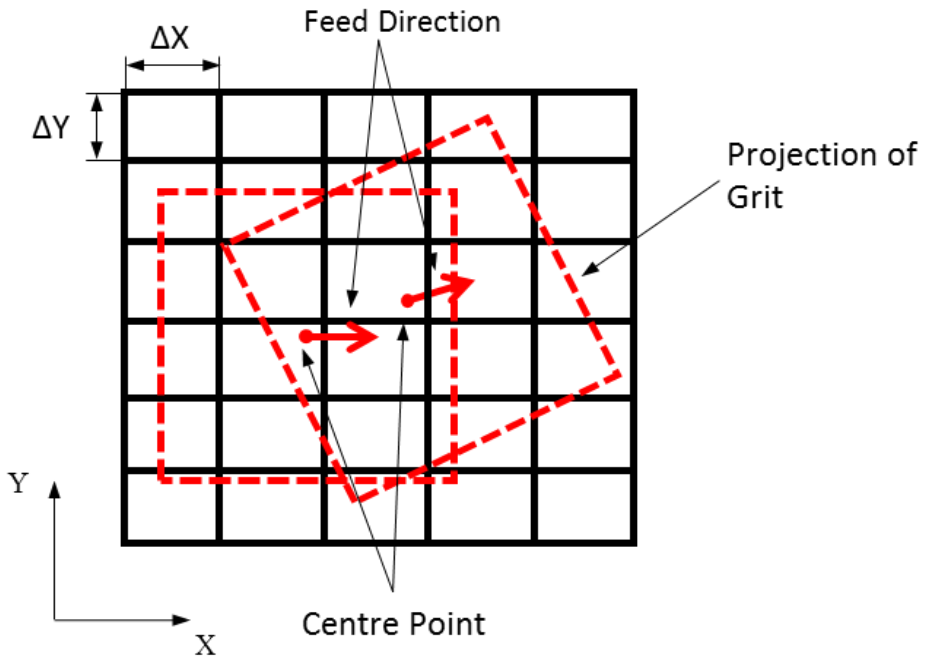
$$h = \begin{cases} H\left(1 - \frac{|X\prime|}{w}\right) & \varphi \in [0^o, 45^o] \\ H\left(1 - \frac{|Y\prime|}{w}\right) & \varphi \in (45^o, 90^o] \end{cases} \tag{5.6}$$

It is noticeable that when pyramid height H and half of the bottom length w is known, height of any point on the girt surface is determined by angle φ and X′ or Y′ coordinates. Equation (5.6) can be used for other axially symmetrical part by taking the absolute values of X′ and Y′, and transforming angle φ by angle transformation formulas.

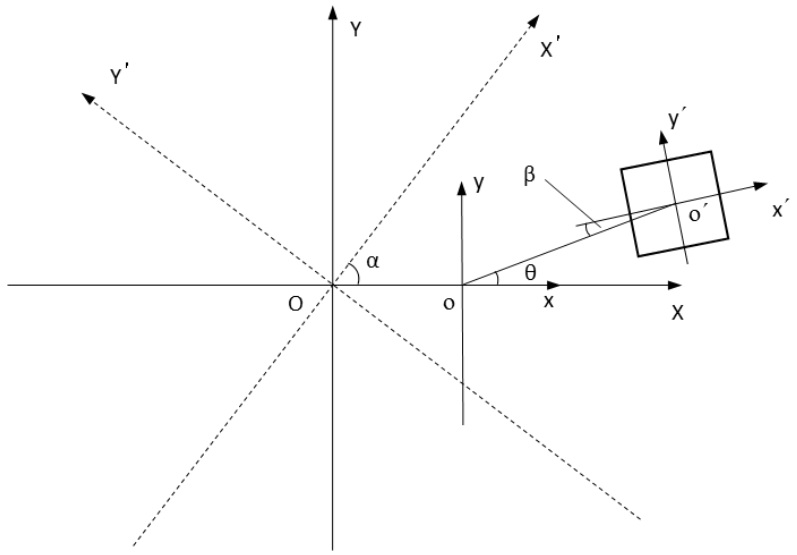
5.2.2 Grit motion discretization

In the plane grinding process, the rotatory motions of polishing platen and mover plate will introduce a shift in orientation of grits relative to workpiece surface. Figure 5.5 (a) shows two transients of the square pyramid grit normal to the workpiece surface. To quantify this rotation relative to workpiece surface, one global and two local coordinates are employed as discussed previously (Figure 5.5 b). It assumes that the initial orientation of coordinates X′O′Y′ and x′o′y′ are parallel to xoy; therefore β is equal to θ_0 and α_0 is equal to 0. This assumption does not affect the profile generated on the workpiece, but facilitate the analysis. In this case, the orientation of coordinate x′o′y′ relative to X′O′Y′, which demonstrates the shift in orientation (counter clockwise) of the grit relative to the workpiece move coordinate, can be given as follow:

$$\gamma = (\omega_1 - \omega_2)t - \theta_0 \tag{5.7}$$



(a)



(b)

Figure 5.5 (a) Transient projections of a single grit (b) transient orientation of a single grit

5.2.3 Material removal algorithm

The key point in material removal simulation is to update the heights stored in two-dimensional array of workpiece surface. As the trajectory of the grit on the workpiece surface has been derived, the position of grit on the workpiece surface at any time can be determined as well. Figure 5.6 shows the projection view of the active part of girt cut into the material on the workpiece surface.

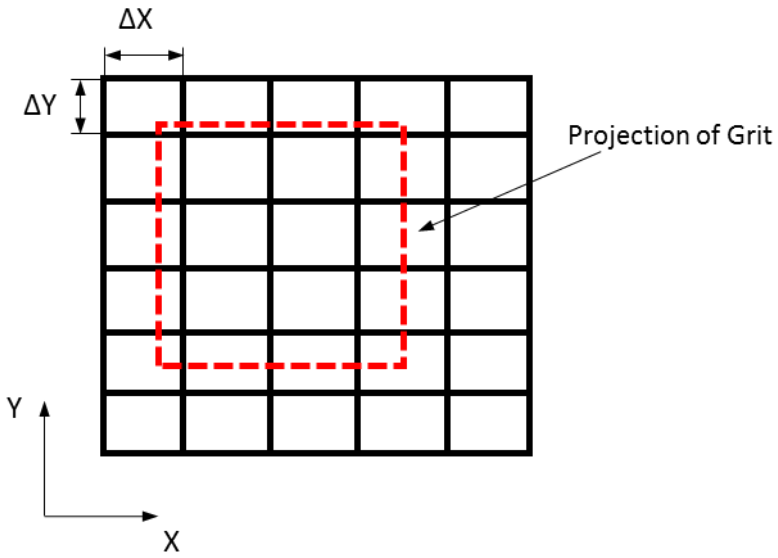


Figure 5.6 Projection view of grit on the workpiece surface

The orientation and position of a grit at the certain transient in workpiece coordinate can be determined by Equation (5.5) and (5.7). Assuming all the meshing points on the workpiece surface within the grit projection has heights of Z_w. According to Equation (5.6), the heights h of cutting points at corresponding positions on the grit surface can be calculated. The surface updating algorithm gives as:

$$Z_w < -h,\ \ Z_w = Z_w$$
$$Z_w \gg -h,\ Z_w = -h \qquad (5.8)$$

After updating for one transient it goes for next transient and follows the same material removal algorithm until the end of the machining process. For multi grits case, same algorithm is employed, the only difference is to set multi positions of grits and perform the simulation one by one. The procedures of the geometrical simulation are summarized in Figure 5.7.

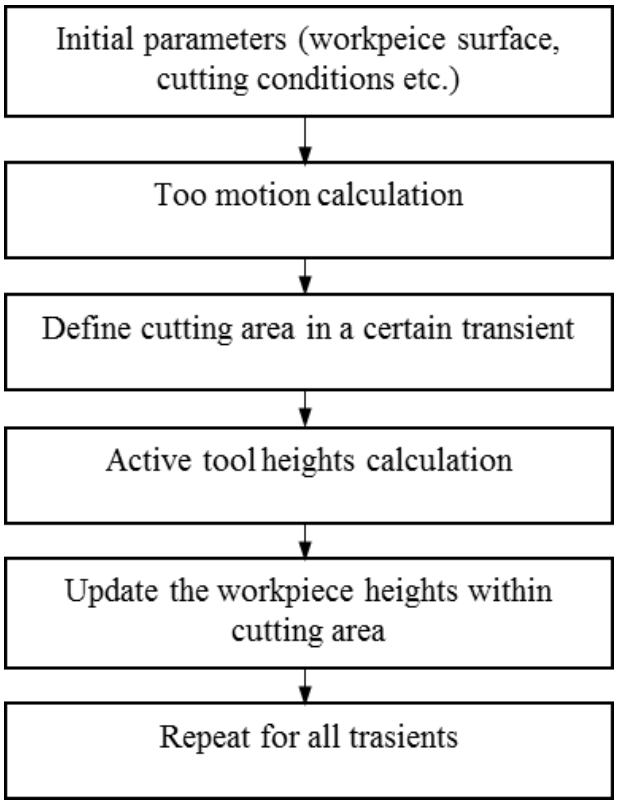


Figure 5.7 Algorithm for 3D updating the surface texture

5.3 Validation and discussion

As described in section 3.8, the surface roughness of simulated surface will be validated by inverted test. The working parameters used were: head speed=100rpm; disc speed=200rpm; Force= 20N, and the PLA abrasive pad used have 25 square frustum grits in total, the dimensional characteristics are described in detail in section 3.8.

The slippage between workpiece material and abrasive pad was captured by PST-360 rotational sensor and transmitted wirelessly between two

Xbee modules. The measured slippage data under the operation conditions listed above is shown in Figure 5.8, which represents the time dependant term $\varphi(t)$ in Equation (5.5), and it was introduced to the grits trajectories as shown in Equation (5.5) for the simulation. Once the scratched surface were generated, it has been scanned using an Alicona on three locations radially across workpiece disc with equal area as simulated surface to allow the evaluation of surface roughness. The scanned surface roughness have been compared with the geometrically simulated surface roughness (Done by Matlab) for the validation.

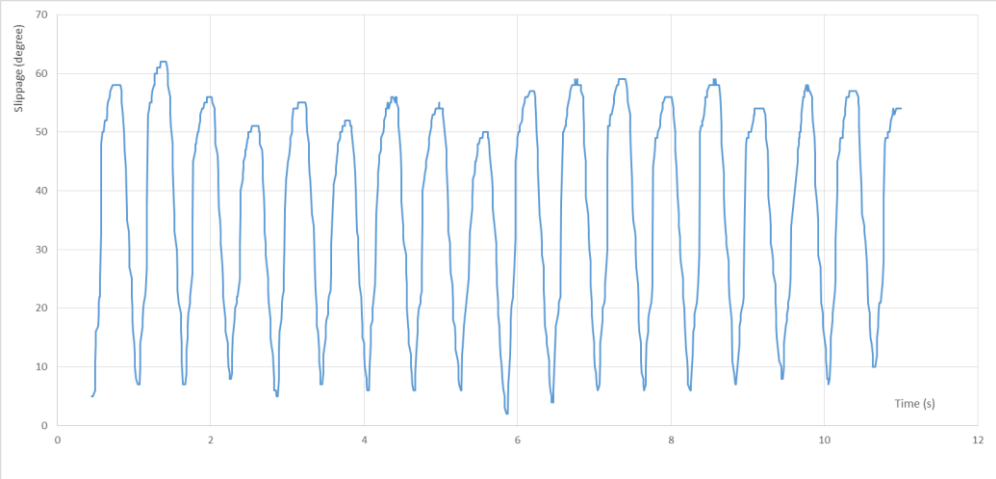


Figure 5.8 Data of measured slippage $\varphi(t)$ in Equation (5.5)

To validate the geometrical model for surface roughness prediction, measurements were taken on three spots radially (20mm, 40mm, 60mm away from the centre) across the stainless steel disc, the simulation was also conducted on these three spots. The experimental and simulated surface topography are compared in Figure 5.9 for each spot respectively. The matlab code used to simulate the surface profile is listed in the appendices. It can be observed, the experimentally measured and simulated surface topography are qualitatively similar. It is noteworthy that, although the experimental and simulated surface looks similar, experimental surfaces tend to have more variations on heights than that of simulated ones. It is possibly due to the measurement noise, micro cutting edges in experiments or material flow in real test conditions.

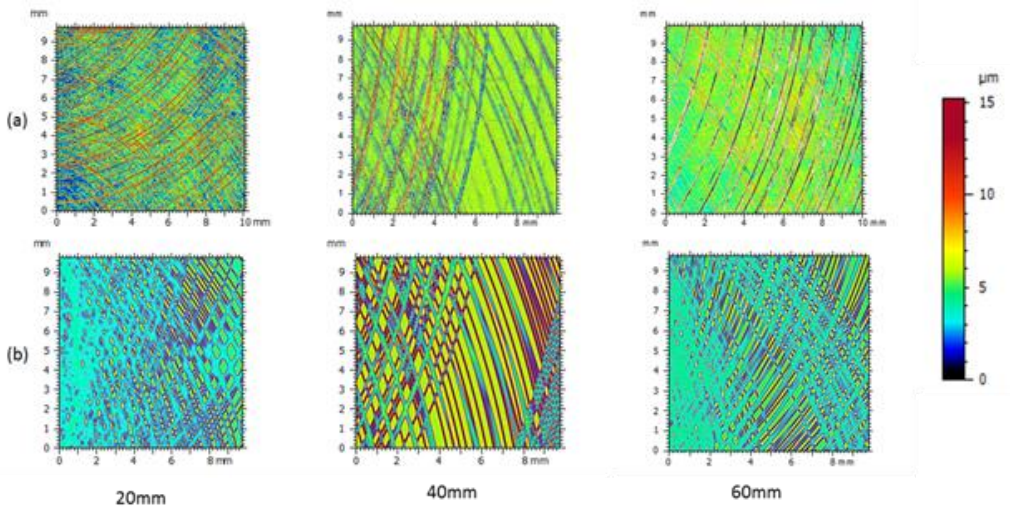
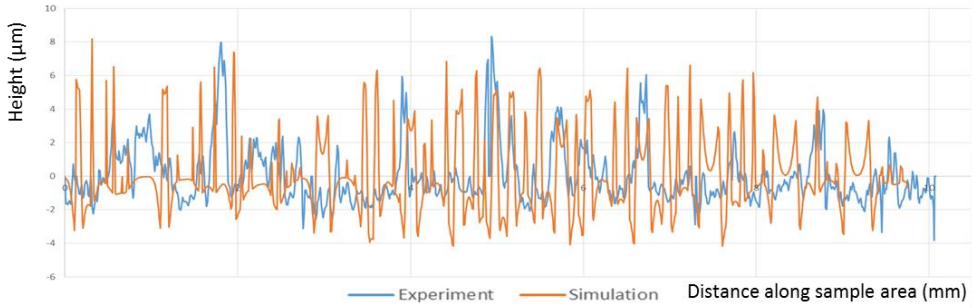


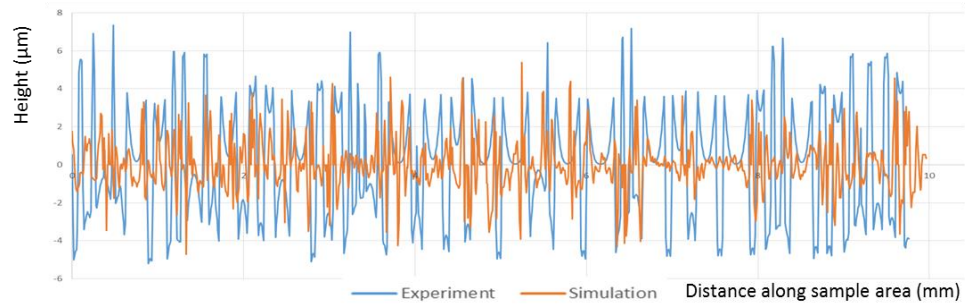
Figure 5.9 Workpiece surface topography for three spots (20mm, 40mm, 60 radially away from the disc centre): (a) experiment (b) simulation

Figure 5.10 shows the experimental and simulated profiles taken along the horizontal axis for each of the three spots. It can be seen that the simulated surface produced heights are very similar to the experimental results, while the simulated heights appear to be somehow greater than the experimental heights.

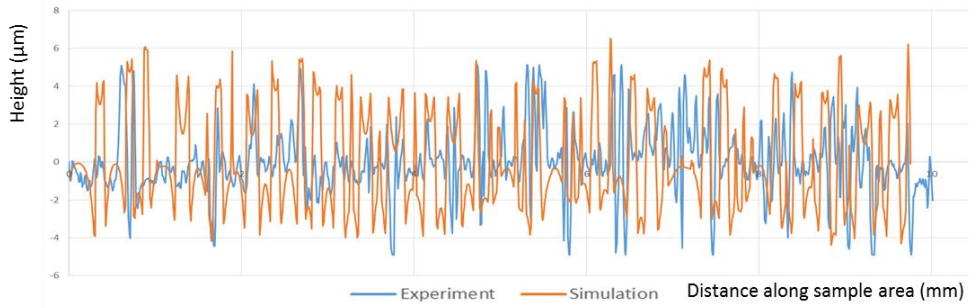
To quantitatively validate the predicted surface roughness results, Figure 5.11 shows the arithmetic mean surface roughness Sa all over the sample area for three different spots. For each spot, the experimentally measured surface roughness are plotted along with the corresponding simulated surface roughness. The results shows a good agreement between experiment and simulation, the differences between the measured and predicted surface roughness are 15.1%, 12.1% and 13.7% for the three spots respectively. The simulation results are slightly higher than the experimental results. This can be explained by the polycrystalline structure of diamond grits, which provide more micro cutting edges that assist the finishing performance rather than the solid geometry in simulation.



(a)



(b)



(c)

Figure 5.10 Cross section profile of experimental and simulated surfaces: (a) 20mm (b) 40mm (c) 60mm radially away from the centre

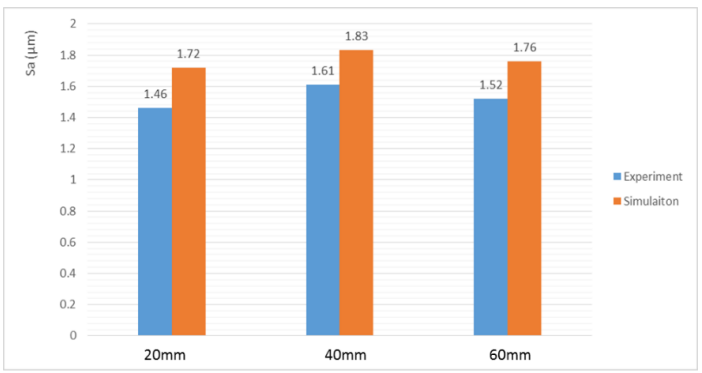


Figure 5.11 Predicted and experimental surface roughness

5.4 Conclusions and remarks

This chapter includes the modelling approach to predict the workpiece surface roughness generated by PLA abrasive pad with square frustum abrasive grits, and results of validation test. A geometrical model has been developed to predict the micro-geometry generated by novel micro arrays with regular abrasives (square frustum) under real contact condition (slippage). A grinding experiment under specific operation conditions was carried out to validate the surface roughness prediction. The slippage between workpiece material and abrasives were captured by rotary sensor, and introduced to the model. A good agreement between simulation and experimental results was observed, the average difference of surface roughness Sa for three measured spots is 13.6%.

This geometrical model has developed a benchmark approach for simulating surface texture under load controlled plane grinding process by employing engineered abrasive pad. The grit geometry can be extended to any other defined shapes which can be described parametrically. As a result, it can be used as an optimization method combined with experimental approach to optimize the design parameters for engineered abrasive pad under particular working conditions, providing preliminary evaluation for both academic and industrial applications in future work.

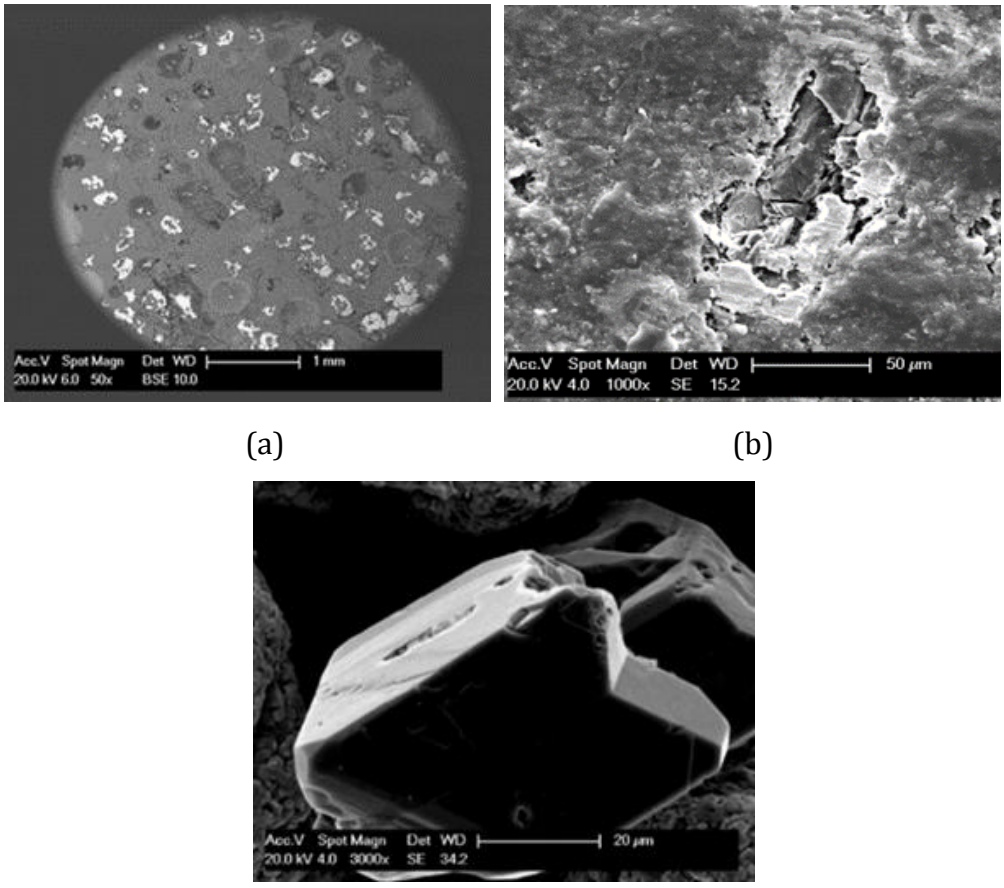
Chapter 6

Evaluation of influence of planar contact area on the grinding performance

In the Chapter 4, the influence of grit geometry on the grinding performance has been studied, and it revealed that planar contact area is also an important factor needs to be taken into consideration for design of engineered grinding pad. This chapter aims at conducting inverted grinding test on one conventional abrasive pad and two engineered abrasive pad (square frustum grits) with different grit size (different planar contact area) to evaluate their influence on grinding performance in load controlled plane grinding operation. The conventional abrasive pad used for this chapter is MD-Piano 220 (FEPA D68) instead of MD-Piano 80 (FEPA D252). The reason for this is MD-Piano 220 is better in terms of maintaining its planar contact area (number of exposed grits) through the whole process, leading to a more solid evaluation on the planar contact area. Although both MD-Piano 220 and 80 pads are multilayered diamond pad, MD 80 pad is more like monolayered pad due to its largest grit size in MD series. Therefore, MD 220 pad is selected for its continuous regeneration of exposed grits to maintain the required planar contact area, and the two engineered abrasive pads with square frustum grits was designed as an emulation of MD 220 pad (details in section 3.4). In addition to the testing procedures conducted in the Chapter 4, mirco-hardness and subsurface damage also have been evaluated for a further understanding of the process.

6.1 Characterization of abrasive grits

As described in section 3.4, the two new engineered abrasive pad is the approximate emulation of Struers MD-Piano 220 abrasive pad, where the grit side length is reduced from 200µm to 40µm and 50µm. Similar to MD-Piano 80 pad used in Chapter 4, it is a tinned metal sheet coated with diamonds in a resin binder, used for the plane grinding of materials in the hardness range 150-2000 HV. The manufacturing methods employed for the production of the Piano 220 are typical to the industry and result in stochastic grit size, shape, orientation, spacing and depth within the resin binder. Characterization of MD-Piano 220 grits are shown in Figure 6.1.

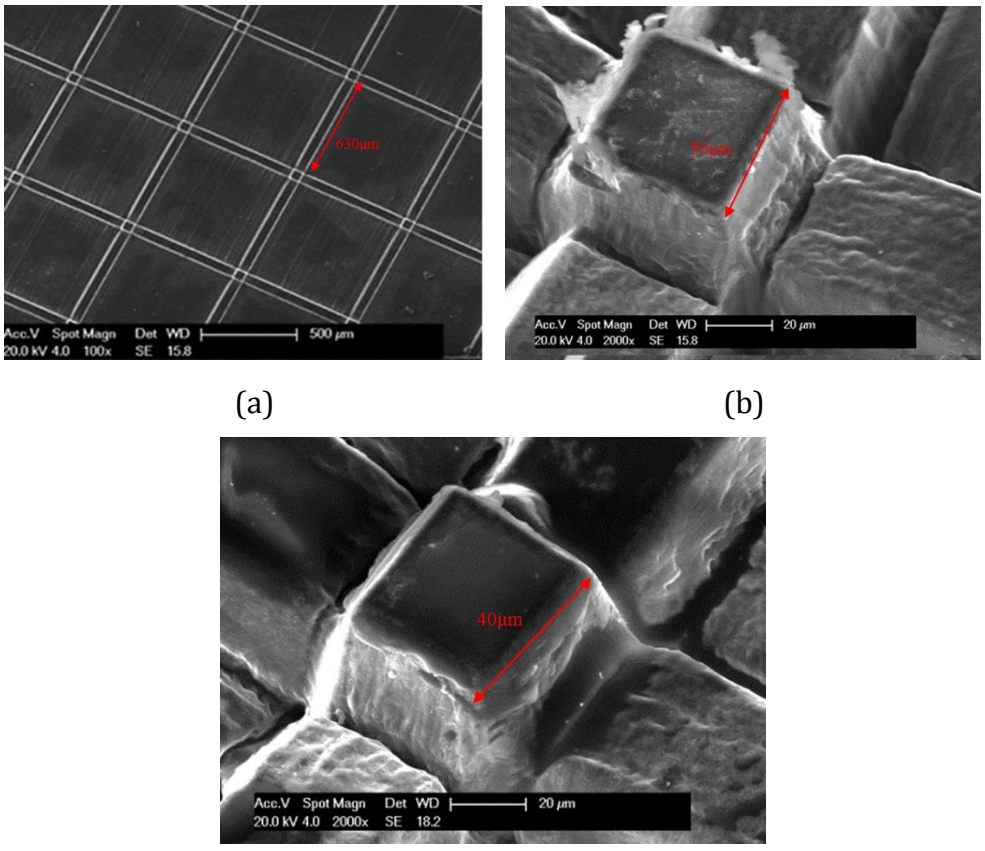


(a) (b)

(c)

Figure 6.1 SEM images (before grinding) of (a) BSE of MD-Piano 220 abrasive pellet (b) half buried single grit (c) uncovered MD-Piano 220 grit

Figure 6.2 shows that the spacing of the grits is random and that the grits are not exposed to the workpiece surface until the resin submerging them is removed; as in 6.2 (b). 6.2 (c) shows the irregular nature of the geometry of the abrasive grit itself, allowing the grit a high number of effective cutting directions. However, the performance of this grit will be highly variable depending on the orientation of the grit relative to the direction of relative motion between the grit and the workpiece and highlights the variability that conventional abrasive tool provides to the users.



(a) (b)

(c)

Figure 6.2 SEM images of new design of PLA micro-arrays: (a) Micro-array structure (b) 50x50µm grit (c) 40x40µm grit

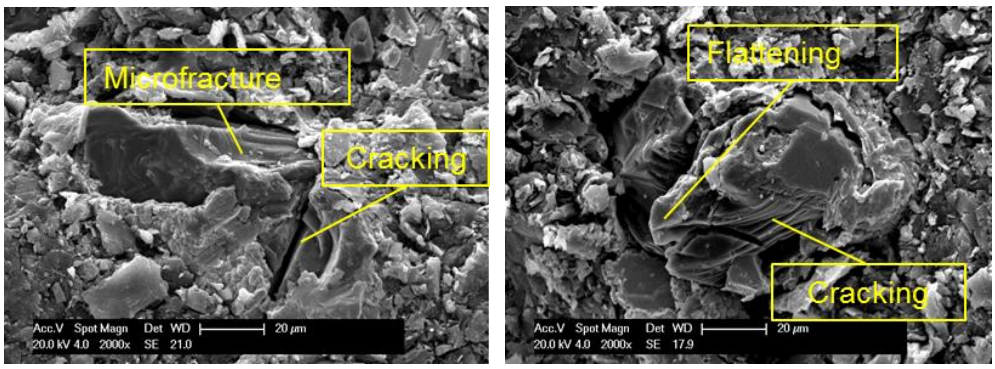
The PLA micro-arrays to be tested have been produced on an EWAG Laserline picosecond laser that allowed an assessment to be carried out on the generation of such abrasive arrays on a commercial laser system. Proprietary technology for the laser generation of abrasive surfaces was used under optimised parameters determined from previous work

(details in section 3.4) in order to generate micro-arrays in a film of polycrystalline CVD diamond. As described in section 3.4, each hexagonal film has dimensions of 24x20.7mm and contains 840 grits, uniformly spaced from adjacent grits in the array by 630μm, as shown in 6.2 (a). Each of the grits is defined as a square frustum, which has previously been found to result in superior surface finish as compared to asymmetric abrasive grits due to having a better utilization of cutting edges for a longer duration of the machining operation in Chapter 4. With regards to the dimensions of the square frustums, there are two separate designs. The first design has a square frustum with a side length of 50μm, and can be seen in Figure 6.2 (b). The second design, as shown in Figure 6.2 (c), has a smaller grit size of 40μm and will allow investigation of the effect of different planar contact area of the abrasive surface on the overall performance in plane grinding process. Compared to these two designs, the MD 220 pad has the lowest planar contact area due to it partially exposed grits and irregular protrusion heights, however, it is very difficult to determine the planar contact area directly from grit size, the further study on this will be covered in Chapter 7.

6.2 Tool wear mechanism

The effects of wear on the abrasive tool surfaces were investigated through SEM imaging, shown in Figure 6.3. As conventional grits have random geometry, the stress distribution through the grit structure is non-uniform and high contact forces between the grit and the workpiece can lead to micro-fracture, typically at the grit tips and edges where the stress concentration is high. Clear evidence of this can be seen in Figure 6.3 (a). The fracture of conventional grits leads to an increase in the number of active cutting edges during the abrasion process, thereby limiting control

over the surface generated. There is also evidence of cracking of the grit structure in a plane perpendicular to the fracture plane. In 6.3 (a), it can be observed that the grit tip has become flattened, due to repeated contact with asperities. Flattening reduces the effectiveness of the grit throughout the abrasion process as the cutting edge angles become more obtuse; thereby reducing their ability to apply concentrated force (high stresses) to the workpiece and cut the surface. In addition, no significant material build up was observed on the grit surfaces, indicating that the conventional abrasive surface has good chip flow in this application.

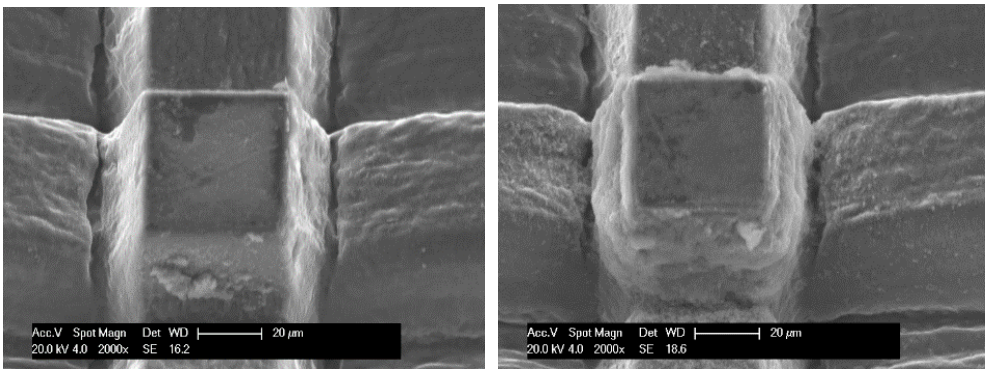


(a) (b)

Figure 6.3 SEM images of wear mechanism of conventional abrasive grits (MD 220) (a) microfracture and cracking (b) flattening and cracking

The PLA micro-arrays demonstrated no evidence of wear sustained during the grinding period. As can be observed in Figure 6.4, the edges of the PLA cutting elements are intact, with no evident fractures, cracking or flattening. This is likely due to the ordered geometry reducing the number of stress concentration sites and also due to the supreme erosion resistance of CVD diamond film. According to the relative erosion resistance of CVD diamond and other materials, CVD diamond has been shown to suffer less relative volume loss than conventional polycrystalline high-pressure sintered diamond [121]. This is due to the CVD diamond manufacturing process creating a highly dense structure, free from voids or structural defects. No workpiece material build up could be observed

on the PLA arrays (Figure 6.4), demonstrating that they have effective chip flow paths in this geometric configuration.

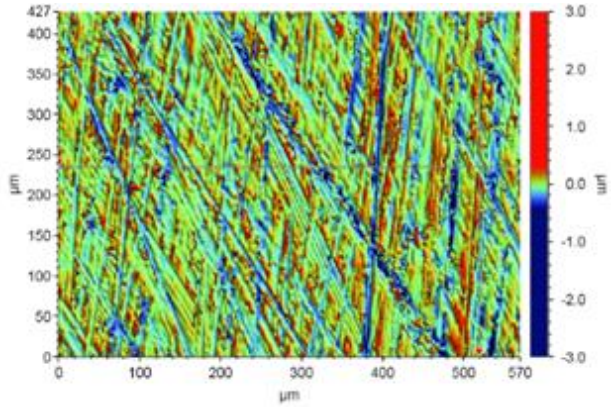


(a) (b)

Figure 6.4 SEM images of PLA grits after 20 minutes of grinding (a) 50x50µm grit (b) 40x40µm grit

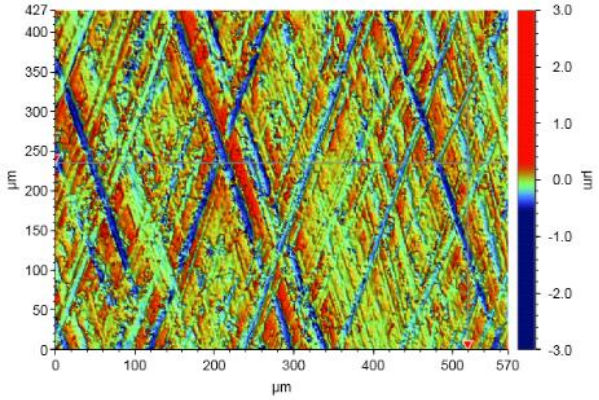
6.3 Evaluation of workpiece surface topography and material removal rate

As discussed in section 6.1, conventional abrasive pad (MD 220) has the lower planar contact area among the three pads, while 50x50µm pad has the highest planar contact area among the three. In order to ease the understanding for the following analysis on planar contact area, low, high and medium will be used referring to planar contact area of Piano 220, 40x40µm and 50x50µm pad in the brackets when necessary. Surface topography images of each of the machined surfaces after the 20 minute grinding period are shown in Figure 6.5. The surface roughness generated 40x40µm (medium) and 50x50µm (high) square frustum pads are 0.114µm and 0.119µm respectively, which are better than that of conventional abrasive pad (low) (0.143). The difference between two engineered abrasive pads is not very significant (0.005µm), while it is much greater when compared with conventional abrasive pad (0.029µm, 0.024µm).



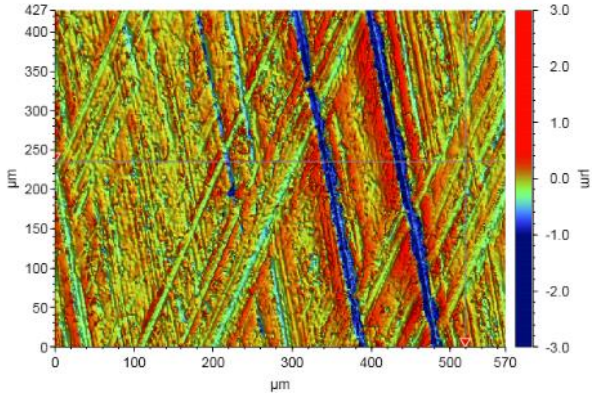
Sa=0.114µm

(a)



Sa=0.119µm

(b)



Sa=0.143µm

(c)

Figure 6.5 Surface topography of workpiece surface after 20 minutes of grinding by (a) PLA 40x40µm (medium) (b) PLA 50x50µm (high) (c) Piano 220 (low)

This revealed that machined surface roughness is more sensitive to grit geometry (number of cutting edges, sharpness etc.) rather than planar contact area. Similar to results in Chapter 4, it can be observed that the engineered abrasive pad show greater uniformity in terms of surface topography due to the defined geometry of the tool, with a relatively small variation of scratch depth generated on the workpiece surface. The conventional abrasive surface generates a more random pattern of scratches and the scratches themselves are less well defined.

The progression of the surface roughness over the 20 minutes grinding period can be observed in Figure 6.6. After 5 minutes, the conventional abrasive pad (low) creates a high surface roughness on the workpiece. This is likely caused by a lack of grits engaging the workpiece surface within the early stages of the machining process, as they remained buried within the resin binder. After the initial period, the surface finish rapidly improves between 5 and 10 minutes as the grit cutting edges engage the surface. Beyond 15 minutes, the surface roughness is getting stable and the final surface roughness is 0.143µm.

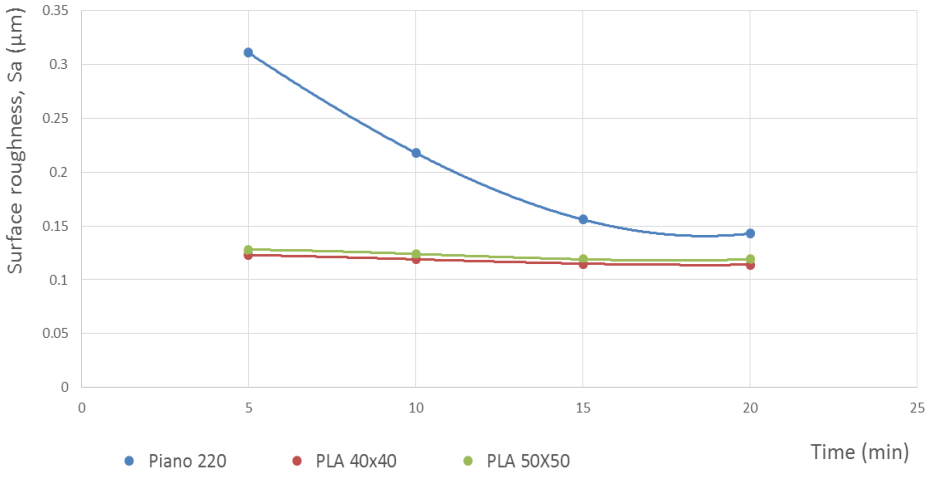


Figure 6.6 Progression of workpiece surface roughness generated by three types of abrasive grits (Piano 220 (low), PLA 40X40 (medium) and PLA 50x50 (high))

Both of the engineered micro arrays (medium and high) achieve a superior surface finish to the conventional abrasive pad (low) right after 5 minutes. This is due to the micro arrays having active cutting edges from the beginning that they operate at maximum efficiency from the start of the grinding process. Throughout the 20 minutes period, the PLA micro-arrays exhibit almost linear and minor incremental improvements in surface finish. This demonstrates that the absence of wear on the PLA micro-arrays (as discussed in chapter 4) allows consistent performance at, or close to the as manufactured-performance. Therefore, as the progression of the surface roughness is highly controllable, future tooling can be designed and utilized to achieve a desired surface quality through knowledge of the as-manufactured performance and the machining time. This demonstrates the similar fundamental improvement found in Chapter 4 that the PLA micro-arrays afford; controllability of the final workpiece surface quality.

The final surface achieved by the PLA micro-arrays (medium and high) is slightly better than the conventional abrasive (low) machined surface; the 50x50μm (high) final surface finish is 0.119μm and the 40x40μm (medium) final surface finish is 0.114μm. It is clear that the 40x40μm (medium) array is superior to the 50x50μm (high) design in terms of surface finish, which is likely to suggest the reduced planar contact area (smaller grit size) can improve the surface roughens; however, as discussed previously, conventional abrasive pad (low) has the smallest total planar contact area among the three, while it produced the highest final surface roughness (0.143μm). As a result, in this case, grit geometry is the dominant factor that influence the finishing performance.

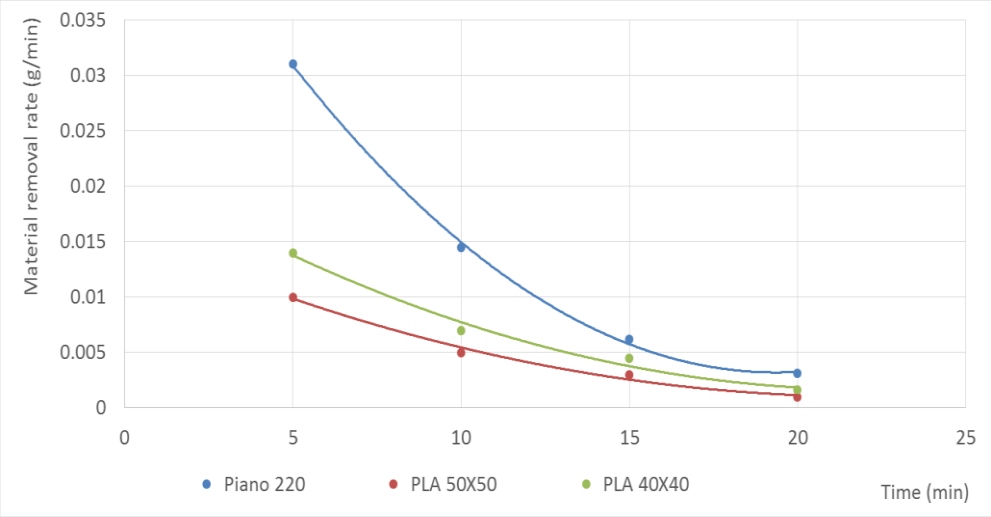


Figure 6.7 Material removal rate of workpiece generated by three types of abrasive grits (Piano 220 (low), PLA 40X40 (medium) and PLA 50x50 (high))

The progression of the material removal rate can be seen in Figure 6.7. It should be noted that in general the material removal follows a similar trend to the surface finish. Once the resin binder has been eroded and the conventional grits are exposed, they can begin to remove material more efficiently. Initially, at 5minutes, the material removal of conventional abrasive pad (0.031g/min) is significantly higher than that of the PLA grits (0.010g/min, 0.014g/min respectively) as the unworn conventional grits have stochastic geometry (as in Figure 6.1 c), and certain grits are likely to have higher angles of attack and sharpness than the square frustum PLA grits. However, after longer exposure to the workpiece surface, the material removal rate quickly reduced. This is partially due to the conventional grits wearing and becoming less effective as discussed in the previous section, however, it is also due to the surface morphology of the workpiece. Initially, the surface had a high amplitude difference between the peaks and the valleys (higher roughness) and so the material was quickly removed by mechanisms such as cutting and ploughing, which are known to occur with conventional grits. However, as the machining progresses, the peaks become flattened down and so the contact area

between the workpiece and the abrasive surface increases, reducing the cutting pressure and therefore less material is removed. The PLA micro-arrays exhibit a very low removal rate initially, whilst achieving a superior surface finish as shown in Figure 6.6. This suggests that rather than removing material from the workpiece surface via cutting and ploughing, the surface is instead being flattened down through a sliding contact mode between the square frustums and the workpiece surface. This trend of low material removal continues throughout the machining process, which is leading to the similar conclusion in Chapter 4 that rather than cutting/ploughing the material, flattening is the dominant material removal mechanism for PLA micro arrays. By comparing the material removal rate in the final stable stage, it showed that 40x40 micro array (medium) has higher material removal rate (0.0016g/min) than that of 50x50 micro array (0.0010g/min) (high), while conventional abrasive pad (low) is much higher (0.0029g/min) than both of them. This gives an indication that reducing the total planar contact area of engineered abrasive pad to a certain extend can improve the performance of material removal. This is likely to be caused by the reduction of the load per unit grit when more grits are present on the abrasive surface, as Gåhlin and Jacobson commented [75]. Furthermore, engineered abrasive pad with same level of total planar contact area is likely to achieve approximately the same or better performance of material removal as conventional abrasive pad. A more detailed study of this will be presented in Chapter 7.

6.4 Evaluation of micro-hardness and subsurface damage

Once the topographical and morphological measurements covered in Chapter 4 are done, subsurface analysis was conducted to further evaluate

the grinding performance. As described in section 3.5, the micro-hardness of the 304 stainless steel workpieces was tested at incremental 5µm depth increments from 20µm below the machined surface (as close to the surface as possible with the Vickers indenter used) to 50µm (towards the bulk material); the results can be seen in Figure 6.8. The bulk material hardness was 172 H_V.

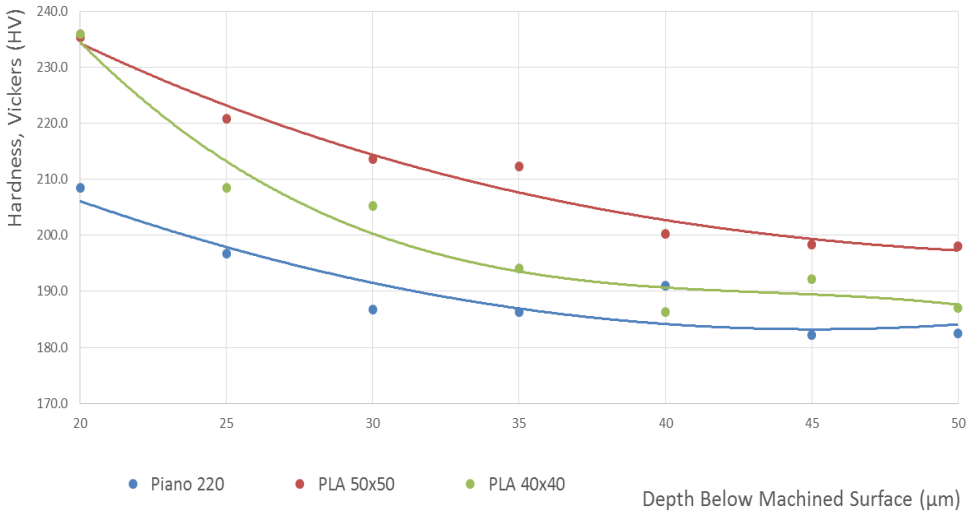
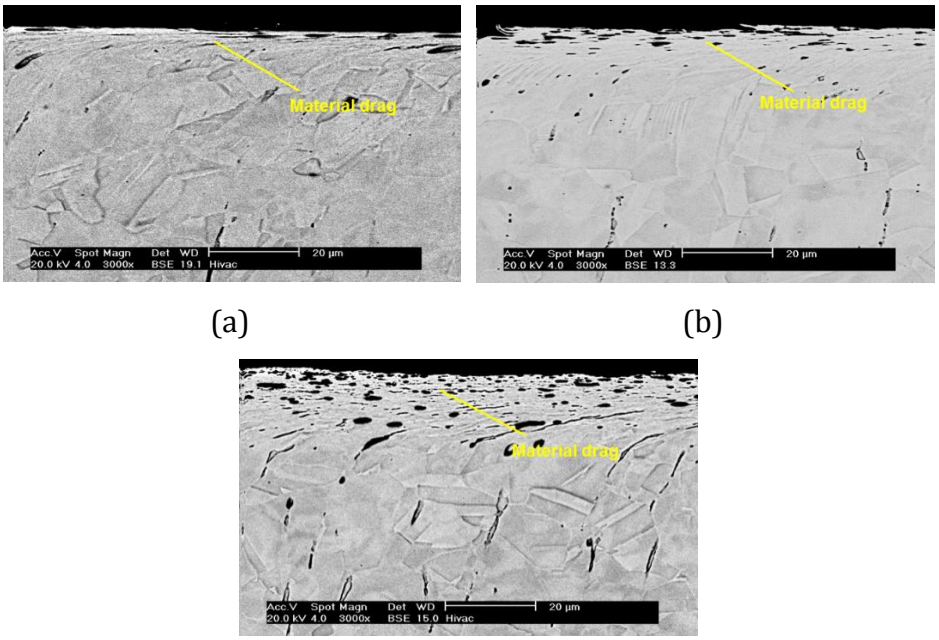


Figure 6.8 Variation of micro-hardness beneath the machined workpiece surface generated by three types of abrasive grits (Piano 220 (low), PLA 40X40(medium) and PLA 50x50(high))

Abrasive machining with the conventional abrasive pad (low) led to a lower hardness through the depth of the cross section of the workpiece, showing that there was less work hardening and therefore lower subsurface damage caused to the workpiece as compared to the PLA arrays. The 40x40µm array (medium) outperformed the 50x50µm (high) as it caused less subsurface damage in general. The conventional abrasive pad shows a steep gradient up to a depth of 35µm below the machined surface, before a reduction in gradient. This point was further into the surface at 40µm for the PLA arrays, suggesting that the PLA arrays of the tested configurations induce subsurface damage further below the machined surface than the conventional abrasive surface.

SEM images of the cross sections of the workpiece discs were taken in

qualitative support of the micro-hardness testing, these can be seen in Figure 6.9. Material drag can be observed near the surface on all of the workpieces, along with grain deformation. Away from the machined surfaces, there is little evidence of grain deformation. The depth that this occurs at is greater in the PLA array machined surfaces at approximately 15µm, compared to the Piano 220 machined surface which shows no deformation beyond 10µm.



(a) (b)

(c)

Figure 6.9 SEM images of workpiece cross sections after 20 Minutes grinding (a) Piano 220 (low) (b) PLA 50x50µm (high) (c) PLA 40x40µm (medium)

Conventional grits typically have good edge definition and sharper cutting edges than the relatively blunt cutting edges of ordered abrasive grits as shown in Figure 6.1 (c), therefore it is more efficient to remove the work-hardened material(higher removal rate). However, although the engineered abrasive grits tends to give better surface finish in a shorter time, it is inferior to the conventional grits in the aspect of removing work-hardened layer. This theory is supported by work undertaken by Yuan et al. who investigated the effects of the cutting edge radius of a cutting tool

on the micro-hardness of the machined surface [122]. It was found that by doubling the cutting edge radii from 0.3μm to 0.6μm (i.e. a less sharp cutting edge); the micro-hardness of the machined surface was increased by 25%. In addition, there is also a correlation between thickness of work-hardened layer and planar contact area. In load controlled plane grinding process, the purpose is to finish the surface and remove the subsurface damage, therefore the similar trends found in material removal rate (Figure 6.7) and micro-hardness (Figure 6.8) can be explained in the same way. The performance of material removal reflected the capability of removing subsurface damage, and by reducing the total planar contact area, the improvement can be observed.

6.5 Conclusions and remarks

In order to evaluate the influence of planar contact area on the performance of plane grinding process, inverted test has been conducted following the identical procedures in Chapter 4 on conventional abrasive pad (MD-Piano 220) and two engineered abrasive pad with different grit size (40x40μm and 50x50μm square frustum grits). The key findings can be summarized as follows:

- The wear mechanisms of the Piano 220 abrasive grits are found to be microfracture, cracking and flattening, however, no sign of aggressive wear can be observed for engineered abrasive grits, indicating that the engineered arrays are significantly more durable.
- Both engineered abrasive pad achieve a better surface finish in a shorter time, due to having immediately active cutting faces. The final surface finish obtained after 20 minutes was superior to the conventional abrasive surface. For engineered abrasive pad, reducing the total planar contact area tends to slightly improve the surface

roughness, however, grit geometry was found to be the dominant factor when compared with conventional abrasive pad.

- Conventional abrasive pad has an overall advantage in material removing due to its shape factor. In addition to this, for engineered abrasive pad, the one with less total planar contact (40x40 PLA) area tends to have a higher material removal rate. This revealed that design of engineered abrasive pad with approximately equivalent total planar area as conventional abrasive pad is likely to have close or better material removal performance.
- The subsurface analysis revealed the similar trend as material removal rate, as the capability of removing subsurface damage is generally reflected by the material removal in load controlled plane grinding process. Therefore, to reduce the subsurface damage, improvement could be done on reducing the total planar contact area of engineered abrasive pad to a certain extend (e.g. equivalent to real planar contact area of conventional abrasive pad).
- Based on the above findings, it can be concluded that the current design of engineered abrasive pad consisted of square frustum grits does not fully emulate the planar contact area of conventional abrasive pad, causing the inferior performance of material removing and higher the subsurface damage compared to conventional abrasive pad. An approach to determine the real planar contact area of conventional abrasives during the wear process is needed for an improved design on material removal (covered in Chapter 7).

Chapter 7

Design improvement of planar contact area for engineered abrasive pad

According to the results in Chapter 6, although the finishing performance is superior for PLA engineered abrasive grits, the amount of material removal did not reach the same level of conventional abrasive pad due to the difference in total planar contact area. In this chapter, research has been conducted to further investigate the role of planar contact area on the removal of ductile material (i.e. 304 stainless steel), in a load controlled plane grinding process. Measurements on the amount of material machined by Piano 220 conventional abrasive pad has been accomplished using linear scratch tests at selected loads and compared with the results achieved in inverted grinding trials. The influence of planar contact area experienced by a defined population of abrasives is evaluated using laser generated abrasive grits of square frustum having controlled, size, protrusion, location and contact area using both scratch tests and inverted grinding tests.

7.1 Determination of planar contact area and specific material removal

Before linear scratch test, inverted grinding tests were conducted for conventional and PLA abrasive pad to quantify the material removal for comparison purpose. The sample abrasive pads adopted are the ones also used in chapter 6: MD-Piano 220 and PLA abrasive pad with square

frustum grits (50x50μm). A load of 30 N is selected and the grinding time is 20 minutes, the setup can be referred to section 3.4.1. This PLA abrasive pad is regarded as Population 1 for later study.

The surface of one hexagonal abrasive element of Piano 220 pad after 20 minutes of operation was then taken to SEM for a full scan. This enables the determination of numbers of visible grits that theoretically engaged with workpiece material. Figure 7.1 shows an example characterization of visible grits on the Piano 220 pad, the total numbers of grits captured are 30, the full characterization is included in appendix 4.

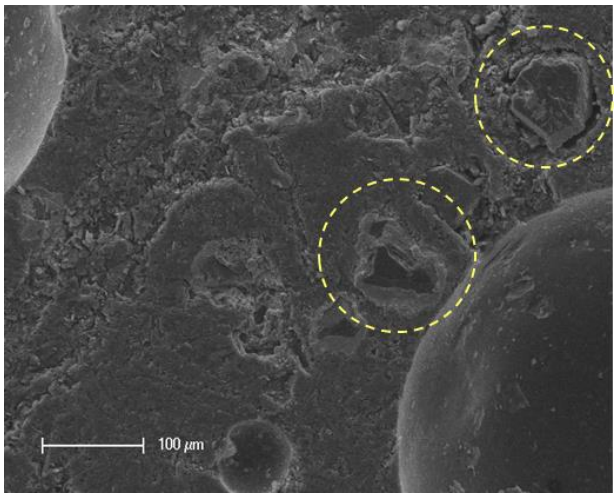


Figure 7.1 Example of visible grits on conventional abrasive pad (MD 220) after 20 minutes of grinding

A combination of SEM imaging and Alicona was also employed to characterize the visible grits size and protrusion height, the surface captures revealed that the exposed abrasives protruded from the bond up to a maximum of approximately 18 um (Figure 7.2). However the exact height of protrusion for every grit was difficult to determine due to the irregular nature surface of the bond matrix. Based on some previous research [16], in order to estimate the theoretical planar contact area, spherical interpolation is used to describe grit shape. Based on the FEPA size of the grit (D68) and size captured by Alicona, the diameter of spherical girts is approximately 60 μm. As a result, the theoretical planar contact area of one visible grit is the area of a circle with 60μm diameter

(without considering the actual exposed size and immersion), and the total planar contact area for 30 grits was calculated to be 87637μm^2.

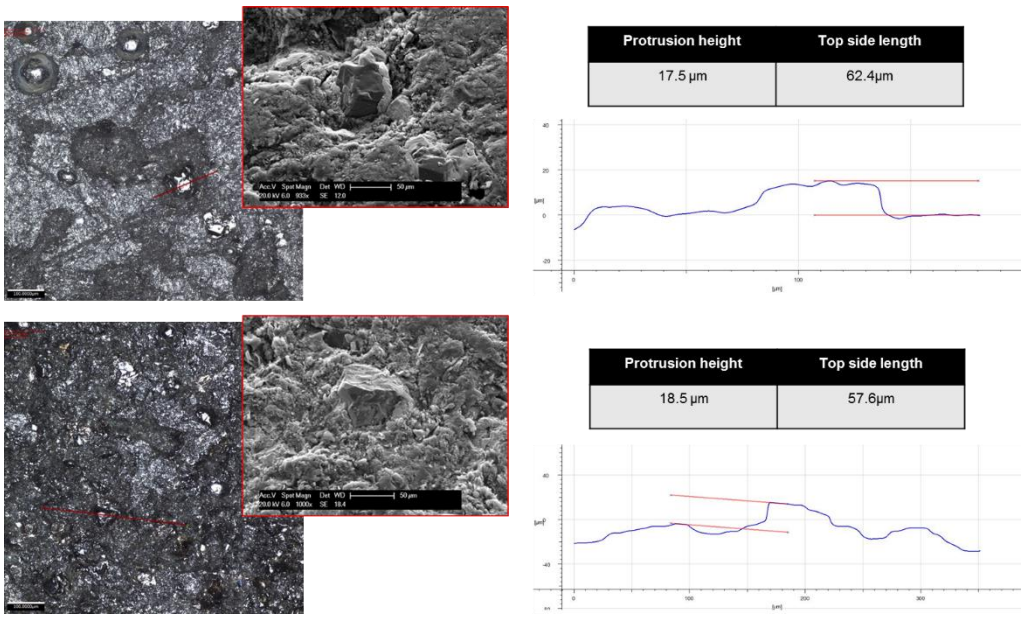


Figure 7.2 Characterization of conventional abrasive grit (MD 220) protrusion and height

As stated in section 2.3.1, the stochastic nature of conventional grinding tool can cause less engagement of grits, only active grits can remove material during the operation. In this case, measurements of the linear scratches produced by the protruding abrasives proved to be a more reliable method to determine the number of abrasives that were actually engaged with workpiece and their depth of engagement at a particular load. By taking the setup and procedures described for linear scratch test in section 3.7, the scratch profiles under three different loads (i.e. 10N,20N,30N) can be obtained by Alicona, an example of scratch captured is shown in Figure 7.3 (data for each scratch is summarized in appendix 5). Spherical interpolation was also used to calculate the estimated planar contact area from each scratch to determine the total planar contact of engaged grits. Table 1 presents a summary of the estimated planar area of the visible grits in a single hexagonal of Piano 220 pad and the determined values of planar contact area based on scratch tests at the three selected loads.

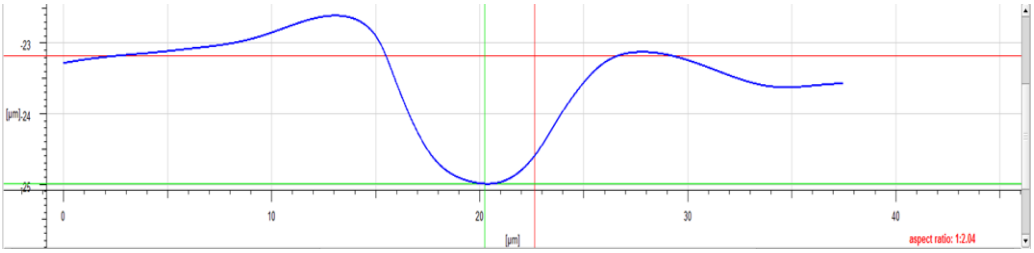


Figure 7.3 Example of scratch profile generated by conventional abrasive pad (MD 220) captured by Alicona

Table 7.1 Planar contact areas of exposed abrasive grits vs. engaged abrasive grits on conventional abrasive pads (MD 220) at 10N, 20N and 30N applied loads

Est. planar area of total exposed abrasives	Summed planar contact area at 10N load	Summed planar contact area at 20N load	Summed planar contact area at 30N load
87637µm^2	2162 µm^2 (2.47% of estimate)	4305µm^2 (4.91% of estimate)	5532µm^2 (6.31% of estimate)

According to table 7.1, the planar contact area obtained from engaged abrasive grits is far less than that of visible grits. Furthermore, from an evaluation of the exposed abrasives from SEM imaging and Alicona captures of the abrasive surface and the measurements of produced scratches, it can be determined from these tests that only a small percentage of the visible abrasives on the surface of the Piano 220 pad engage with the workpiece and affect material removal. Table 7.1 also reveals that the planar contact area of engaged grits, and therefore the number of abrasive grits, increases with an increasing load, more than doubling contact the area between 10N and 20N and an excess of a 28 % increase between 20N and 30N.

In contrast with the progressive engagement of the Piano 220 diamond abrasive grits which increased with applied load, the entire population of the engineered abrasive grits has been designed to engage with the workpiece simultaneously and the number of abrasive grits in contact

with the workpiece does not vary with the applied load. The scratch tests for PLA engineered pad were therefore conducted at one selected load (i.e. 30N) to compare with the inverted grinding tests conducted at the same load condition.

Two laser ablated abrasive pads were designed and generated to have an equivalent total abrasive area of planar contact to a Piano 220 pad at 30N. First is one regarded as population 1, while the second one having an equal abrasive size and layout but incorporating a dimpled relief of 40um diameter and 10 um deep on the abrasive contact face (designated as Population 3). The dimpled relief was designed to allow a more progressive engagement with the workpiece by providing approximately (50%) of the planar area for initial engagement which progressively increased up to the full crater depth. In each of these cases, three aligned square frustum abrasives were generated and designed to have the discrete cutting action of non-overlapped abrasives in the 90^{o} cutting direction and abrasive overlap in the 0^{o} direction. Figure 7.4 shows the SEM images of PLA grits and illustration of grits arrangement.

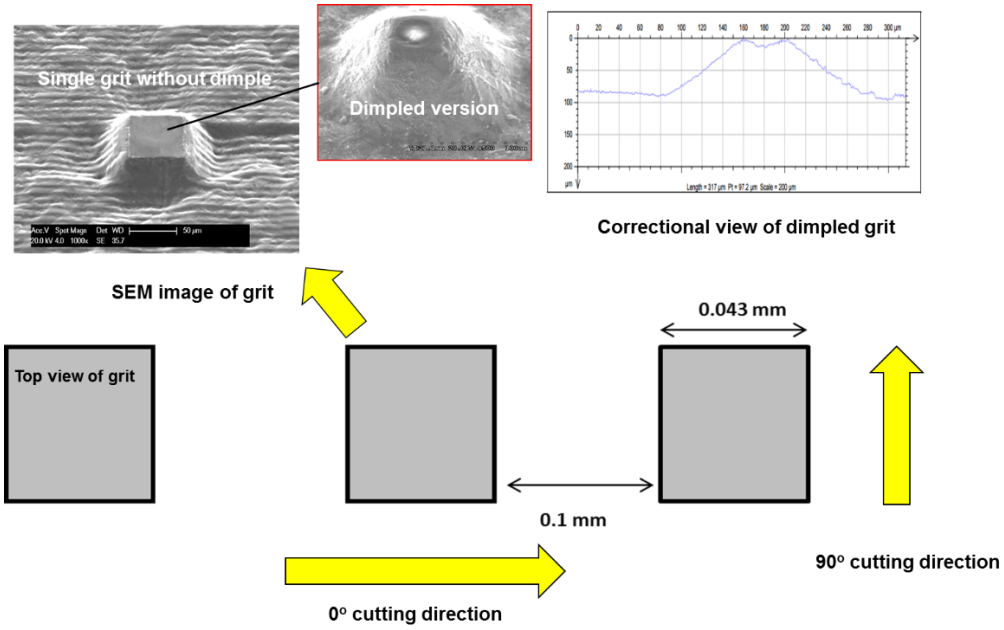


Figure 7.4 Schematic illustration of grit arrangement and cutting directions as well as SEM images of population 2 and 3

7.2 Evaluation of material removal

The conventional Piano 220 pad and the laser generated abrasive surface Population 1 were both run for 20 minutes on 304 stainless steel discs and their mass reduction measured for each grinding test. The results of the material removal rate at steady state are shown in Figure 7.5. These initial results combined with results in chapter 4 and 5 indicate that the engineered abrasives, having an equivalent abrasive size and population to the visible population in a conventional diamond abrasive pad, removed significantly less material.

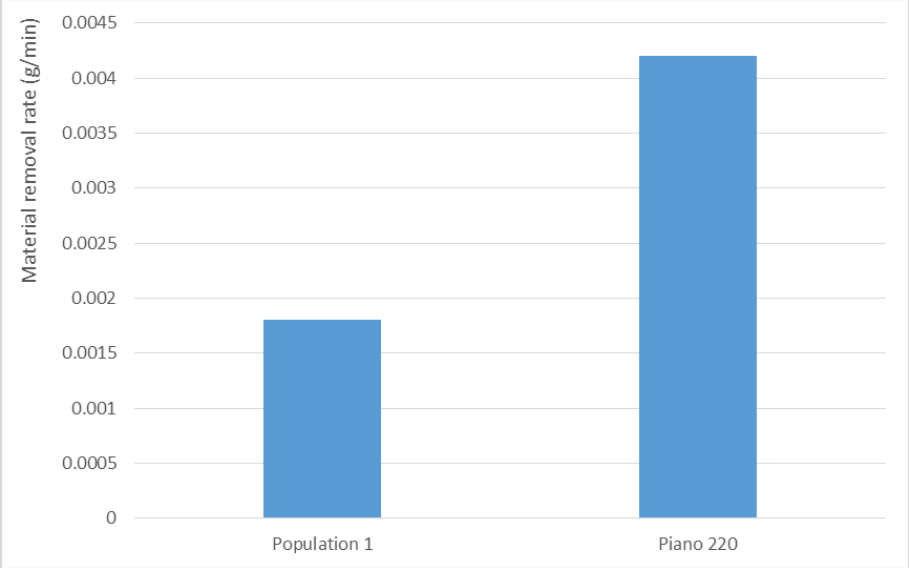


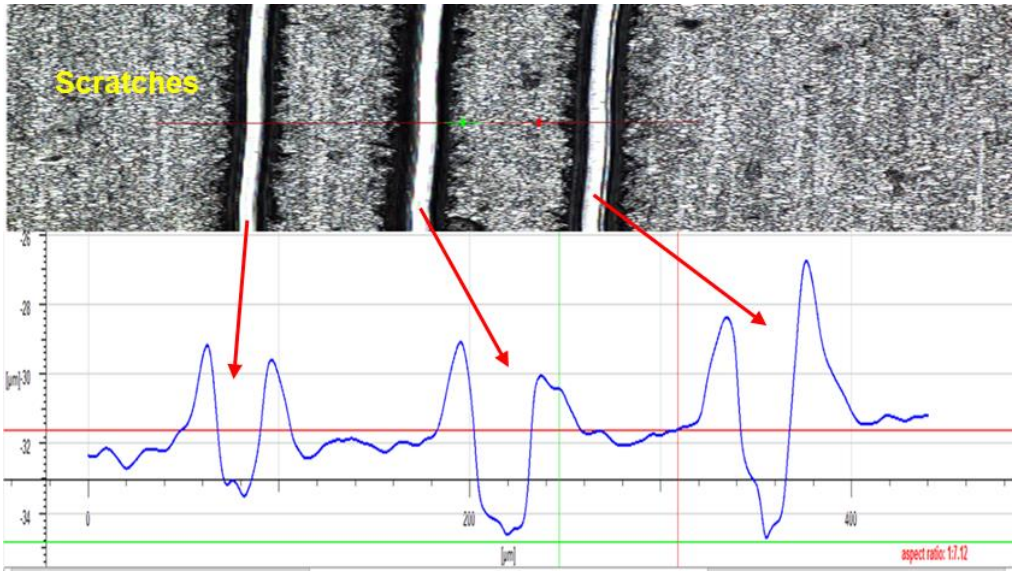
Figure 7.5 Material removal rates produced by conventional abrasive pad (MD 220) and the engineered Population 1 from the load controlled inverted grinding test at 30N

The results of scratch tests in two cutting directions on a Piano 220 abrasive pad and the laser generated Populations 2 and 3, having equivalent planar contact areas at 30N load based on the square frustum abrasive size are shown in Table 7.2.

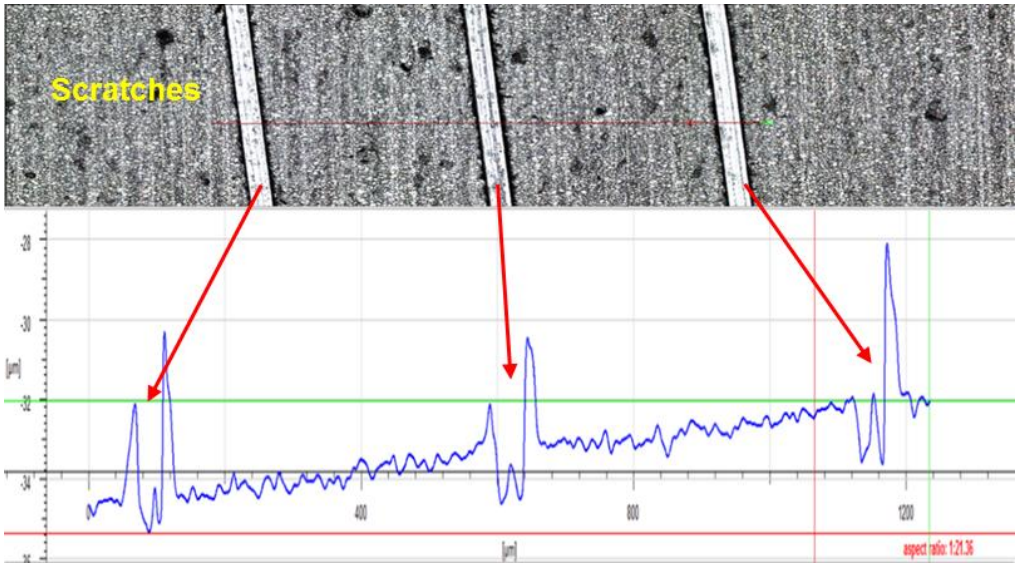
Table 7.2 Specific volume removed of 0.1mm scratch length for conventional abrasive pad (MD 220) and engineered, Population 2 and 3 at 30N load

Pad type	Specific volumes cut at 90^0	Specific volumes cut at 0^0
Population 2	15807 μm^3	5919 μm^3
Population 3	19911 μm^3	8898 μm^3
Piano (Ave. volume cut)	15144 μm^3	

While little change in the specific volume removal was observed between the two cutting directions with the Piano 220 pad (average value given), large differences existed with the specific volume removed by Population 2 engineered abrasives. In the cutting direction 90^o where discrete scratches were produced by each abrasive, Population 2 showed small increase in specific volume removed of 4.4% compared with that for the Piano pad but a reduction of 65.3% in the 0^o cutting direction with the abrasives in overlap. A similar trend existed with Population 3. However, it can be observed in Figure 7.6 and table 7.2, resulting from the dimpled relief with an associated increase in overall cutting depth at 30N load (Population 2: 2.9μm, Population 3: 3.6μm) a significant increase in specific volumetric removal was achieved over Population 2 in both cutting directions (90^o: 26.0%, 0^o: 50.0%). This produced an advantage in specific volume removed of 31.5% over the Piano 220 in the 90^o cutting direction when discrete scratches were produced.



(a)



(b)

Figure 7.6 Scratch profile of a) Population 2 and b) Population 3 at 30N

It has been demonstrated with the scratch tests that for the conventional diamond abrasive pad, only a small percentage of visible abrasives engage with the workpiece. Due to the sparse population of abrasives engaged with the workpiece over the area of the pad (i.e. bond matrix), the occurrence of abrasive overlap is expected to be minimal and therefore material removal rate in the grinding process is not highly sensitive to cutting direction. The material removal is however sensitive to applied

load as the number of abrasives and their depths of engagement vary significantly with load.

By contrast the high population of abrasives engaged with the workpiece in the case of Population 1, even though more cutting edges are engaged, lower material removal rates are produced by the lower contact pressure and resulting lower depths of cut with the workpiece.

The material removal performance of Populations 2 and 3 in the cutting directions 0^o when no abrasive overlap exists, exceeds that for the conventional diamond abrasive bond matrix, when the regular square frustum proves a more effective cutting edge to the irregular edge of the diamond abrasive. These deliberately aligned abrasive arrays however demonstrate the effect of overlap of closely populated abrasives with the large reduction in material removal at 0^o cutting direction.

The scratch tests have also revealed that in the load controlled plane grinding system, that the specific volume of material removed for an abrasive is sensitive to the contact geometry of the abrasive, as demonstrated with Population 3 producing a significant increases specific volume removal over both Population 2 and the conventional diamond / bond matrix.

7.3 Conclusions and remarks

The inverted grinding tests in combination with linear scratch tests have aided the assessment of the material removal performance of both conventional diamond abrasives in a resin bond matrix and of the laser generated geometrically controlled diamond abrasives arrays under load controlled conditions.

The increased understanding of the working population of abrasives in relation to the abrasives visible on the surface of a conventional diamond

bonded system, the effects of abrasive contact area, contact geometry and overlap in the cutting direction provide valuable insights for the design of abrasive surfaces for the enhancement of material removal rates.

It has been shown that laser generated abrasives can provide Significant advantages in material removal, particularly when the abrasive contact geometry is designed to provide clearance in the cutting directions. The modeling of the abrasive cutting trajectories, considering cutting directions and abrasive overlap will allow the full potential of laser generated designed abrasive surfaces to be exploited in future work.

Chapter 8

Strategy of determining design parameters for engineered abrasive pad

In the Chapter 4 to 7, two design parameters (grit geometry and planar contact area) of engineered abrasive pad has been evaluated in relations to their influence on the working performance (e.g. surface roughness, material removal etc.) under the condition of load controlled plane grinding process (planetary movement). This chapter aims at briefly summarizing the approaches and criteria covered in previous chapters to develop a preliminary benchmark procedure of determining design parameters for engineered abrasive pad for future work.

8.1 Determination of grit geometry

Based on the evaluation of different grit geometries in Chapter 4, it revealed that grit geometry is a critical design parameter that has a significant influence on finishing performance. As in theory, the possible defined geometry is infinite, the criterion used to select the geometry is the utilization of cutting edges during planetary movement. Engineered grits with symmetric shapes (e.g. square frustum) was proved to be the better generic design than the asymmetric shapes (e.g. saw tooth). As a result, the procedure to select and optimize the grit geometry in the benchmark methodology is supposed to be evaluating the symmetric grit with different numbers of cutting edges (e.g. circular, square, hexagon) for specific application.

8.2 Determination of planar contact area

As the results shown in Chapter 6 and 7, besides the grit geometry, planar contact area (affect working pressure) is a key design parameter for material removal and reduce the subsurface damage in load controlled plane grinding process. In order to determine the planar contact area for a specific application, the first step is to determine the actual engaging planar contact area of the conventional abrasive pad used for that application, which provides a quantitative guidance on the planar contact area required (same level of working pressure). This is done by a linear scratch test, and the planar contact area is calculated based on the spherical interpolation of grit. After that, the contact area per unit grit can be determined based on the numbers of on the abrasive pad. The further optimization of the planar contact area in the benchmark methodology is supposed to be adjusting the engaging planar contact area derived from conventional abrasive pad.

8.3 Evaluation of the design

Once the grit geometry and planar contact area are determined, the sample pad can be manufactured by laser ablation technique and evaluation through the morphological and topographical analysis described in Chapter 3.

The defined geometry of engineered abrasive grits also allows the geometrical modelling of the workpiece surface texture, the modelling approach developed in Chapter 5 can be used to predict the surface roughness generated by symmetric abrasive grits in parallel to experimental evaluation. Figure 8.1 shows the steps of the preliminary benchmark strategy for design and evaluate engineered abrasive pad.

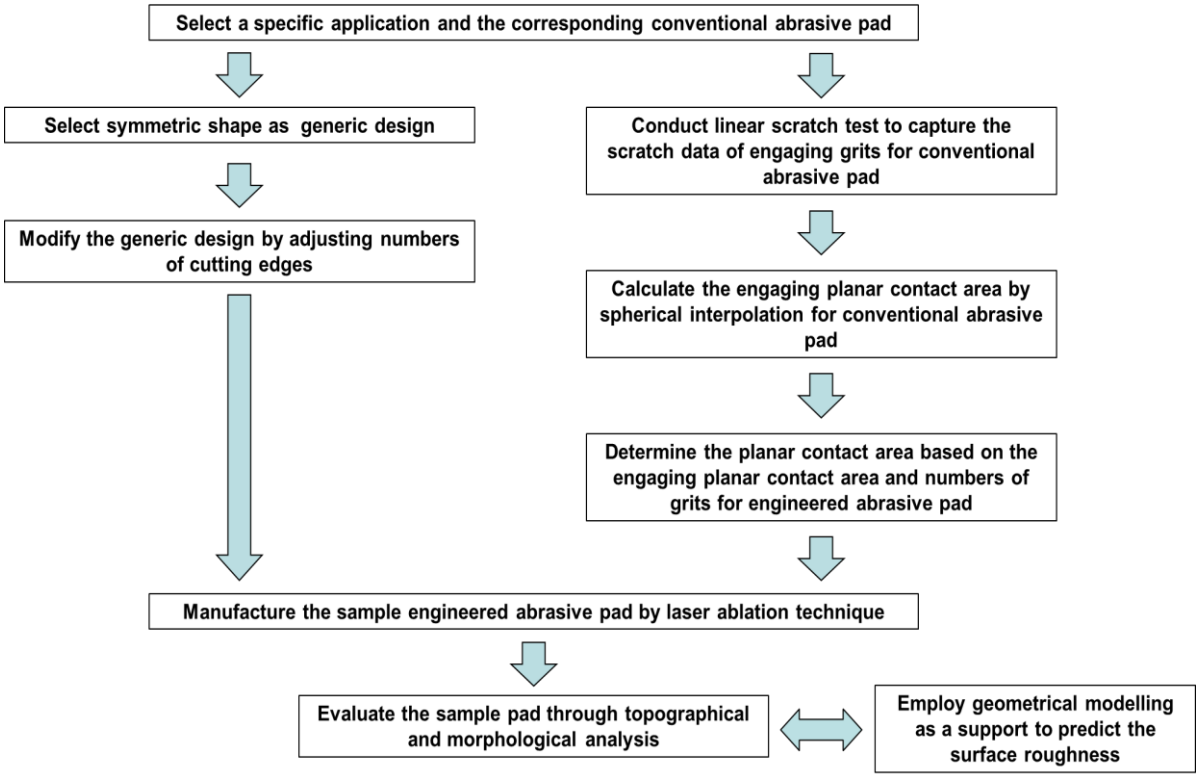


Figure 8.1 Procedures of the preliminary benchmark strategy for design and evaluation of engineered abrasive pad

Chapter 9

Research outcomes and future works

This chapter aims at discussing the overall outcomes of this research and also provide the outlook of future work related to the research findings. In particular, findings on evaluation of laser generated engineered abrasive tool in the application of plane grinding and modelling approach for surface roughness prediction, are summarized.

9.1 Summary of research, findings and conclusions

As the development of modern engineering, more and more industrial applications requires components with high profile accuracy and surface finish. Therefore conventional grinding tool with stochastic features exhibiting less controllable performance is no longer the optimized choice for material removal and finishing. This research work aims at generating laser ablated engineered abrasive pad with controlled features for plane grinding application and develop a geometrical model to simulate the grinding process. The objectives of this research work were presented in chapter 1, while the methodology adopted to conduct all the research work and achieve the objectives were included in chapter 3. The research activities and the corresponding outcomes in relation to the objectives are presented as follows:

i. ***Research activity***: An understanding of influence of grain geometry on the surface topography and material removal rate along with the study of tool wear mechanism and material removal mechanism for both conventional and engineered

abrasive pad (grit size is comparable to conventional pad) was carried out, by generating the feature controlled PLA abrasive pad and tested under an inverted plane grinding setup.

Research outcome: Results in chapter 4 revealed that symmetric engineered abrasive grits (e.g. square frustum) exhibited better finishing performance than that of non-symmetric ones (e.g. saw tooth), indicating symmetric geometries tend to provide effective and uniform cutting orientation more often under the planetary movement machining process (e.g. plane grinding).

Characterization of tool showed that there is no evident sign of wear for engineered abrasive grits, while various wear mechanisms (microfracture, cracking, flattening) wear found for conventional abrasive grits after grinding. In addition, study on the grinding performance revealed that square frustum grits is capable of achieving better surface finish faster, however with a lower material removal rate, than that of conventional grits. The large and flat contact area of engineered abrasive grits resulting in sliding contact which introduce less damage but also remove less material.

ii. ***Research activity:*** A geometrical model was developed to simulate the workpiece surface profile generated by PLA engineered abrasive grits, in order to predict the surface roughness. A validation test was carried out considering the slippage between abrasives and workpiece by inverted grinding test, along with comparison against simulated surface.

Research outcome: The geometrical model has been successfully developed by first deriving the 2D trajectories of grits based on kinematics, and then generating the 3D profile along the trajectories. The slippage was captured experimentally by a

rotary sensor and introduced to the model. A good agreement between simulation and experimental results was observed, the average difference of surface roughness Sa for three measured spots is 13.6%.

iii. ***Research activity:*** A study of influence of planar contact area on the grinding performance was carried out by conducting inverted test on conventional abrasive pad and two engineered abrasive pad with different grit size. Evaluation procedures used in Chapter 4 along with subsurface damage analysis and micro-hardness test were carried out for further study of surface integrity.

Research outcome: Two laser ablated engineered abrasive pad with different grit size (40x40μm and 50x50μm) were generated. The results of inverted test revealed that the progression trend of surface roughness and material removal rate is similar to the results in Chapter 4. However, the design with smaller grit size is superior to the design of larger grit size in terms of surface finish, material removal and less subsurface damage, indicating the influence of planar contact area of grits on the cutting performance. It was found that conventional abrasive pad performed slightly better than engineered abrasive pad in terms of material removal. As the designs of engineered abrasive pad generated are the emulation of conventional abrasive pad in terms of grit number and size, their planar contact area did not take the real planar contact area of engaged grits into consideration. These results led to a new research activity for determination of real planar contact area of conventional abrasive pad, providing an approach to optimize the future design of engineered abrasive tool.

iv. ***Research activity:*** A study on the working population of abrasive in relation to visible abrasives to enable the understanding of influence of planar contact are on material removal is conducted. This objective is achieved by conducting a combination of inverted grinding test and linear scratch test on the conventional abrasive pad and PLA abrasive pad designed to have equivalent real planar contact area as conventional abrasive pad.

Research outcome: Number of visible grits was extracted from SEM imaging and the theoretical planar contact area is calculated based on spherical interpolation of grits. By comparing the theoretical planar contact area with real planar contact area of engaged abrasives captured by linear scratch test, it was found only a very small percentage of grits are engaged with workpiece during grinding operation. The laser generated abrasives based on the real planar contact shows an advantage in material removal, particularly when the abrasive contact geometry is designed to provide clearance in the cutting directions. These results allow the optimization of laser generated abrasives for future work.

9.2 Future work

This research work has presented a novel design of engineered abrasive pad for the application of plane grinding consisting of patterned micro-cutting elements with regular shapes and protrusion heights. A geometrical modelling approach was also presented which can predict the surface roughness of machined workpiece surface generated by

engineered abrasive pad. On the one hand, although the results showed engineered abrasive pad has superior performance against conventional abrasive pad, and study on the planar contact area between abrasives and workpiece provide a method to improve the current design. Some of the design parameters are still not fully investigated to achieve the optimized performance. On the other hand, despite the geometrical model achieved a good agreement with the experimental data, it did not consider the material properties and working conditions (lubricants, vibration etc.) , these parameters can have significant influences on the simulation accuracy which also needs to be introduced in future work. Some of the main possible future work are listed as follows:

1. In chapter 4, the geometry of grits was divided into symmetric and non-symmetric and square frustum and saw tooth grits were selected as representatives for performance comparison. This way of describing the geometry is very general and may not be able to categories engineered grits geometry in some specific cases. Numbers of shape factor can be developed to more accurately describe the regular shaped grits along with a theoretical model to demonstrate their removal characteristics, and then an in-depth study can be done on optimization of grit geometries for different abrasive machining applications.
2. The results in chapter 7 showed laser generated abrasives with equivalent planar contact area to the Piano 220 pad exhibited advantage in material removal. However, due to the limitations on the laser technique employed to manufacture the PLA pad, it is unable to generate very small grit with defined cutting edges, therefore only three aligned grits were produced. Future work can done to explore the manufacturing techniques that is capable of producing grits with defined cutting edges in a smaller scale. Furthermore, how to distribute the equivalent contact area across

the surface to achieve optimized performance has not been studied either. An optimization study could be done by investigating the correlation between planar contact area of individual grit and material removal for future work. Moreover, the linear scratch test can be used to evaluate material removal rate, however, it cannot fully emulate the working condition of plane grinding process. Future work could be done to improve the accuracy of PLA grits with smaller sizes that can distribute all over the surface and still have the equivalent planar contact area as conventional pad. This can lead to a full scale test under inverted test setup.

3. As geometrical model developed in this study did not consider the material properties and working conditions (lubricants, vibration etc.), it suggested the future directions of improvements. For instance, when updating the surface profile along the 2D trajectories, wear modes for different materials can be taken into consideration for adjusting the simulated scratch profile. In addition, the experimentally determined slippage between abrasives and workpiece can be analytically or numerically expressed which reduce the excessive experiments work for specific conditions.

References

1. Grinding wheel developments-principles of modern grinding technology (second edition), CRC Press, 2012.

2. Conventional diamond tool, 2015, https://static1.squarespace.com/static/58b8899e20099e3eada76504/t/5948129f4c8b03f2703c913c/1497895587590/CDT-brochure-FOR+WEB-LoRes.pdf.

3. Transparency market research, Abrasives (Bonded Abrasives, Coated Abrasives, Raw Superabrasives, Steel Abrasives, Loose Abrasive Grains and Others) Market for Machinery, Electrical & Electronic Equipment, Transportation, Metal Fabrication and Other End-user Industries - Global Industry Analysis, Size, Share, Growth, Trends and Forecast, 2013 – 2019, 2014.

4. G.I. Alden, Operation of grinding wheels in machine grinding, Trans. Am. Soc. Mech. Eng, 36 (1914) 451-460.

5. J.J. Guest, Grinding machinery, Edward Arnold, London, 1915.

6. Z. W. Zhong, V. C. Venkatesh, Recent developments in grinding of advanced materials, The International Journal of Advanced Manufacturing Technology, 41 (2009) 468.

7. W.B Rowe, et al., Applications of artificial intelligence in grinding, Ann. Int. Inst. Prod. Eng. Res. Keynote paper, 43(2) (1994) 521-532.

8. W.B Rowe, et al., An open CNC interface for grinding machine, Int. J. Manuf. Sci. Tech. 1, 1 (1999) 17-23.

9. M. Pacella, D. A. Axinte, P. W. Butler-Smith, P. Shipway, M. Daine, C. Wort, An Assessment of the Wear Characteristics of Microcutting Arrays Produced From Polycrystalline Diamond and Cubic Boron Nitride Composites, Journal of Manufacturing Science and Engineering, 138(2) 2015

10. P.W. Butler-Smith, D.A. Axinte, M. Daine, Ordered diamond micro-arrays for ultra-precision grinding – an evaluation in Ti–6Al–4V, Int. J. Mach. Tools Manuf, 51 (1) (2011) 54-66.

11. S.Y. Luo, et al., Grinding characteristics of micro-abrasive pellet tools fabricated by a LIGA-like process, International Journal of Machine Tools and Manufacture, 49(3-4) (2009) 212-219.

12. M. Tsai, S. Chen, Y. Liao, J. Sung, Novel diamond conditioner dressing characteristics of CMP polishing pad, International Journal of Machine Tools and Manufacture 49 (9) (2009)722–729.

13. P.W. Butler-Smith, D.A. Axinte, M. Daine, Preferentially oriented diamond micro-arrays: a laser patterning technique and preliminary evaluation of their cutting forces and wear characteristics, Int. J. Mach. Tools Manuf, 49 (15) (2009) 1175-1184.

14. T.W. Hwang, C.J. Evens, S. Malkin, High speed grinding of silicon nitride with electroplated diamond wheels, part 1: wear and wheel life, ASME Journal of Manufacturing Science and Engineering 122 (February) (2000) 32–41.

15. T.W. Hwang, C.J. Evens, S. Malkin, High speed grinding of silicon nitride with electroplated diamond wheels, part 2: wheel topography and grinding mechanisms, ASME Journal of Manufacturing Science and Engineering 122 (2000) 42–50.

16. X. Chen, W.B. Rowe, Analysis and simulation of the grinding process. Part I: generation of the grinding wheel surface, International Journal of Machine Tools and Manufacture, 36(8) (1996) 871–882.

17. T.A. Nguyen, D.L. Butler, Simulation of precision grinding process, part 1: generation of the grinding wheel surface. International Journal of Machine Tools and Manufacture, 45(11) (2005) 1321–1328.

18. Y. Liu, Y. Gong, R. Bauer, A. Warkentin, Experimental and numerical investigation into workpiece surface topology in point grinding, Proceedings of the Institution of Mechanical Engineers, Part B, Journal of Engineering Manufacture, 0(0) (2012) 1-8.

19. S. Chakrabarti, S. Paul, Numerical modelling of surface topography in superabrasive grinding, International Journal of Advanced Manufacturing Technology, 39 (2008)29–38.

20. A. Darafon, A. Warkentin, R.J. Bauer, 3D metal removal simulation to determine uncut chip thickness, contact length and surface finish in grinding, International Journal of Advanced Manufacturing Technology, 66(9-12) (2013) 1715-1724.

21. P. Jisheng, et al., Abrasive Particles Trajectory Analysis and Simulation of Cluster Magnetorheological Effect Plane Polishing, Physics Procedia, 25 (2012) 176 – 184.

22. Q. Zuqiang, L. Wanjia, L. Weiming, A hydrodynamic and kinematic analysis of chemical–mechanical planarization mechanism in double sided polisher, International Journal of Advanced Manufacturing Technology, 2014; 82-83 (2014) 59–67.

23. Tribology of machining process, second edition, 2013

24. Handbook of Ceramic Grinding and Polishing, Noyes Publications/William Andrew Publishing, Norwich, NY (2000) Chapter 1.

25. R. H. J. Bundy, F. P., Hall, H. T., Strong, H. M. & Wentorf, "Man-made diamonds." Nature, pp. 176, 51–54, 1955.

26. G.V. Raman, The tetrahedral carbon atom and the structure of diamond, Proceedings of the Indian Academy of Sciences - Section A, 46(6) (1957) 391-398.

27. Material science and engineering 8th edition.

28. M.L.Bauccio (Ed.), ASE Engineered Materials Reference Book, 2nd ed., ASM International, Materials Park, Ohio, 1994.

29. J.Singh, Physics of semiconductors and their hetero-structures, McGraw-Hill, New York, 1993.

30. Diamond, Mindat, Retrieved July 7, 2009 <https://www.mindat.org/min-1282.html>.

31. P.W.May, Diamond Thin Films: A 21st Century Materil, Phil. Trans. Royal Society London, A (358) (2000) 473-495.

32. P. John, N. Polwart, C.E. Troupe, J.I.B. Wilson, The oxidation of (100) textured diamond, Diamond and Related Materials, 11 (3–6) (2002) 861-866.

33. G. Davies, T. Evans, Graphitization of Diamond at Zero Pressure and at a High Pressure, Proceedings of the Royal Society A, 328(1574) (1972) 413–427.

34. T. Evans, P.F. James, A Study of the Transformation of Diamond to Graphite, Proceedings of the Royal Society A, 277(1369) (1964) 260–269.

35. T. Evans, Z. Qi, J. Maguire, The stages of nitrogen aggregation in diamond, Journal of Physics C: Solid State Physics, 14(12) (1981) L379.

36. Handbook of carbon graphite diamond and fullerenes, Noyes Publications, 1993.

37. Crystal orientation, 2011, IPCI project, <
http://81.161.252.57/ipci/courses/technology/index_59.htm>

38. S. Ramaseshan, The cleavage properties of diamond, Proceedings of the Indian Academy of Sciences - Section A, (1946) 24-114.

39. J. E. Field, The Properties of Diamond, edited by J. E. Field, Academic Press, London, 1979.

40. T. Smithson, On the nature of the diamond, Philosophical Transactions of the Royal Society of London, 87 (1797) 123–127.

41. J.B. Hannay, On the artificial formation of the diamond, Proc. Royal Society, 30 (1880) 188-189.

42. C.A. Parsons, Experiments on the artificial production of diamond, Proc. Royal Society, 220 (1919) 67-107.

43. C.H.Desch, The Problem of Artificial Production of Diamonds, Nature, 121 (3055) (1928) 799–800.

44. K. Lonsdale, Further Comments on Attempts by H. Moissan, J. B. Hannay and Sir Charles Parsons to Make Diamonds in the Laboratory, Nature, 196 (4850) (1962) 104–106.

45. R. H. J. Bundy, F. P., Hall, H. T., Strong, H. M. & Wentorf, Man-made diamonds, Nature, 176 (1955) 51–54.

46. Synthetic diamond fabrication by HPHT method, 2014, < http://www.substech.com/dokuwiki/doku.php?id=synthetic_diamonds>.

47. Y.A. Sorb, F.P. Bundy, R.C. DeVries, Diamond: High-Pressure Synthesis,

Reference Module in Materials Science and Materials Engineering, 2016.

48. U.F.S. D'Haenens-Johansson, K.S.Moe, P. Johnson, S.Y. Wong, R. Lu, W. Wang, Near-colorless HPHT synthetic diamonds from AOTC Group, G&G, 50(1)(2014) 30–45.

49. U.F.S. D'Haenens-Johansson, A. Katrusha, K.S. Moe, P. Johnson, W. Wang, Large colorless HPHT-grown synthetic gem diamonds from New Diamond Technology, Russia, G&G, 51(3) (2015) 260–279.

50. M.P. Groover, Fundamentals of modern manufacturing, materials, processes, and systems (3rd edition), Prentice Hall Inc, 2007.

51. H. Sumiya, K. Harano, K. Tamasaku, HPHT synthesis and crystalline quality of large high-quality (001) and (111) diamond crystals, Diamond and Related Materials, 58 (2015) 221-225.

52. S. Eaton-Magaña, J.E. Shigley, M.B. Christopher, Observations on HPHT-Grown Synthetic Diamonds: A Review, G&G, 31(3) (2017) 262-284.

53. W. G. Eversole, Synthesis of diamond, U.S. Patent 3030188,1962.

54. J.C. Angus, et al., Growth of Diamond Seed Crystals by Vapor Deposition, J. Appl. Phys, 39 (6) (1968) 2915-2922.

55. B.V. Deryagin, et al., Epitaxial Synthesis of Diamond in the Metastable Region, Rus. Chem. Rev, 39. 39 (9) (1970) 783–788.

56. S. Matsumoto, et al., Vapour deposition of diamond particles from methane, Japanese Journal of Applied Physics, 2 (21) (1982) 183-185.

57. M. Kamo, Y. Sato, S. Matsumoto, N. Setaka, Diamond synthesis from gas-phase in microwave plasma, J. Cryst. Growth, 62 (3) (1983) 642-644.

58. K. Kitahama, K. Hirata, H. Nakamatsu, S. Kawai, N. Fujimori, T. Imai, et al., Synthesis of diamond by laser-induced chemical vapor-deposition, Appl. Phys. Lett., 49 (11) (1986) 634-635.

59. S. Eaton-Magaña, J.E. Shigley, Observations on CVD-Grown Synthetic Diamonds: A Review, G&G, 52(3) (2016) 222-245.

60. D.J. Garrett, et al., Diamond for neural interfacing: A review, Carbon, 102 (2016) 437-454.

61. P. May, CVD diamond – a new technology for the future, Endeavour, 19 (3) (1995) 101-106.

62. CVD Diamond for Electronic Devices and Sensors, Wiley, 2009.

63. J. Gäbler, S. Pleger, Precision and micro CVD diamond-coated grinding tools, 50 (4) (2010) 420-424.

64. H.O. Pierson, CVD in cutting-tool applications, Handbook of Chemical Vapor Depostion (CVD) , 2nd ed., 1999, 452-463.

65. The element six CVD diamond handbook, 2017, < https://www.e6.com/wps/wcm/connect/5cd6a18f-8e5e-488d-87fb-216aff737b14/Element+Six_CVD+Diamond+Handbook_A5_r3_v1.pdf?MOD=AJPERES&CACHEID=5cd6a18f-8e5e-488d-87fb-216aff737b14>.

66. E. Rabinowicz, Friction and Wear of Materials, 2nd ed., John Wiley, New York, 1995.

67. M. M. Kruschov, Principles of abrasive wear, Wear, 28 (1974).

68. D. V. De Pellegrin, A. A. Torrance, Characterisation of abrasive particles and surfaces in grinding, Diamond at Work Conference, Barcelona, 2006.

69. K. H. Zum Gahr, Microstructure and Wear of Materials, Tribology Series 10, Elsevier, Amsterdam, 1987.

70. K. H. Zum Gahr, Wear by hard particles, in New Directions in Tribology, ed. I. M. Hutchings, MEP, 1997.

71. J. M. Challen, P. L. B. Oxley, An explanation of the different regimes of friction and wear using asperity deformation models, Wear 53 (1978) 229–243.

72. K. Hokkirigawa, K. Kato, An experimental and theoretical investigation of ploughing, cutting and wedge formation during abrasive wear, Trib. Int. 21 (1988) 51–57.

73. B.W.E. Anvient, J. Goddard, H. Wilman An experimental study of friction and wear during abrasion of metals, Proceedings of the Royal Society of London Series A (1960) 159-181

74. E. Rabinowicz, A. Mutis, Effect of abrasive particle size on wear, Wear, 8 (1965), 381-390

75. H. Sin, N. Saka, N.P. Suh, Abrasive wear mechanists and the grit size effect, Wear, 55 (1979), 163-190

76. R. Gahlin, S. Jacobson, The particle size effect in abrasion studied by controlled abrasive, Wear, 224 (1999), 118-125

77. I. Sevim, I.B. Eryurek, Effect of abrasive particle size on wear resistance in steels, Materials and Design, 27 (2006) 173-181

78. D.V. De Pellegrin, A.A. Torrance, E. Haran, Wear mechanisms and scale effects in two-body abrasion, Wear, 266 (2009) 13-20

79. J.J. Coronado, A. Sinatora, Effect of abrasive size on wear of metallic materials and its relationship with microchips morphology and wear micromechanisms: Part 1, Wear, 271 (2011) 1794-1803

80. G.Tressia, et al., Effect of abrasive particle size on slurry abrasion resistance of austenitic and martensitic steels, Wear, 376-377 (Part A) (2017) 63-69.

81. T. Sasada, M. Oike, N. Emori, The effect of abrasive grain size on the transition between abrasive and adhesive wear, Wear, 97 (1984) 291-302.

82. A. Misra, I. Finnie, On the size effect in abrasive and erosive wear, Wear, 65 (1981) 359-373

83. J.G. Chacon-Nava, A. Martinez-Villafañe, F. Almeraya-Calderon, J.A. Cabral-Miramontes, M.M. Stack, Some remarks on particle size effects on the abrasion of a range of Fe based alloys, Tribol. Int., 43 (2010) 1307-1317

84. D.V. De Pellegrin, G.W. Stachowiak, Assessing the role of particle shape and scale in abrasion using 'sharpness analysis'. Part I. technique development, Wear, 253 (2002) 1016-1025.

85. D.V. De Pellegrin, N.D. Corbin, G. Baldoni, A.A. Torrance, Diamond

particle shape: its measurement and influence in abrasive wear, Tribol. Int., 42 (2009) 160-168.

86. Y.X. Sun, Y.T. Tsai, K.H. Lin, The influence of sintering parameters on the mechanical properties of vitrified bond diamond tools, Mater. Des., 80 (2015) 89-98.

87. M. Zeren, S. Karagöz, Sintering of polycrystalline diamond cutting tools, Mater. Des., 28 (2007), 1055-1058.

88. G.X. Mei, Q.L. Li, H.H. Su, J.H. Xu, Based on the brazing of abrasive orderly arranged diamond tool the new preparation technology research, Mach. Manuf. Autom., 4 (2012) 10-11.

89. K. Wegener, et al., Recent developments in grinding machines, CIRP Annals, 66 (2) (2017) 779-802.

90. B.Kersschot, On the Dressing Behavior in ELID-Grinding, Procedia CIRP, 6 (2013) 632-637.

91. W. Brian Rowe, et al., Principles of Modern Grinding Technology (Second Edition), William Andrew, 2014.

92. P.W. Butler-Smith, D.A. Axinte, M. Daine, Ordered diamond micro-arrays for ultra-precision grinding—An evaluation in Ti–6Al–4V, International Journal of Machine Tools and Manufacture, 51 (1) (2011) 54-66.

93. S. Malkin, C. Guo, Thermal analysis of grinding, CIRP Ann. Manuf. Technol, 56 (2) (2007) 760-782.

94. J.C. Aurich, B. Linke, M. Hauschild, M. Carrella, B. Kirsch, Sustain. Abras. Process, CIRP Ann. Manuf. Technol, 62 (2) (2013) 653-672.

95. F.W. Pinto, An Experimental and Numerical Approach to Investigate the Machining Performance of Engineered Grinding tools (Ph.D. thesis), ETH Zürich, Zürich, Switzerland (2008).

96. K. Rickens, D. Grimme, O. Riemer, E. Brinksmeier, Engineered diamond wheels for precision ductile grinding, Prod. Eng, 8 (2) (2006) 71-76.

97. G. Burkhard, F. Rehsteiner, B. Schumacher, High efficiency abrasive tool for honing, CIRP Ann. Manuf. Technol, 51 (1) (2002) 271-274.

98. J.C. Aurich, O. Braun, G. Warnecke, L. Cronjäger, Development of a superabrasive grinding wheel with defined grain structure using kinematic simulation, CIRP Ann. Manuf. Technol., 52 (1) (2003) 275-280.

99. J.C. Aurich, P. Herzenstiel, H. Sudermann, T. Magg, High-performance dry grinding using a grinding wheel with a defined grain pattern, CIRP Ann. Manuf. Technol, 57 (1) (2008) 357-362.

100. P. Herzenstiel, J. Aurich, CBN-grinding wheel with a defined grain pattern – extensive numerical and experimental studies, Mach. Sci. Technol, 14 (3) (2010) 301-322.

101. F.W. Pinto, Grain Pattern Evaluation on Engineered Grinding Tools, LAMDAMAP, 2005 (2005) 412-421.

102. F.W. Pinto, G.E. Vargas, K. Wegener, Simulation for optimizing grain pattern on Engineered Grinding Tools, CIRP Annals, 57(1) (2008) 353-356.

103. Y.S. Lv, D.F. Liu, Z.H. Kou, An Investigation on a tin fixed abrasive polishing pad with phyllotactic pattern for polishing wafer, J. China Ordnance, 8 (3) (2012) 174-180.

104. Y.S. Lv, J. Wang, C.Y. Zhao, Y. He, An end-grinding wheel with the phyllotactic pattern of abrasive grain clusters and its milling-grinding experiments, Acta ArmamentarII, 34 (12) (2013) 569-1574.

105. Y.S. Lu, J. Wang, Y.M. Liu, X.L. Xing, Development of a novel polishing pad with a phyllotactic pattern, and experimental studies, J. Electron. Mater, 43 (7) (2014) 2738-2746.

106. H.N. Li, D. Axinte, Textured grinding wheels: A review, International Journal of Machine Tools and Manufacture, 109 (2016) 8-35.

107. C. Heinzel, K. Rickens, Engineered wheels for grinding of optical glass, CIRP Ann. Manuf. Technol, 58 (1) (2009) 315-318.

108. H.P. Yuan, H. Gao, Y.D. Liang, Fabrication of a new-type electroplated wheel with controlled abrasive cluster and its application in dry grinding of CFRP, Int. J. Abras. Technol, 3 (4) (2010) 299-315.

109. Y. Zhou, D. Axinte, P. Butler-Smith, E. Jessen, T. Norbygaard, Effects of novel rotary-abrasive finishing pad textures on the controlled 2-body

abrasive wear of Type 304 stainless steel, Wear, 348–349 (2015) 89-97.

110. P.W. Butler-Smith, D.A. Axinte, M. Daine, Solid diamond micro-grinding tools: from innovative design and fabrication to preliminary performance evaluation in Ti–6Al–4V, Int. J. Mach. Tools Manuf, 59 (0) (2012) 55-64.

111. H. Tönshoff, J. Peters, Modelling and simulation of grinding processes, Ann. CIRP, 41 (1992) 677-688.

112. E. Brinksmeier, J. Aurich, Advances in modelling and simulation of grinding processes, Ann. CIRP, 55 (2) (2006) 667-696.

113. C.L. He, W.J. Zong, Z.M. Cao, T. Sun, Theoretical and empirical coupled modeling on the surface roughness in diamond turning, Mater Desig, 82 (2015) 216-222.

114. R. Hecker, S. Liang, Predictive modeling of surface roughness in grinding, Int. J. Mach. Tools Manuf, 43 (2003) 755-761

115. P. Agarwal S,, P.V. Rao, A probabilistic approach to predict surface roughness in ceramic grinding, Int J Mach Tools Manuf, 45 (2005) 609-616.

116. R.L. Hecker, S.Y. Liang, X.J. Wu, D.G.W. Jing, Grinding force and power modeling based on chip thickness analysis, Int J Adv Manuf Technol, 33 (5–6) (2007), pp. 449-459.

117. P. Stepien, A probabilistic model of the grinding process, Appl Math Modell, 33 (2009), pp. 3863-3884.

118. X. Zhou, F. Xi, Modeling and predicting surface roughness of the grinding process, Int. J. Mach. Tools Manuf., 42 (2002), pp. 969-977.

119. A. Mohamed, R. Bauer, A. Warkentin, Application of shallow circumferential grooved wheels to creep-feed grinding, J. Mater. Process. Technol., 213 (2013), pp. 700-706.

120. Kemet, Polycrystalline Diamond, 2017 < https://www.kemet.co.uk/products/diamond-products/polycrystalline-diamond>

121. L. Bigelow, Diamond Coatings, Journal de Physique IV Colloque, 3

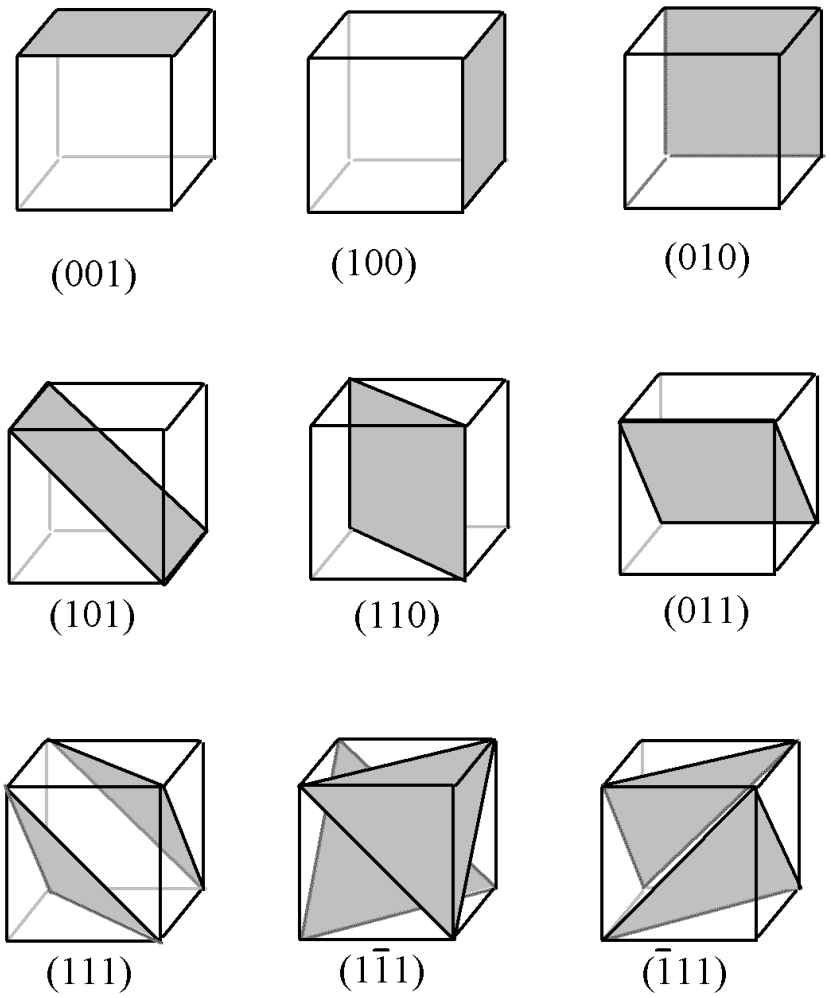
(1993) 897-902.

122. Z.J. Yuan, M. Zhou, S. Dong, Effect of diamond tool sharpness on minimum cutting thickness and cutting surface integrity in ultraprecision machining, Journal of Materials Processing Technology, 62(4) (1996) 327-330.

123. A.L. Carrano, J.B. Taylor, Geometric Modeling of Engineered Abrasive Processes, Journal of Manufacturing Processes, 7(1) (2005) 17-27.

Appendices

Appendix 1 Miler indices



Examples of planes denoted by Miler Indices

(Source: http://www.smartway2study.com/2016/03/salient-features-of-miller-indices-of.html)

Miller indices are derived from a set of three integers that designate crystallographic planes, as determined from reciprocals of fractional axial in

intercepts. Miller Indices are determined as follows:

- A plane of interest is extended to cut the crystal axis system at points which can be denoted as

$$(a_1, b_1, c_1)$$

- Obtain the reciprocals of the axis intercepts. i.e.

$$(1/ a_1, 1/b_1, 1/ c_1)$$

- Multiply or divide by the highest common denominator in the set to obtain the smallest integer numbers.
  - Negative numbers are denoted thus e.g. $-a_1$ as $\overline{a}_1$
  - If the plane is parallel to an axis, the intercept is ∞ and

$$1/\infty=0$$

(Source: https://en.wikipedia.org/wiki/Miller_index)

Appendix 2 FEPA abrasive particle size

This chart is designed to compare millimeters, microns and inches to sieve sizes and match them to corresponding FEPA grit sizes.

Macro grits

Millimeters	Microns*	Inches	FEPA Grit
4.75	4750	0.189	F4
4	4000	0.159	F5
3.35	3350	0.133	F6
2.8	2800	0.111	F7
2.36	2360	0.094	F8
2	2000	0.079	F10
1.7	1700	0.068	F12
1.4	1400	0.056	F14
1.18	1180	0.047	F16
1	1000	0.040	F20
0.85	850	0.034	F22
0.71	710	0.028	F24
0.6	600	0.024	F30
0.5	500	0.020	F36
0.425	425	0.017	F40
0.355	355	0.014	F46
0.3	300	0.012	F54
0.25	250	0.010	F60
0.212	212	0.008	F70
0.18	180	0.007	F80
0.15	150	0.006	F90
0.125	125	0.005	F100
0.106	106	0.004	F120
0.075	75	0.0030	F150
0.063	63	0.0025	F180
0.053	53	0.0021	F220

*Micron size is based upon the 40% min sieve.

Microgrits

Millimeters	Microns*	Inches	FEPA Grit
0.053	53	0.00211	F230
0.0445	44.5	0.00177	F240
0.0365	36.5	0.00145	F280
0.0292	29.2	0.00116	F320
0.0228	22.8	0.00091	F360
0.0173	17.3	0.00069	F400
0.0128	12.8	0.00051	F500
0.0093	9.3	0.00037	F600
0.0065	6.5	0.00026	F800
0.0045	4.5	0.00018	F1000
0.003	3	0.00012	F1200
0.002	2	0.00008	F1500
0.0012	1.2	0.00005	F2000

*Micron size is based upon the 40% min sieve.

Appendix 3 Matlab code for surface profile simulation algorithm

```
function [Z,x1,y1] =
squarefrustum(N,Cx,Cy,Side,w,h,dt,omega1,omega2)

% input datas are
% N: number of mesh points along the side length of mesh
% Cx: x coordinate of sample area on the workpiece disc
% Cy: y coordinate of sample area on the workpiece disc
% side: side length of sample area
% w: half bottom side length of grit
% h: cutting depth of grit
% dt: unit time increasment
% omega 1: angular speed of grinding platern
% omega 2: angular speed of mover plate


x = linspace(Cx-Side/2,Cx+Side/2,N); y = linspace(Cy-
Side/2,Cy+Side/2,N); %create mesh for sample area on workpiece
disc
range = ceil((2*w)/(Side/N));
[x1, y1] = meshgrid(x,y);
Z = zeros(N);


   [xside,yside]=meshgrid(68:1:72,-2:1:2);
   RP=sqrt(xside.*xside+yside.*yside);
   THETA0=atan(xside./yside);
   for n=1:25;
   rp=RP(n);theta0=THETA0(n);

      t = 0; tend =20;

    while t < tend

       [X,Y,theta,alpha] =
toolpath(t,omega1,omega2,rp,theta0);
       if (Cx-Side/2-2*w)<=X && X<=(Cx+Side/2+2*w) && (Cy-
Side/2-2*w)<=Y && Y<=(Cy+Side/2+2*w); % z-map method to update
the surface profile
          pos=(N*[(X-Cx+Side/2) (Y-Cy+Side/2)])/Side;
```

```
            disc2 = max(1,floor(pos(1))-
range):min(N,ceil(pos(1))+range);
            disc1 = max(1,floor(pos(2))-
range):min(N,ceil(pos(2))+range);
            xx=x1(disc1,disc2)-X;
            yy=y1(disc1,disc2)-Y;
            xgrit=xx*cos(theta-alpha)+yy*sin(theta-alpha);
            ygrit=-xx*sin(theta-alpha)+yy*cos(theta-alpha);
            angle = abs(atan(ygrit./xgrit));
            C = Heights(h,w,angle,xgrit,ygrit);
            H=h*(C>0);
            Z(disc1,disc2) = Z(disc1,disc2) -
max(Z(disc1,disc2)+H,0);
            t = t+dt;
            disp(t)
        else
            t=t+dt;
            disp(t)
        end;

      end;

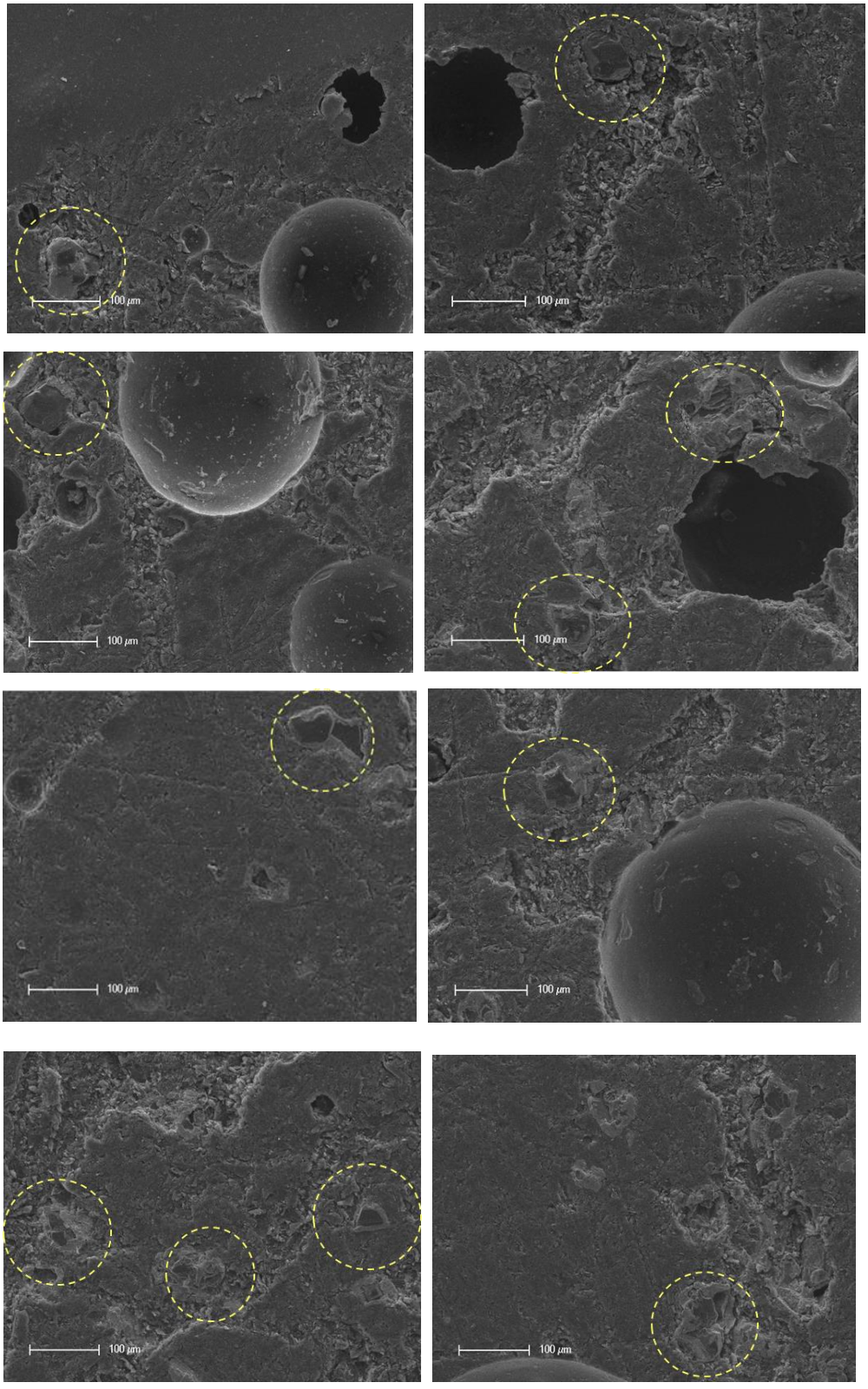
    end;
%mesh(x1,y1,Z)
end

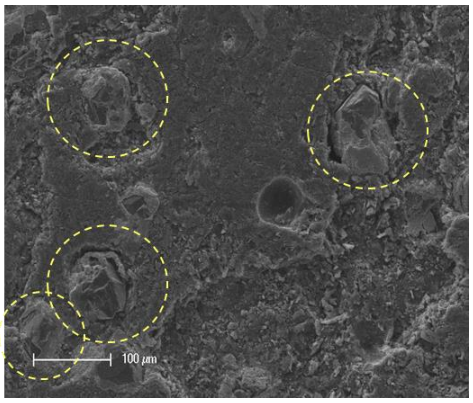
function C = Heights(h,w,angle,xgrit,ygrit) %describe the
protrusion heights for cutting
angle1 = angle.*(angle<=pi/4);
angle2 = angle.*(angle>pi/4);
C1 = max(h*((angle1>0)-abs(xgrit)/w),0);
C2 = max(h*((angle2>0)-abs(ygrit)/w),0);
C = max(C1+C2,0);
end

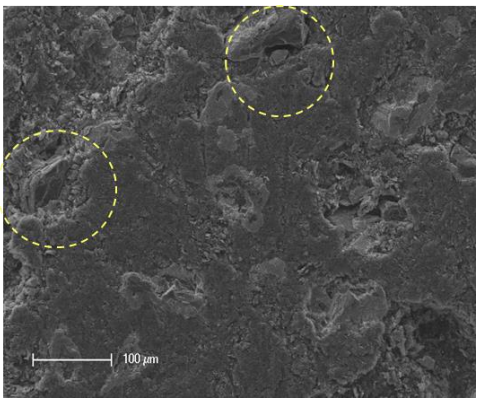
function [X,Y,theta,alpha] =
toolpath(t,omega1,omega2,rp,theta0) % determine the 2D
trajectory of grits
e=50;   % the distance between polishing pad center and disk
center
alpha0=0;
theta=theta0+(omega1*2*pi/60)*t;
alpha=alpha0+(omega2*2*pi/60)*t;
% coordinates of single grit
```

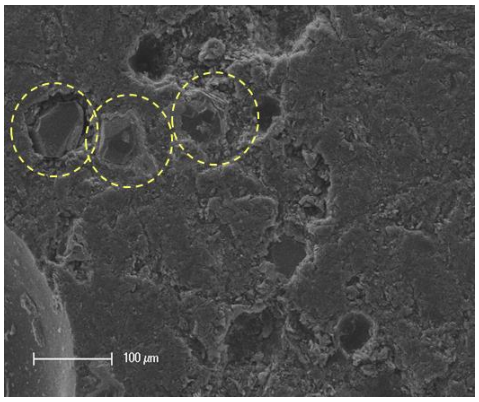
```
%Φ(t) is the experimentally determined slippage between
abrasives and workpiece
X=rp*cos(theta-alpha+Φ(t))-e*cos(alpha);
Y=rp*sin(theta-alpha+Φ(t))+e*sin(alpha);
end
```

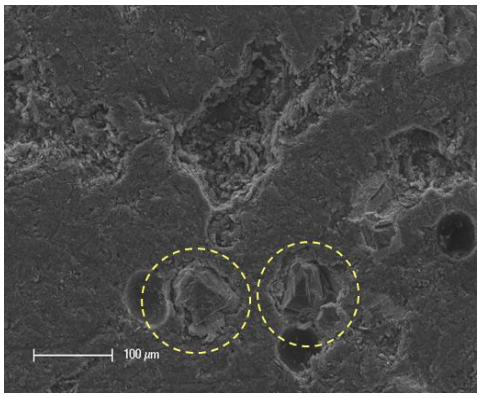
Appendix 4 Visible grits on the Piano 220 pad

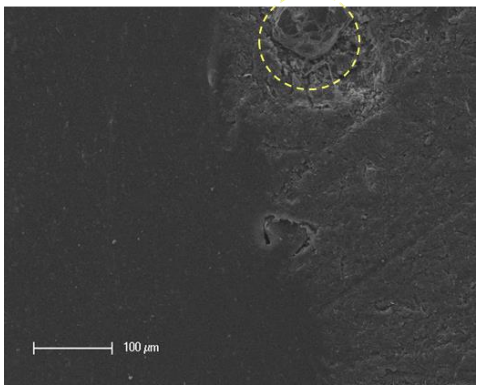


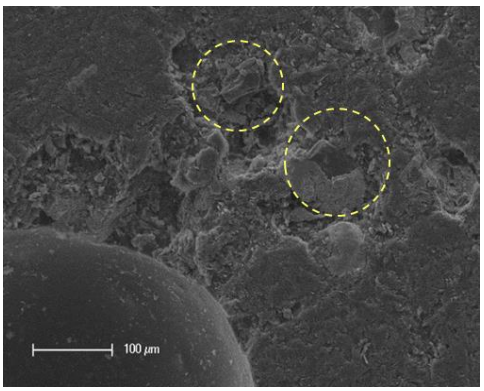

100 µm

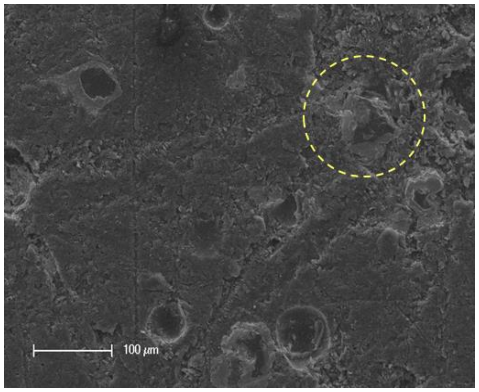

100 µm

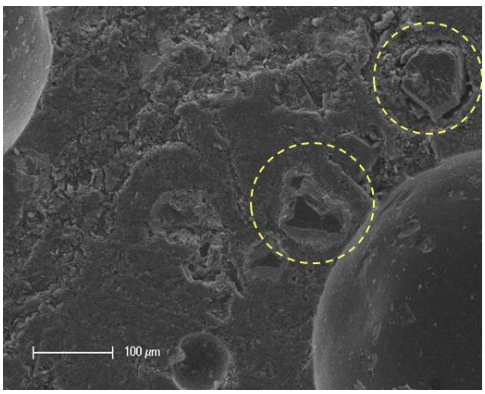

100 µm

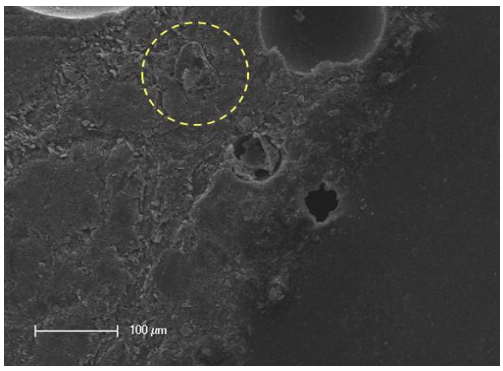

100 µm

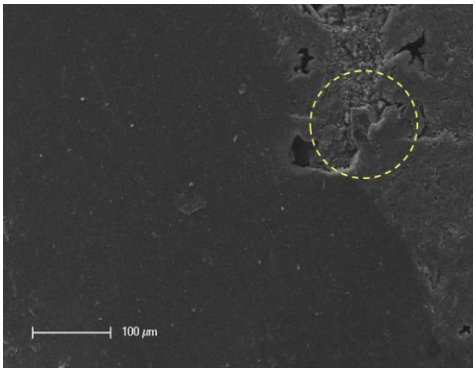

100 µm


100 µm


100 µm


100 µm

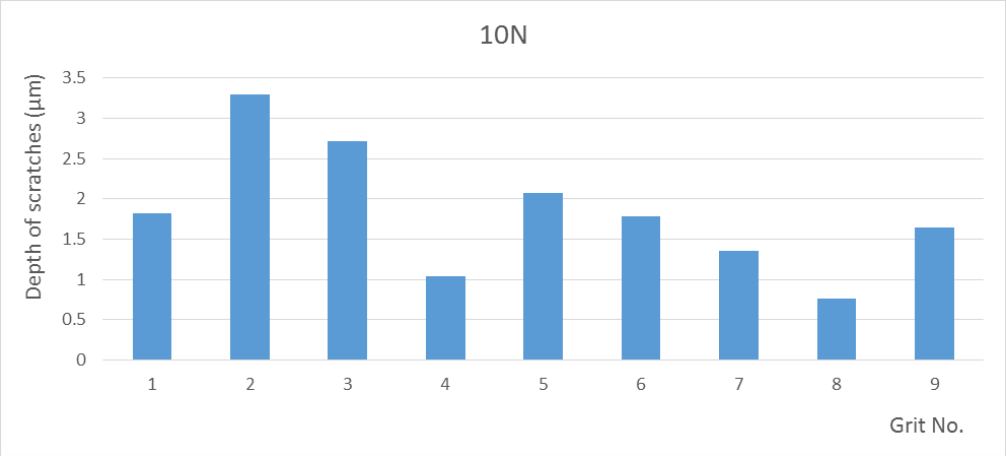

100 µm


100 µm

Appendix 5 Scratch data for Piano 220

Scratch data for 10N trial

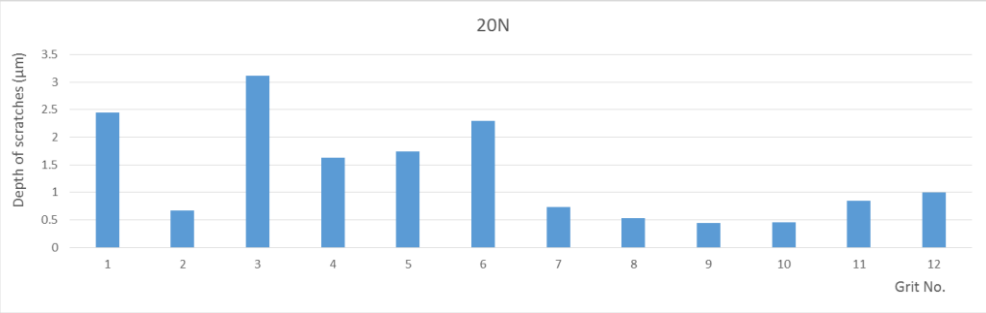
Grit No.	Depth of scratch(μm)	Grit size (diameter of sphere) (μm)	Planar contact area (μm^2)	Total planar contact area (μm^2)
1	1.82	11	95.03	2162.14
2	3.3	16	201.06	
3	2.72	19	283.52	
4	1.04	17	226.97	
5	2.07	19	283.52	
6	1.79	18	254.46	
7	1.36	14	153.93	
8	0.76	26	530.91	
9	1.64	13	132.73	



Scratch data for 20N trial

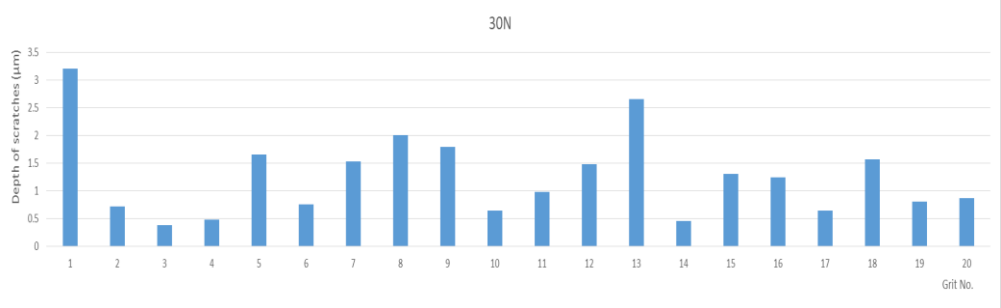
Grit No.	Depth of scratch(μm)	Grit size (diameter of sphere) (μm)	Planar contact area (μm^2)	Total planar contact area (μm^2)
1	2.45	16	201.06	4305.43
2	0.67	18	254.46	
3	3.12	14	153.93	
4	1.63	16	201.06	
5	1.74	18	254.46	
6	2.3	14	153.93	
7	0.73	15	176.71	

8	0.53	20	314.15	
9	0.44	9	63.62	
10	0.46	14	153.93	
11	0.85	18	254.46	
12	1	52	2123.65	



Scratch data for 30N trial

Grit No.	Depth of scratch (µm)	Grit size (diameter of sphere) (µm)	Planar contact area (µm^2)	Total Planar contact area (µm^2)
1	3.21	17	226.97	5532.18
2	0.72	18	254.46	
3	0.39	24	452.38	
4	0.49	10	78.54	
5	1.66	16	201.06	
6	0.76	5	19.63	
7	1.53	17	226.97	
8	2.01	16	201.06	
9	1.8	34	907.89	
10	0.65	14	153.93	
11	0.98	13	132.73	
12	1.48	18	254.46	
13	2.66	17	226.97	
14	0.46	13	132.73	
15	1.31	16	201.06	
16	1.25	9	63.62	
17	0.65	17	226.97	
18	1.57	16	201.06	
19	0.81	40	1256.6	
20	0.87	12	113.09	


30N
Depth of scratches (µm)
3.5
3
2.5
2
1.5
1
0.5
0
1
2
3
4
5
6
7
8
9
10
11
12
13
14
15
16
17
18
19
20
Grit No.